Analysis of Shock Dynamics in Core-Collapse Supernovae

February 2015

Kazuya TAKAHASHI

Analysis of Shock Dynamics in Core-Collapse Supernovae

February 2015

Waseda University
Graduate School of Advanced Science and Engineering
Department of Pure and Applied Physics, Research on Theoretical Astrophysics

Kazuya TAKAHASHI

Abstract

Massive stars whose masses are about ten times larger than the sun are thought to explode and blow up the entire gases at the end of their lives. The explosion is called core-collapse supernova (CCSN) and it is one of the most energetic phenomena in the universe. The CCSNe are associated with the history of the universe in terms of the chemical evolution and the origin of the lives since the heavy elements that were produced in the star are spread out by the explosion. Furthermore, they emit neutrinos and gravitational waves as well as the electromagnetic waves, which give the information on the micro physics under the nuclear density. The next-generation detectors such as Hyper-Kamiokande and KAGRA hence aim at the CCSNe as one of the main targets. For such reasons, to understand the explosion mechanism of CCSNe is one of the significant challenges of modern physics.

In this thesis, we treated the shock dynamics in CCSNe, which is one of the central issues of the fields of supernovae. We focused on the non-spherical structures of core-collapse progenitors, which have been reported by a series of paper by Arnett, and the effects on the shock dynamics at first. We performed a linear analysis and found that the seed perturbations that arise in the outer layer of a progenitor grow sufficiently during they fall onto the stagnant shock surface in CCSNe. Then we also performed another linear analysis, in which we studied the effects of such amplified perturbations on the so-called standing accretion shock instability (SASI). The results are, however, that the fluctuated upstream flows may not affect the unstable modes of SASI although we seem to need further investigations in order to make a robust conclusion.

As the next topic, we treated the shock waves in magnetohydrodynamics (MHD). Since the magnetic field play a central role in some explosion mechanisms, it is also one of the important ingredients in CCSNe. There is, however, an unresolved issue in the theory of MHD, which is related to the physical relevance of the so-called intermediate shocks. We address the problem by studying the solutions of the MHD Riemann problem, which is one of the initial value problems of hyperbolic systems. We developed a new MHD Riemann solver that handles all types of in-

termediate shocks and other non-regular waves in order to investigate the solution space. Applying the code to one of the most famous MHD Riemann problems and its neighborhood, we obtained uncountably many solutions that include intermediate shocks. This result cast a new question on the physical relevance of the intermediate shocks

Contents

Chapter 1

Introduction

1.1 Brief review of core-collapse supernovae

Looking up at the sky, we see thousands of stars and those who were fascinated might have imagined some stories in old times. The mysteries of the celestial objects are day by day solved with the inventions and improvements of observational instrument the theory of physics. Such advances elucidated the wider and deeper landscapes of the universe as well as the new puzzles, which are associated with not only visible objects but also the invisible or transient phenomena such as black holes, gamma-ray bursts, and gravitational waves that will be detected by future experiments.

Supernovae (SNe) are one of the most energetic transients, which are thought to be related with the explosive deaths of massive stars. Due to the extreme brightness, which is comparable to that of a galaxy, some Galactic SNe were observed even with naked eyes and they were written as a 'new star' in historical records (Green & Stephenson, 2003), which include the faithful and well-recorded SNe: SN 1006, SN 1054 (whose remnant is known as the Crab Nebula), SN 1181, SN 1572 (also known as Tycho's SN) and SN 1604 (Kepler's SN). Since SN 1604 is the last SN that was observed in our galaxy, they were not distinguished from normal novae, which are known to be a giant eruption on the surface of a white dwarf, until they were observed in other galaxies and their larger absolute magnitudes were measured in 1920s (see Lyne & Graham-Smith, 2006; Duerbeck, 2008).

Spectroscopically SNe were divided into two groups, Type I and Type II, after the discovery of a SN in NGC 4725 that represented emission lines in the region of Hα and was deficient in other absorption and emission lines (Minkowski, 1940, 1941). Nowadays, the former type is further divided to Type Ia and Type Ib/c. Type Ia SNe are different from the others in terms of the strong absorption lines of

Si II (Filippenko, 1997) and is thought to be the thermonuclear runaway explosion of a white dwarf (Howell, 2011), which synthesizes lots of nickels, whose radio active decay is the main energy source of the optical light.

On the other hand, the other supernovae are thought to be related to the collapse of the massive stars, whose masses are larger than about 10 $M_{\odot}$, and called core-collapse supernovae (CCSNe).In the widely accepted scenario, the explosion is triggered by the collapse of the central iron core, which is the final product of nuclear burnings. As the core collapses, the central density grows and neutrons are produced via inverse beta decays. The so-called proto-neutron star is formed once the nuclear density is reached, which endures the collapse by the degenerate pressure of neutrons. The infalling matter hits the surface and recoils, which produce a shock wave that proceeds outward. It is known, however, that the shock wave stagnates in the iron core due to the large mass accretion rate and loss of energy via photodissociations of nuclei. In fact, searching the way to revive the stagnant shock wave has been the central issue in the field of CCSN mechanisms (Janka, 2012; Kotake et al., 2012). One of the milestones for a feasible and detailed mechanism of CCSNe was placed by Colgate & White (1966), who introduced the idea of the so-called neutrino heating mechanism. In the scenario, neutrinos that defuse out of a proto-neutron star deposit the energies with the fluid below the shock wave, which revives the stagnant shock wave and the shock proceeds outward (Bethe & Wilson, 1985). This neutrino-heating mechanism has been one of the most hopeful mechanisms as well as other scenarios such as the acoustic mechanism (Burrows et al., 2006, 2007) and magneto-driven supernovae (e.g. Kotake et al., 2004; Sawai et al., 2005; Sawai & Yamada, 2014).

It has been commonly accepted that the standing shock wave does not revive in spherically symmetric simulations if detailed physics are properly considered (e.g. Rampp & Janka, 2000; Liebendörfer et al., 2005; Suwa et al., 2014). The reason of the failure is that the neutrino heating becomes insufficient since the fluid particles fall rapidly and pass through the gain region, where the fluid particles receive the energy from neutrinos, in a short time due to the spherically symmetric accretion flow. On the other hand, in higher dimensional flows, matters can stay in the gain region longer in principle. In fact, fluid instabilities such as convections produce complex flow patterns, which prolong the dwelling time.

Standing accretion shock instability (SASI) is one of such fluid instabilities that enhance the efficiency of the neutrino heating. This instability is also thought to be a key to revive the stagnant shock wave as well as neutrino-driven convections. We focus the SASI activity in CCSNe and give a brief review in the next section.

1.2 Standing accretion shock instability

1.2.1 basic properties

As stated above, the mechanism of CCSNe has been a long-standing problem despite intensive efforts. One of the central issues is how a shock wave proceeds outward and breaks out of an iron core. The shock wave that originates from core bounce does not go through the core directly but stagnates due to heavy accretion and loss of energy via photodissociations of nuclei. Among proposed mechanisms, neutrino heating is commonly thought to be the most promising one, in which neutrinos that diffuse out of a proto-neutron star deposit energy to matter and lead to a revival of the standing shock and, as a result, to an explosion.

In this scenario, a multi-dimensional fluid instability that is called SASI may play an important role to enhance the neutrino heating and contribute to shock revival. This is because the standing shock gets deformed rapidly due to the instability and makes complex flows below the shock, which detain the fluid in a gain region longer, even if the standing shock is initially spherically symmetric. A remarkable character of SASI is that the large scale modes dominate both in linear and non-linear regimes, which correspond to $l = 1, 2$ modes in term of the index of the usual spherical harmonics, $Y_{lm}(\theta, \phi)$. In addition to this sloshing motions, the non-axisymmetric spiral motions, where low m is dominant, can develops in three-dimensional simulations. Such dynamical motions of a shock wave that are induced by SASI have been widely observed in multi-dimensional numerical simulations of various progenitors, where detailed physics is taken into account (Abdikamarov et al., 2014; Bruenn et al., 2013; Couch & O'Connor, 2014; Hanke et al., 2013; Iwakami et al., 2008, 2009, 2014a,b; Nakamura et al., 2014; Suwa et al., 2010; Takiwaki et al., 2012, 2014).

From the observational point of view, the existence of SASI may be indirectly inferred. The proper motions of pulsars, some of which are known to have large velocities, may be a consequence of the recoil in an asymmetric explosion that follows SASI (Burrows & Hayes, 1995; Nordhaus et al., 2012; Wongwathanarat et al., 2010, 2013). The rotation of neutron stars may be induced by spiral flows in SASI and redistribution of the angular momentum. Rantsiou et al. (2011); Guilet & Fernández (2014) concluded that the spiral modes of SASI can produce the observed spin periods even for non-rotating progenitors (but see also Wongwathanarat et al., 2010, 2013). Furthermore SASI activity in CCSNe is expected to be observed as an imprint in gravitational wave signals, which gives more direct evidence of the instability (Murphy et al., 2009; Kotake et al., 2009, 2011; Müller et al., 2012, 2013; Kuroda et al., 2014).

The driving force of SASI is thought to be the cyclic productions of waves, which propagate inward and outward, in the shocked region. Suppose that a small fluctuation arises behind the shock surface. It will travel inward and produce an acoustic wave that propagates outward when it reaches the region where the background flow changes sharply (e.g., the region near the proto-neutron star surface). The outgoing acoustic wave will reach the shock and strike the surface, which makes new waves that propagate inward. If the amplitudes of waves grow as the procedure is repeated, this coupling cycle of the ingoing and outgoing waves makes the standing shock unstable (Guilet & Foglizzo, 2012). There are, however, two different versions in this basic idea. The difference is that the ingoing wave that produces the outgoing acoustic wave is a vorticity wave or an acoustic wave; The former cycle is called the advective-acoustic cycle and the other is referred to as the purely-acoustic cycle. Both of the cycles can cause an instability in principle and hence it is the matter of their efficiencies. The difference of the mechanism results in a different time evolution of the shock surface such as oscillatory frequency and growth rate. Previous linear analyses support the advective-acoustic cycle since the eigen frequencies match the crossing timescale of advections and acoustic waves between the shock radius and proto-neutron star surface (Yamasaki & Yamada, 2007; Foglizzo et al., 2007; Yamasaki & Foglizzo, 2008; Foglizzo, 2009; Sato et al., 2009; Guilet & Foglizzo, 2010, 2012). Some numerical simulations also confirmed the dominant role of the advective-acoustic cycle (Ohnishi et al., 2006; Scheck et al., 2008; Müller et al., 2012; Takiwaki et al., 2012). On the other hand, however, some author reported that the purely-acoustic cycle is responsible for the instability (Blondin & Mezzacappa, 2006; Blondin & Shaw, 2007). Hence, it is not completely understood which mechanism is really essential for SASI.

As seen from the driving mechanisms, SASI is known to be essentially different from the convective instability. In fact, SASI occurs even in isentropic flows, where there is no negative entropy gradient (Blondin et al., 2003). It is difficult, however, to distinguish them in realistic simulations and which instability is important in CCSNe is still controversial (see Iwakami et al., 2014a,b, and references).

It is worth noting that SASI itself is found not only in CCSNe but also in other phenomena: e.g. in a disk around a black hole (Nagakura & Yamada, 2008, 2009) and in a shallow water experiment (Foglizzo et al., 2012). It is also noted that the relation between SASI and the g-mode instability of a proto-neutron star has been discussed, which may help the explosions by the acoustic mechanism (Burrows et al., 2006, 2007), although a linear analysis by Yoshida et al. (2007) and other numerical simulations did not find such evidence (e.g. Marek & Janka, 2009).

1.2.2 a new question on SASI

As discussed in the previous section, SASI is an important key to the explosion mechanism and observable properties as well. Hence, the analytical studies have been performed to investigate nature of SASI (Yamasaki & Yamada, 2005, 2006, 2007; Foglizzo et al., 2007; Yamasaki & Foglizzo, 2008; Foglizzo, 2009; Sato et al., 2009; Guilet & Foglizzo, 2010, 2012). They assumed, however, that the matter flow outside the shock is steady and spherical.

This assumption may not be justified as pointed out by Bazan & Arnett (1998); Asida & Arnett (2000); Meakin & Arnett (2006, 2007); Arnett & Meakin (2011); Chatzopoulos et al. (2014). They numerically investigated nuclear burnings in outer layers (Si, O, C, and Ne shells) in the pre-collapse stage and found that the structures of progenitors are substantially deviated from spherical symmetry due to violent convections. Couch & Ott (2013) reported recently that such non-spherical fluctuations in the progenitor may yield successful explosions even when no explosion obtains without the fluctuations. Furthermore, Müller & Janka (2014) systematically investigated the effect of such non-spherical perturbations by artificially adding various perturbations in outer layers. They reported that the large scale ($l = 1, 2$) perturbations are effective in shock revival.

This non-spherically symmetric nature of the progenitors and its effect on SASI are the first topic of this thesis. We postpone the details of our scope, however, to Sec. 1.4.

1.3 Magnetohydrodynamics

1.3.1 magnetohydrodynamics in CCSNe

The magnetic field is also one of the main topics that are related to CCSNe. There are many observational evidences that neutron stars have a strong magnetic field, which is about $10^{12} - 10^{13}$ G (e.g. Lorimer, 2009). Furthermore, there are also some observations that indicate the existences of so-called magnetars, which have stronger magnetic fields that are estimated as $\sim 10^{14}$ or even $\sim 10^{15}$ G (Hurley, 2009).

These objects are thought to be a remnant of CCSNe and the way to produce such a strong field has been discussed by many authors (Sawai et al., 2013). In addition, there are some mechanisms in which magnetic fields pla (see e.g. Kotake et al., 2004; Sawai et al., 2005; Sawai & Yamada, 2014, and references).

The magnetic field should be also related to SASI since the number of modes increase due to the magnetic field, which affect the mechanism of cycle (Guilet &

Foglizzo, 2010). Moreover, Endeve et al. (2010, 2012) pointed out that SASI strengthens the magnetic field and hence contributes to the magnetization of a neutron star.

From the above results, the magnetohydrodynamics (MHD) can be essential in CCSNe. There remains, however, an unresolved issue in MHD theory indeed. It is the problem of the physical relevance of a class of MHD shock waves, which are so-called intermediate shocks. We review the issue in the following section.

1.3.2 an unresolved issue of MHD Riemann problems

The Riemann problem for a system of 1st-order, hyperbolic partial differential equations is an initial value problem, in which two distinct constant states are separated by a discontinuity initially. By hyperbolic we mean that all eigenvalues of the Jacobian matrix that characterizes small perturbations are real. It is well known that the Riemann problem in ideal MHD has in general non-unique solutions for a given initial condition even if one discards manifestly unphysical ones such as those including rarefaction shock waves, in which entropy is decreased. This is in sharp contrast to the hydrodynamical counterparts and is due to the facts that the system of equations that describes ideal MHD is not strictly hyperbolic, i.e., some of the eigenvalues of the Jacobian matrix are coincident with each other, and that the characteristic fields are neither linear nor genuinely non-linear (see § 4.2 and e.g. Lax, 1957; Jeffrey & Taniuti, 1964; Polovin & Demutskii, 1990). In fact, the MHD Riemann problem has a far greater variety of solutions including so-called intermediate shock waves. Although these intermediate shocks are deemed to be unphysical in some text books, some interplanetary experiments have reported the detections of intermediate shocks (Chao, 1995; Feng & Wang, 2008; Feng et al., 2009) and they are actually realized in almost all numerical solutions. Their reality is hence still an issue of controversy as will be described below more in detail.

Solutions of the Riemann problem consist of discontinuities and centered self-similar simple waves in general (see § 4.2 for more details). Various shock waves appearing in the solutions of Riemann problem are usually characterized by the flow speeds upstream and downstream in the shock-rest frame: in ideal MHD, for example, the fast shock has a flow velocity that exceeds the fast-wave velocity (termed super-fast hereafter) upstream whereas the downstream flow velocity is sub-fast, i.e. lower than the fast-wave velocity, but super-Alfvénic, i.e., higher than the Alfvén-wave velocity (see § 4.3 for the definitions of these wave velocities); assigning the numbers 1, 2, 3 and 4 to the super-fast, sub-fast and super-Alfvénic, sub-Alfvénic and super-slow, and sub-slow states respectively, we designate the fast shock as $1 \to 2$ shock; other shocks are referred to just in the same way.

The intermediate shock waves in ideal MHD have coplanar configurations, i.e. the upstream transverse magnetic field is anti-parallel to the downstream one and they are characterized by the flow velocities that are super-Alfvénic upstream and sub-Alfvénic downstream. They are normally assigned to one of the following four types: $1 \to 3$, $1 \to 4$, $2 \to 3$ or $2 \to 4$ shock. There are some boundary types as well: for example, the $2 \to 3, 4$ shock is a boundary type that has a downstream flow speed that is equal to the slow speed as indicated by its name. As mentioned above, these intermediate shock waves are considered to be unphysical in some textbooks (see e.g. Lax, 1957; Jeffrey & Taniuti, 1964; Polovin & Demutskii, 1990) because they do not satisfy the so-called evolutionary conditions, which require the existence of perturbed states of the same type; for ordinary shock waves (such as the fast shock in ideal MHD), one of the characteristics runs into the discontinuity from both sides; this is not the case for some of the intermediate shocks; for instance, the $1 \to 3$ intermediate shock is a shock wave whose flow speeds in the shock-rest frame are super-fast upstream and sub-Alfvénic and super-slow downstream; hence the fast and Alfvén characteristics go into the shock both upstream and downstream; in the case of the $2 \to 3$ shock, only the Alfvén characteristic converges to the shock wave; however, another evolutionary condition on the linear independence of eigenfunctions is violated and it is classified as unphysical shock.

In spite of the evolutionary conditions, the intermediate shocks are commonly observed as a stable constituent wave in numerical solutions of the MHD Riemann problems (Wu, 1987; Brio & Wu, 1988; Wu, 1988b,a, 1990; Wu & Kennel, 1992). One of the best known cases is the one discussed by Brio & Wu (1988), in which the numerical solution contains a so-called compound wave that consists of a $2 \to 3, 4$ shock followed by a slow rarefaction wave. Wu (1987) also showed numerically that the $2 \to 4$ shock-like structure could be obtained by steepening of a continuous wave, an indication that the resultant structure is physical. In addition he demonstrated that a perturbed states obtained for a slightly different initial condition retains a similar structure. Moreover, Wu (1988b) computed interactions between the $2 \to 4$ shock-like structure and an Alfvén wave and found that the structure remains for a while before it breaks to other waves. These results indicate that the intermediate shock is stable to the perturbation in a sense. Wu (1988b) found that the shock-like structures observed in the computations with perturbations are time-dependent and do not satisfy the Rankine-Hugoniot condition in fact. He claimed that these new types of shocks are the neighboring states for the intermediate shocks. In yet another simulation Wu (1988a) showed that rotational discontinuities, which are not intermediate, break into some other waves that include an intermediate shock. This is a suggestion that it is not intermediate shocks but particular types of evolutionary

discontinuities that are unstable and unphysical. On the other hand, Wu (1990) studied the structures inside shock waves by introducing dissipations and found that they are not uniquely determined by the asymptotic states and there remain extra degrees of freedom. He concluded that the stability of the intermediate shocks to the interactions with Alfvén waves is originated from these degrees of freedom. Incidentally, it was also demonstrated that all types of intermediate shocks can be produced by steepening processes in dissipative MHD.

Completely opposite and equally convincing arguments were made by Falle & Komissarov (1997, 2001). They pointed out that if perfect planarity or coplanarity is imposed initially, the solution retains the symmetry and magnetic fields cannot rotate in the evolutions; then the problem is equivalent to solving the reduced system of MHD equations, in which it is assumed that magnetic fields are confined in a plane and, as a consequence, the Alfvén waves do not exist; this changes the number of characteristics of the system and modifies the evolutionary conditions; in fact, the 180°-rotational discontinuity becomes non-evolutionary whereas $1 \rightarrow 3$ and $2 \rightarrow 4$ shocks become evolutionary for this reduced system. They also demonstrated numerically that the intermediate shock does not emerge if coplanarity of the solution is broken by inserting a thin layer within which the magnetic field rotates continuously. Barmin et al. (1996), on the other hand, found numerically that the compound wave breaks into a rotational discontinuity and a slow shock if the exact coplanarity is perturbed. Although Falle & Komissarov (2001) agreed with Wu (1990) that the temporary survival of $1 \rightarrow 3$, $2 \rightarrow 4$ and $1 \rightarrow 4$ shocks in their interactions with Alfvén waves is due to the non-unique shock structures, it was claimed that they should be regarded as transients.

We also note that the evolutionary conditions themselves have been reconsidered in the mean time (Hada, 1994; Markovskii, 1998; Inoue & Inutsuka, 2007). These authors took dissipations into account, considering that the waves that emerge in dissipative MHD should be physical. With dissiptations shocks are no longer discontinuities and the analysis is facilitated. They found new modes that do not exist in ideal MHD and argued that on account of these modes the intermediate shocks are indeed evolutionary.

As a result, the existence of intermediate shocks is still controversial. To address this issue, we developed a new MHD Riemann solver that can handle the intermediate shocks as mentioned briefly in the next section and Chap 4 in detail. We note here that previous works that are strongly related to our study are separately reviewed in Chap. 4.

1.4 Main topics in the thesis

Considering the above background, this thesis focuss on the following two topics. The first one is the analysis of SASI in CCSNe with non-spherical stellar structures. This topic was studied with the two succeeding linear analyses as described in detail in the following chapters. First, we investigated the evolution of linear perturbations that are given in the supersonic accretion flows in order to know how the fluctuations due to the dynamic convections in Si/O shells are amplified during the infall onto the standing shock. Second, we analyzed the SASI activities that are exposed to such fluctuated non-spherical flows. Both of them are performed with the use of Laplace transform, which is suitable for our analysis.

Our studies are based on the linear analysis although the SASI may grow even into a non-linear phase in reality as seen in numerical simulations. We emphasize, however, that our analyses are the first challenge to understand the SASI with more realistic progenitors that have non-spherical structures. We also note that such analyses are necessary to understand the linear growth phase of the SASI in numerical simulations, which will eventually take into account the non-spherical upstream flows.

Another is a fundamental problem that is related to the theory of MHD: the non-uniqueness of the solutions of MHD Riemann problem and their stabilities. We think that the detailed study of particular solutions of the MHD Riemann problem together with their neighboring ones are also helpful to get some more insights into the reality of intermediate shocks. For this purpose, we coded a program to find all the solutions for arbitrary initial conditions. We have extended the algorithm proposed by Torrilhon (2002, 2003b) so that we could handle all combinations of constituent waves, including all types of intermediate shocks as well as the regular waves. Since the parameter space of the MHD Riemann problem is vast (15 dimensions indeed) and exploring the entire space is almost impossible, we need to pay attention to those initial conditions and their neighborhoods, which appear of particular interest to us. In this thesis we mainly investigated the initial condition that was first picked up by Brio & Wu (1988), which is the most famous MHD Riemann problem and includes a compound wave in one of the solutions as mentioned earlier.

The second topic may seem to have nothing to do with the mechanisms of CCSNe. To solve the above problem is, however, necessary to take a step to understand the magnetic phenomena because it is directly related to the physics of MHD and it is also a basis of MHD numerical simulations. Hence, the topic is associated not only with the physics of SNe but also with all the phenomena in magnetic fields.

Both of these themes give some important basics to analyze the shock dynamics in CCSNe, which will continue to be studied by super-computer simulations in the

future. Hence, we believe that these studies will make much contribution to the elucidation of the mechanism of CCSNe, which is one of the main problems of the modern physics.

This thesis is organized as follows. We devote pages to analyses of SASI at first. In the next chapter, we discuss the analysis of the perturbation growths in supersonic accretion flows in front of a stagnant shock wave. Then the linear analysis of SASI under non-spherical flows is presented in Chap. 3. The latter part of the thesis is mainly devoted to the second topic, which discusses the solutions of MHD Riemann problems in Chap 4. Finally we give a summary of the conclusions in Chap. 5. We also note that some additional information is given as appendices in the last few pages.

Chapter 2

Analysis of the Non-spherical Supersonic Flows

2.1 Introduction

In this section, we analyze the evolution of the perturbations during infall onto the stagnant shock wave, whose seed is the dynamically convective flows in outer la
of a progenitor of CCSNe, as mentioned in the previous chapter.

Instead of conducting multi-dimensional simulations, we investigate the growth
-spherical perturbations in accretion flows onto the standing shock wave, based on linear analysis. In contrast to previous studies (Kovalenko & Eremin, 1998; Lai & Goldreich, 2000, hereafter LG00), we do not treat the asymptotic behavior ($r \to 0$) but deal with the growth of perturbations as an initial and boundary value problem with a use of Laplace transform. This facilitates to see the correspondence between the seed perturbations and the fluctuations at the shock. We employ some assumptions for simplicity: we neglect cooling and heating and use a polytropic equation of state; we consider only the gravity of the proto-neutron star that is approximated by a point mass; the background flow is assumed to be a spherically symmetric supersonic Bondi accretion flow. These assumptions are justified for the current purpose.

In this chapter we give perturbations initially at a certain radius, possibly corresponding to Si/O shells, and see how they evolve as they flow inwards. This is in sharp contrast to the ordinary linear analysis. In fact, perturbations do not grow exponentially in time at any fixed point in the current problem. They grow in space. Our analysis is better suited for such problems. We are interested in the amplification factor of perturbations when they reach the shock wave. As shown later in this

chapter, they are oscillating in time and the typical frequencies are similar to those of SASI. If an analogy with forced oscillations holds true, these amplified perturbations may enhance the SASI activity in turn. The dependence of the amplification factor on l, the index of the spherical harmonics $Y_{lm}(\theta, \phi)$, is obtained and is found to be different from those claimed by LG00 and Kovalenko & Eremin (1998), who treated the asymptotic regime ($r \to 0$).

The chapter is organized as follows. In the next section, we give the basic equations with the assumptions mentioned above, and we introduce the Laplace transform method that facilitates the solution of the linearized partial differential equations. We also set the model-parameters in this section. The results are presented in Sec. 2.3 and discussions are given in Sec. 2.4. Finally, we summarize our findings in Sec. 2.5.

2.2 Method

As stated in the introduction, we study the evolution of the perturbations that are initially given at a certain radius. Since we have in mind the application to the post-bounce phase of CCSNe, we focus on the amplification factor and its time-dependence at a certain radius downstream, corresponding to the shock position. We study it by linear analysis although the fluctuations may become nonlinear in reality if they grow sufficiently. For such a purpose, Laplace transform is quite useful as shown in section 2.2.2. We apply it to the linearized equations that govern the evolution of perturbations in supersonic accretion flows and are derived in section 2.2.1. At the end of this section, we introduce models and parameters employed in this paper.

2.2.1 basic equations

We consider supersonic accretion flows, which approximate the matter flows outside the standing shock wave in the post-bounce phase of CCSNe. We neglect the self-gravity of the accreting matter and take into account only the gravity of the central accretor, which mimics a proto-neutron star, and of matter inside the shock wave. This is not a bad approximation since the accretor mass is indeed dominant. Since cooling and heating via neutrinos are negligible, we assume that the flows are adiabatic and employ a polytropic equation of state. We note that nuclear burnings, which are also neglected just for simplicity in this study, may actually affect the dynamics. This issue will be addressed elsewhere.

Under these assumptions, the governing equations are given as follows.

$$\frac{\partial \rho}{\partial t} + \nabla \cdot (\rho \mathbf{v}) = 0, \tag{2.1}$$

$$\frac{\partial}{\partial t}(\rho v_i) + \nabla_j (\rho v_i v^j + \delta_i^j p) = -\rho \frac{GM}{r^2}\frac{r_i}{r}, \tag{2.2}$$

$$p = K\rho^\gamma, \tag{2.3}$$

where ρ, p, $\mathbf{v}$, γ, and K are the density, pressure, velocity, ratio of specific heats and polytropic coefficient, respectively. G and M are the gravitational constant and mass of the central object, respectively.

As repeatedly mentioned, we consider fluctuations to a spherically symmetric, transonic Bondi accretion flow, which is a time-independent solution of Eqs. (2.1)-(2.3). Following LG00, we linearize above equations and express the perturbations as

$$\delta\rho(\mathbf{r}, t) = \delta\rho(r, t) Y_{lm}(\theta, \phi), \tag{2.4}$$

$$\begin{aligned}\delta\mathbf{v}(\mathbf{r}, t) = {} & \delta v_r(r, t) Y_{lm}(\theta, \phi)\hat{\mathbf{r}} \\ & + \delta v_\perp(r, t)\left[\hat{\theta}\frac{\partial Y_{lm}}{\partial \theta} + \frac{\hat{\phi}}{\sin\theta}\frac{\partial Y_{lm}}{\partial \phi}\right] + \delta v_{rot}(r, t)\left[-\hat{\phi}\frac{\partial Y_{lm}}{\partial \theta} + \frac{\hat{\theta}}{\sin\theta}\frac{\partial Y_{lm}}{\partial \phi}\right],\end{aligned} \tag{2.5}$$

where $Y_{lm}(\theta, \phi)$ is the ordinary spherical harmonics and $\hat{\mathbf{r}}, \hat{\theta}$, and $\hat{\phi}$ are unit vectors in spherical coordinates. Then the system of linearized equations is given as

$$\frac{\mathrm{D}}{\mathrm{D}t}\delta\rho + \frac{\delta\rho}{r^2}\frac{\mathrm{d}}{\mathrm{d}r}(r^2 v_r) + \frac{1}{r^2}\frac{\partial}{\partial r}(\rho r^2 \delta v_r) - \frac{\rho}{r} l(l+1)\delta v_\perp = 0, \tag{2.6}$$

$$\frac{\mathrm{D}}{\mathrm{D}t}\delta v_r + \frac{\mathrm{d}v_r}{\mathrm{d}r}\delta v_r + \frac{\partial}{\partial r}\left(\frac{\delta p}{\rho}\right) = 0, \tag{2.7}$$

$$\frac{\mathrm{D}}{\mathrm{D}t}(r\delta v_\perp) + \frac{\delta p}{\rho} = 0, \tag{2.8}$$

$$\frac{\mathrm{D}}{\mathrm{D}t}(r\delta v_{rot}) = 0, \tag{2.9}$$

$$\delta p = \gamma K \rho^{\gamma-1}\delta\rho, \tag{2.10}$$

where $\mathrm{D}/\mathrm{D}t := \partial/\partial t + v_r \partial/\partial r$ denotes the Lagrange derivative. We note that Eq. (2.9) is decoupled from others and can be solved immediately as follows:

$$\delta v_{rot}(r, t) = \frac{R}{r}\delta v_{rot,R}\left(t - \int_R^r \frac{\mathrm{d}r'}{v_r(r')}\right)\theta\left(t - \int_R^r \frac{\mathrm{d}r'}{v_r(r')}\right), \tag{2.11}$$

where R is the radius of the outer boundary and the boundary value $\delta v_{rot,R}(t)$ is imposed there. $\theta(t)$ denotes the step function. The solution means that the perturbation δv_{rot} is simply advected inwards, increasing its amplitude as $\propto r^{-1}$.

2.2.2 Laplace transform

We introduce here an idea to solve the linearized partial differential equations by Laplace transform. Although finite difference methods are more often employed to solve hyperbolic partial differential equations, we prefer Laplace transform. As will be seen below, this method is particularly suitable for our interest: by what factor does the perturbation imposed at a certain point will grow during the advection to a specified point?

Laplace transform with respective to t is symbolically expressed by an operator $\mathcal{L}$ and defined as follows (e.g. Schiff, 1999):

$$f^*(s) := \mathcal{L}[f(t)](s) := \int_0^\infty f(t)e^{-st}\mathrm{d}t, \tag{2.12}$$

where $f(t)$ is a function of t, for which Laplace transform exists for some complex number, s. The advantage in the use of Laplace transform is that the partial differential equations are reduced to ordinary differential equations with respective to r thanks to the relation:

$$\mathcal{L}\left[\frac{\partial f}{\partial t}\right] = s\mathcal{L}[f] - f(0^+), \tag{2.13}$$

in which the second term on the right hand side is the initial values of f at $t = 0$. Note that the r-dependence is omitted in the above equation for notational simplicity. Laplace transforming the linearized equations (2.6)-(2.8), we obtain the following

equations:

$$\frac{\mathrm{d}}{\mathrm{d}r}\left(\frac{\delta\rho^*(r,s)}{\rho}\right) = \frac{1}{1-\mathcal{M}^2}\left\{\left(\frac{s\mathcal{M}}{c_s}+\mathcal{M}^2\frac{\mathrm{d}}{\mathrm{d}r}\ln\dot{M}-\frac{\gamma-1}{\rho}\frac{\mathrm{d}\rho}{\mathrm{d}r}\right)\frac{\delta\rho^*}{\rho} + \left[-\frac{s\mathcal{M}}{c_s}+\mathcal{M}^2\left(\frac{\mathrm{d}}{\mathrm{d}r}\ln\dot{M}-\frac{2}{v_r}\frac{\mathrm{d}v_r}{\mathrm{d}r}\right)\right]\frac{\delta v_r^*}{v_r}-\mathcal{M}^2\frac{l(l+1)}{r}\frac{\delta v_\perp^*}{v_r}\right\}, \quad (2.14)$$

$$\frac{\mathrm{d}}{\mathrm{d}r}\left(\frac{\delta v_r^*(r,s)}{v_r}\right) = \frac{1}{1-\mathcal{M}^2}\left[\left(-\frac{s}{v_r}-\frac{\mathrm{d}}{\mathrm{d}r}\ln\dot{M}-\frac{\gamma-1}{\rho}\frac{\mathrm{d}\rho}{\mathrm{d}r}\right)\frac{\delta\rho^*}{\rho} + \left(\frac{s\mathcal{M}}{c_s}-\frac{\mathrm{d}}{\mathrm{d}r}\ln\dot{M}+\frac{2\mathcal{M}^2}{v_r}\frac{\mathrm{d}v_r}{\mathrm{d}r}\right)\frac{\delta v_r^*}{v_r}+\frac{l(l+1)}{r}\frac{\delta v_\perp^*}{v_r}\right], \quad (2.15)$$

$$\frac{\mathrm{d}}{\mathrm{d}r}\left(\frac{\delta v_\perp^*(r,s)}{v_r}\right) = -\frac{1}{r\mathcal{M}^2}\frac{\delta\rho^*}{\rho}-\left(\frac{s}{v_r}+\frac{1}{r}+\frac{1}{v_r}\frac{\mathrm{d}v_r}{\mathrm{d}r}\right)\frac{\delta v_\perp^*}{v_r}, \quad (2.16)$$

where variables with a suffix $*$ are the quantities that are Laplace transformed with respect to t; $\dot{M}(:= 4\pi r^2\rho v_r)$ is the mass accretion rate; $c_s(:=\sqrt{\gamma\quad})$ is the sound speed and $\mathcal{M}(:=\ _r\quad _s$. In deriving these equations, we assume that the initial perturbations are zero except at the outer boundary because we suppose that the fluctuations are initially confined in the convective zone in the outer envelope of the progenitor and will fall onto the stalled shock wave later.

We emphasize here that Eqs. (2.14)-(2.16) form a system of ordinary differential equations with respect to r with s being a parameter. The integration of the equations is then much facilitated by the use of e.g. the Runge-Kutta method. As mentioned above, perturbations are generated at the outer boundary and given as the boundary condition there in our formulation. For example, if the perturbation is given as $f(t,R)=\sin(\omega t)$, then its Laplace transform, $\mathcal{L}[\sin(\omega t)]=\omega/(s^2+\omega^2)$, is used as the boundary value for each s.

Integrating the Laplace transformed equations from the outer boundary to the inner boundary, which corresponds to the shock radius in the CCSNe context, we obtain the Laplace transformed quantities at the inner boundary for a given value of s. Collecting these quantities for a set of s, we can recover the corresponding time

evolutions of these variables at the inner boundary via the inverse transform formula:

$$f(t) = \mathcal{L}^{-1}[f^*(s)], \tag{2.17}$$

$$= \lim_{y\to\infty} \frac{1}{2\pi i} \int_{x-iy}^{x+iy} f^*(s) e^{st} \mathrm{d}s, \tag{2.18}$$

$$= \frac{e^{tx}}{2\pi} \int_{-\infty}^{\infty} f^*(x,y) e^{iyt} \mathrm{d}y, \tag{2.19}$$

where x and y are the real and imaginary parts of s, respectively.[3] In these expressions, x is a fixed number and the integral path is a line parallel to the imaginary axis. In fact, x is arbitrary as long as the Laplace transform of $f(t)$ is defined for s. Note that the integral on the right hand side is nothing but a Fourier transform and can be performed efficiently by Fast Fourier Transform. It is also mentioned that if $f(t)$ is a real function, the real and imaginary parts of $f^*(s)$ are even and odd functions, respectively. This is indeed the case for our current problem, since we are dealing with the perturbations of real quantities. We can then reduce the integral domain by half. In the numerical evaluations, the integral domain is enlarged until we see a convergence. Other technical details in numerical evaluations are given in Appendix A.1.

2.2.3 models and parameters

As mentioned repeatedly, we have in mind the application of our models to the post-bounce phase of CCSNe. We hence employ the transonic, spherical Bondi accretion flow as an unperturbed state in order to mimic the infall of the outer envelope onto the stalled shock wave. Only the supersonic portions of the transonic flows are adopted in our models. We set the inner boundary at $200 - 400$ km from the center, roughly corresponding to the radius of the stagnant shock wave in the post-bounce core of CCSNe. The outer boundary approximately coincides with the position of Si/O layer.

The canonical values of model parameters to specify a background flow are as follows: the density at the sonic point $\rho_c = 1 \times 10^7$ g cm^{-3}, mass accretion rate $\dot{M} = 1$ M$_\odot$ s^{-1}, ratio of specific heats $\gamma = 1.6$, mass of the accretor $M_{cen} = 1.4$ M$_\odot$, and radius of the inner boundary $r_{sh} = 3 \times 10^7$ cm. In this model, the radius of the sonic point is given as $r_c = 1.39 \times 10^8$ cm, and the sound speed at that point is $c_{sc} = 8.20 \times 10^8$ cm s^{-1}, and the Bernoulli constant is $E = 1.12 \times 10^{17}$ g cm^2 s^{-2}. The constant in the polytropic equation of state is given as $K = 2.65 \times 10^{13}$ in CGS units.

[3] As a matter of fact, we can obtain the time evolution at any point in the same way.

These parameters are tuned to approximate the collapse of 15 $M_\odot$ progenitor model by Woosley & Heger (2007) (see also Yamamoto et al., 2013), which is thought to be a typical progenitor of CCSNe and commonly used in the literature. The profiles of this model are displayed in Fig. 2.1. Note that the mass of accreting matter is 0.1 $M_\odot$, which is much smaller than the mass of central accretor, 1.4 $M_\odot$. This justifies the neglect of self-gravity in our model. In fact, the background flow changes at most 10 per cent if we take fully into account the self-gravity of accreting matter.

In reality, the infall velocities around Si/O layer, the region that produces perturbations, will be subsonic. We do not include the subsonic part of the Bondi accretion flow in this study, however, to avoid numerical complexities in treating the sonic point. Unless the perturbations are suppressed substantially in this subsonic portion, which is rather unlikely, the conclusion of this paper is not changed.

As mentioned already, we impose perturbations at the outer boundary as a time-dependent boundary condition. Since the background flow is supersonic, no boundary condition is needed at the inner boundary. As for the functional form of the outer boundary condition, we consider a step-function, $\theta(t)$, and a sinusoidal function, $\sin(\omega t)$.

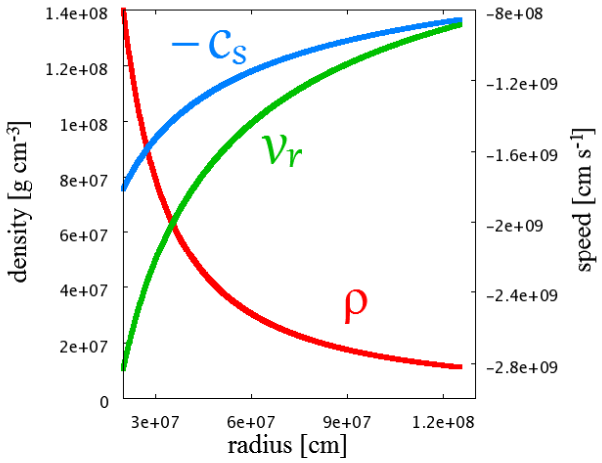

Figure 2.1: The background flow (the transonic Bondi accretion flow) for the canonical parameter set. The blue, green, and red lines represent the sound speed (multiplied by -1), flow velocity and density, respectively.

2.3 Results

In this section, we show the time evolutions of the perturbations as well as their systematics. As mentioned previously, the results are obtained by integrating the Laplace transformed equations (2.14)-(2.16) numerically from the outer boundary located near the sonic point to the inner boundary for a set of s and then inverse-transforming the quantities so obtained into the counterparts in the real-time domain by Eq. (2.17). In the following we first present the time evolutions for the step-function type outer boundary condition, for which the causality is demonstrated most clearly. Then we give a more realistic case, in which we impose a sinusoidal time-variations in all quantities at the outer boundary.

2.3.1 step-function type perturbations

We present firstly the time evolutions at $r_{sh} = 300$ km in the canonical model. The density of perturbations and radial-velocity perturbations are set at the outer boundary $r = R = 1.25\times10^8$ cm as a step function in time. Since the background flow is spherically symmetric and the perturbations are decomposed with the spherical harmonics, different l-modes are considered separately.

We begin with spherical modes with $l = 0$. In this case, the transverse components of velocity vanish everywhere at any time. We present the result in Fig. 2.2, in which the vertical axis is the perturbations normalized by the values at the outer boundary whereas the horizontal axis represents the time from the instance when the perturbation is imposed at $r = R$. As seen in the figure, the perturbations reach r_{sh} with a delay, which is estimated as

$$t_1 = \int_R^{r_{sh}} \frac{\mathrm{d}r'}{\lambda(r')} = 41.5 \text{ ms}, \tag{2.20}$$

where $\lambda(r)$ denotes the velocity of the in-going acoustic wave: $v_r - c_s$. Since the background flow is supersonic everywhere, the other two characteristic velocities, $v_r + c_s$ and v_r, are also negative. It is also evident in the figure that the perturbations become steady after $t_3 = 783$ ms, which corresponds to the time, at which a wave that has the slowest characteristic velocity, $v_r + c_s$, reaches r_{sh}. The perturbation increases monotonically in the case of density. It is doubled quickly in less than 200 ms and nearly tripled finally in the steady state. The radial velocity grows much slowly and the amplification factor reaches only ~ 1.25 in the steady state.

Fig. 2.3 represents the results for $l = 1, 4, 5, 10, 15$, and 20. For $l = 20$, for example, the amplification factor reaches ~ 30 for the density perturbation and it

goes up to ~ 15 for the radial-velocity perturbation in the steady state established after t_3. For these modes, the transverse components of velocity are also perturbed as $\delta v_\perp / v_r = \delta v_{rot} / v_r \propto \theta(t)$ at the outer boundary. As mentioned in Sec. 2.2.1, δv_{rot} is not coupled with other perturbations and is obtained by Eq. (2.11). As a matter of fact, for the step-function type perturbation assumed in this section, $\delta v_{rot}/v_r$ also becomes a step function in time with a discontinuity at $t = t_2$ given by

$$t_2 = \int_R^{r_{sh}} \frac{\mathrm{d}r'}{v_r(r')}. \tag{2.21}$$

The time evolutions of other variables, on the other hand, change qualitatively as l increases. Firstly, in contrast to the $l = 0$ case, the density and radial-velocity perturbations have another transition at t_2 (see Fig. 2.4 for close-ups). This may seem strange, since the eigenfunction that corresponds to the eigenvalue, v_r, contains only $\delta v_\perp$ and hence $\delta\rho$ and δv_r appear to have nothing special at t_2. This is not true, however, and these modes are actually mixed because the background flow is non-uniform spatially and, as a consequence, the eigenvectors vary radially.

Secondly, the perturbations oscillate in time between t_1 and t_3. Although these oscillations are not harmonic, their frequencies are roughly in the range of $40 - 100$ s^{-1} for $l = 1 - 20$ between t_1 and t_2 and they become higher as l increases. The oscillations continue after t_2 but the frequencies get lower as the time passes: the interval between nodes are $14, 19, 25, 35, 51$, and 93 ms for $l = 20$ while those for $l = 10$ are $32, 58$, and 128 ms. In general, the number of nodes and the intervals between them are larger and shorter, respectively, for greater l's.

Thirdly, as l becomes larger, the amplitudes of the density and radial-velocity perturbations tend to get larger. It is analytically shown in Appendix A.2 that for large l's the saturated amplitudes are proportional to l for density and radial-velocity perturbations while those for the transverse velocities are independent of l. Note that these dependences are different from those claimed by LG00 or Kovalenko & Eremin (1998) for the asymptotic regime ($r \to 0$). These authors assumed that the amplitudes obey a power law of r in this asymptotic regime ($r \to 0$) and deduced the dependence of $\propto l^2$.

So far we have fixed the inner boundary to $r = 300$ km. We turn our attention to the dependence of the amplification factors on this radius. In Fig. 2.5, we plot the normalized perturbation amplitudes in the steady state at $t \geq t_3$ as a function of radius. As is evident, there are nodes in general, whose number becomes larger as l increases, and the perturbation growth in space is never described by a simple power law of radius as assumed in the previous analyses by Kovalenko & Eremin (1998) and LG00. The radial variation may be better approximated by a sinusoidal

wave. Note, however, that we are not dealing with the asymptotic regime ($r \to 0$) unlike these authors. It is important that the amplitudes of the radial oscillations are largest for the density perturbation and those for the radial-velocity perturbation is second largest. More quantitative discussions on the radial oscillations are found in Appendix A.2.

We also plot the maximum amplification factors, which are not necessarily attained in the steady state, at each radius in Fig. 2.6. The lines for $\delta v_{rot}/v_r$ are identical in Figs. 2.5 and 2.6 for the reasons mentioned above. The plots for other variables are rather complicated and radial variations are sometimes rectangular rather than sinusoidal. For larger l's, however, Figs. 2.5 and 2.6 become similar to each other, indicating that the maximum amplification factor is attained after the steady state is reached in these cases.

We note finally that the above features are not altered both qualitatively and quantitatively even if only $\delta v_\perp$ is non-vanishing at the outer boundary, which is the situation considered in Couch & Ott (2013). This is because the mode mixing explained earlier produces the density and radial-velocity perturbations.

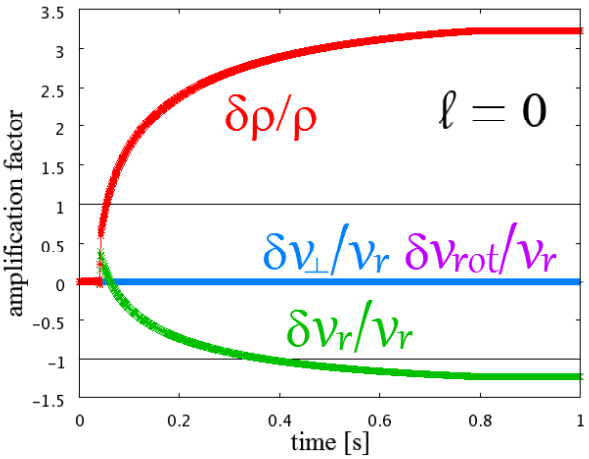

Figure 2.2: The time evolutions of the $l = 0$ perturbations at the radius of 300 km. The step-function type perturbations are imposed at the outer boundary. The vertical axis is the amplification factors, i.e. the ratio to the values set at the outer boundary. The red, green, blue, and purple lines represent the perturbations of density, radial-velocity, and transverse components of velocity, respectively. Two horizontal black lines represent ± 1.

2.3.2 sinusoidal perturbations

Although it facilitates the interpretation of results, the step-function type boundary condition adopted in the previous section is admittedly artificial. In this section we consider the models, in which a sinusoidal variation: $\delta\rho/\rho = \delta v_r/v_r = \delta v_\perp/v_r = \delta v_{rot}/v_r \propto \sin(\omega t)$, is assumed in the outer boundary condition. Here we set the angular frequency as $\omega = 2$ s^{-1}, which is approximately the inverse of the sound crossing time in the Si layer of the 15 $M_\odot$ progenitor. The background model is not changed from the one in the previous section. We have repeated the same analysis for this model. We present here only the time evolutions of normalized perturbation amplitudes at $r_{sh} = 300$ km in Fig. 2.7. Much like in the previous case, the perturbations oscillate rapidly in the early phase and grow later over the timescale of $\sim \omega^{-1}$. In contrast to the step-function type perturbations, however, perturbations at a fixed point do not become steady but oscillate in a harmonic manner after t_3.

We now turn our attention to the dependence of the amplification factors on the radius of the inner boundary. Fig. 2.8 shows the r-dependence of the magnitudes of amplification factors in the late phase, when the perturbations attain the harmonic oscillations at the inner boundaries. We again observe the same features as those in the previous section: the perturbation growth in space is never fitted by a simple power la lification factors are largest for density and those for radial velocity is second largest.

Although we have not investigated them, we believe that these features will be unchanged for other ω.

2.4 Discussions

2.4.1 comparisons with the previous results

LG00 investigated the linear stability of supersonic accretion flows both analytically and numerically. In their analytic treatment, they considered only the asymptotic region, $r \to 0$, assuming a simple power law for the growth of perturbations. It is stressed that we are not dealing with this regime in this paper. In fact, since we have in mind the application of the results to the post-bounce phase of CCSNe, the inner boundary in this paper roughly corresponds to the stagnant shock wave in the supernova core and is rather distant ($\sim$ 100 km) from the center. We should be aware of this difference in the following comparison. It is also noted that we

neglect self-gravity whereas it was included in LG00.[4] As mentioned already, we do not find the power-law behavior in our model. We observe instead the oscillations in the spatial profile of the perturbation amplitudes. In the following we show that the envelopes of these oscillations obey power laws (see also Appendix A.2). Even in that case, however, the powers we obtain are different from those reported in the previous papers as demonstrated below.

We first give the result of LG00 shortly. From Eqs. (7), (22)-(25) in their paper, the perturbation growths are obtained in the asymptotic limit ($r \to 0$) as

$$\frac{\delta\rho}{\rho} \propto 2l(l+1)\frac{\delta v_\perp}{v_r} \propto 2l(l+1)r^{-1/2}, \tag{2.22}$$

$$\frac{\delta v_r}{v_r} \propto r^{-(3\gamma-4)/2}, \tag{2.23}$$

$$\frac{\delta v_\perp}{v_r} \propto r^{-1/2}, \tag{2.24}$$

$$\frac{\delta v_{rot}}{v_r} \propto r^{-1/2}, \tag{2.25}$$

under the assumption that the flow velocity in the background is $v_r \propto r^{-1/2}$.[5] Applying these relations to the entire region, we obtain the amplification factors as $8, 1.8, 2$, and 2 for $\delta\rho/\rho, \delta v_r/v_r, \delta v_\perp/v_r$, and $\delta v_{rot}/v_r$, respectively, if we adopt $R = 1.25 \times 10^8$ cm, $r_{sh} = 3 \times 10^7$ cm, $l = 1$ and $\gamma = 1.6$.

Now we use equations (2.11) and (A.19)-(A.21) in Appendix A.2 to obtain the perturbation amplitudes for large l's after the steady state is established. Note that the perturbation amplitudes in this steady state are not very different from the maximum values. Assuming that the velocity is proportional to $r^{-1/2}$ as LG00 did in the asymptotic limit of $r \to 0$, we obtain $\mathcal{M} \propto r^{-(5-3\gamma)/4}$ in the Bondi accretion flow.

[4] As already mentioned, the mass of accreting matter is less than 10 per cent of the central accretor in our canonical model. It is hence expected that the following results may be subject to change as much if self-gravity is taken into account.

[5] They further imposed the irrotational condition $\delta v_T := \delta v_r - \partial(r\delta v_\perp)/\partial r \equiv 0$, which is justified since the right hand side is proportional to $\sqrt{r}$ as $r \to 0$ anyway.

Inserting these relations to Eqs. (2.11) and (A.19)-(A.21), we have the following.

$$\frac{\delta\rho}{\rho} \propto lr^{-(5-3\gamma)/4}, \tag{2.26}$$

$$\frac{\delta v_r}{v_r} \propto lr^{(5-3\gamma)/4}, \tag{2.27}$$

$$\frac{\delta v_\perp}{v_r} \sim \text{const.}, \tag{2.28}$$

$$\frac{\delta v_{rot}}{v_r} \propto r^{-1/2}. \tag{2.29}$$

It should be mentioned that Eqs. (A.19)-(A.21) are obtained under the assumption that the Mach number is almost constant and hence are not applicable to the present case with $\mathcal{M} \propto r^{-(5-3\gamma)/4}$, rigorously speaking. However, the r-dependence of $\mathcal{M}$ is rather weak and the local application of Eqs. (A.19)-(A.21) may be justified. As a matter of fact, the l-dependence obtained this way reproduces the numerical results fairly well as shown in Fig. 2.9.

It is evident from the comparison with Eqs. (2.22)-(2.24) that both the power and l-dependence are different. In fact, the power for $\delta\rho/\rho$, $-(5-3\gamma)/4$, is larger than $-1/2$ expected in LG00 as long as $\gamma > 1$, which is expected in CCSNe. Taking into account the difference of the l-dependence, in addition, it turns out that the amplification factor at the inner boundary assumed in the paper will be much smaller than expected by the previous study for large l's. As for $\delta v_r/v_r$, since the power in Eq. (2.27) is positive for $\gamma < 5/3$ and larger than that in Eq. (2.23) for $\gamma > 1$, $\delta v_r/v_r$ will be decreased faster than supposed in LG00. The reason for the decrease in the perturbation amplitude is just more rapid increases in the background velocity. Note that this is true only near the inner boundary and $\delta v_r/v_r$ increases at the beginning. Combined with the l-dependence, the amplification factor can become much larger than unity as shown in Fig. 2.6. Finally, $\delta v_\perp/v_r$ is not amplified according to Eq. (2.28), which is in sharp contrast to the prediction in LG00 that it is inversely proportional to the square root of r. Fig. 2.6 demonstrates that it is indeed smaller than unity for large l's.

It is finally mentioned that Kovalenko & Eremin (1998) also investigated the stability of Bondi accretion flows in the asymptotic regime and obtained $\delta v_r \propto l^2$, which is different both from our result and from the LG00. On the other hand, they found the same l-dependence for the density perturbation as LG00 did, which is different from ours as stated above.

2.4.2 possible impact on the shock dynamics in CCSNe

The above analysis suggests that the perturbations generated in the outer envelope of a massive progenitor may be amplified by an order by the time when they reach the stalled shock wave. This implies that the initial perturbation amplitudes of a few percent may be sufficient to affect shock revival. Such a number may indeed obtain in violent convections that Arnett and his company advocated (Bazan & Arnett, 1998; Asida & Arnett, 2000; Meakin & Arnett, 2006, 2007; Arnett & Meakin, 2011). As demonstrated above, since the density and radial-velocity perturbations are amplified in proportion to l, the spectrum of the initial perturbation is important to identify the dominant l. It was recently studied by Chatzopoulos et al. (2014) in their multi-dimensional simulations of oxygen shell burnings of a 15 $M_\odot$ progenitor. They reported that the power spectrum peaks at $l = 8$ (5) and then decays exponentially for the two- (three-) dimensional case. It is then expected from our study that the dominant modes that will affect most the stalled shock wave will be also those with $l \sim 8(5)$.

It is also intriguing to point out that the perturbations will oscillate in time at the shock wave with frequencies of $10 - 10^2$ s^{-1}, which are rather close to the typical frequencies of SASI (e.g. Iwakami et al., 2014a). This similarity might play some role in reviving the stagnated shock wave in Couch & Ott (2013). Further investigations are certainly warranted.

2.5 Summary

We have studied the linear growth of the perturbations that are generated at a large radius and propagate inward in a spherically symmetric supersonic accretion flow, having in mind the application to the investigation of shock revival in CCSNe. In contrast to the previous studies, we have solved the linearized equations as an initial and boundary value problem, employing Laplace transform, which enables us to obtain the amplification factor at a specified point easily.

The background flow is chosen to be a supersonic portion of a transonic Bondi accretion flow whose parameters are set to mimic the collapse of a supposedly typical supernova progenitor: the 15 $M_\odot$ star of Woosley & Heger (2007). We have considered two seed perturbations: a step-function type perturbation and a sinusoidal one. The former is more experimental and meant to elucidate the systematics.

We have found that the density and radial-velocity perturbations grow as they propagate inward. In fact, the amplification factors can be more than 10 when applied to the perturbations generated in the Si/O layer of the massive progenitor and

accreted on the stalled shock wave in the CCSN core. They are actually oscillatory in both time and space, which is in sharp contrast to the previous studies that predicted power-law behavior in the asymptotic limit ($r \to 0$). We have shown analytically that the envelopes of the oscillatory amplification factors may obey power la large l's. We have observed, however, that the powers are still different from the previous results. We have also demonstrated both analytically and numerically for large l's that the amplification factors for the density and radial-velocity perturbations are proportional to l, which is again at odds with the previous expectations. These discrepancies are most likely due to the difference in the regimes of supersonic flows, however. The previous works investigated the innermost part of the Bondi flow ($r \to 0$), in which the Mach number becomes high and varies rapidly. In this paper, on the other hand, we have studied the outer part of the same flow, at which the Mach number is close to unity and changes rather slowly. The latter regime is more appropriate for the post-bounce phase of CCSNe.

We have found that the typical oscillation frequencies of perturbations at the stalled shock wave in the CCSN core are not much different from the canonical frequencies of SASI. This may have an important implication for shock revival and will be our next target. The results of linear analysis will be reported in the next chapter.

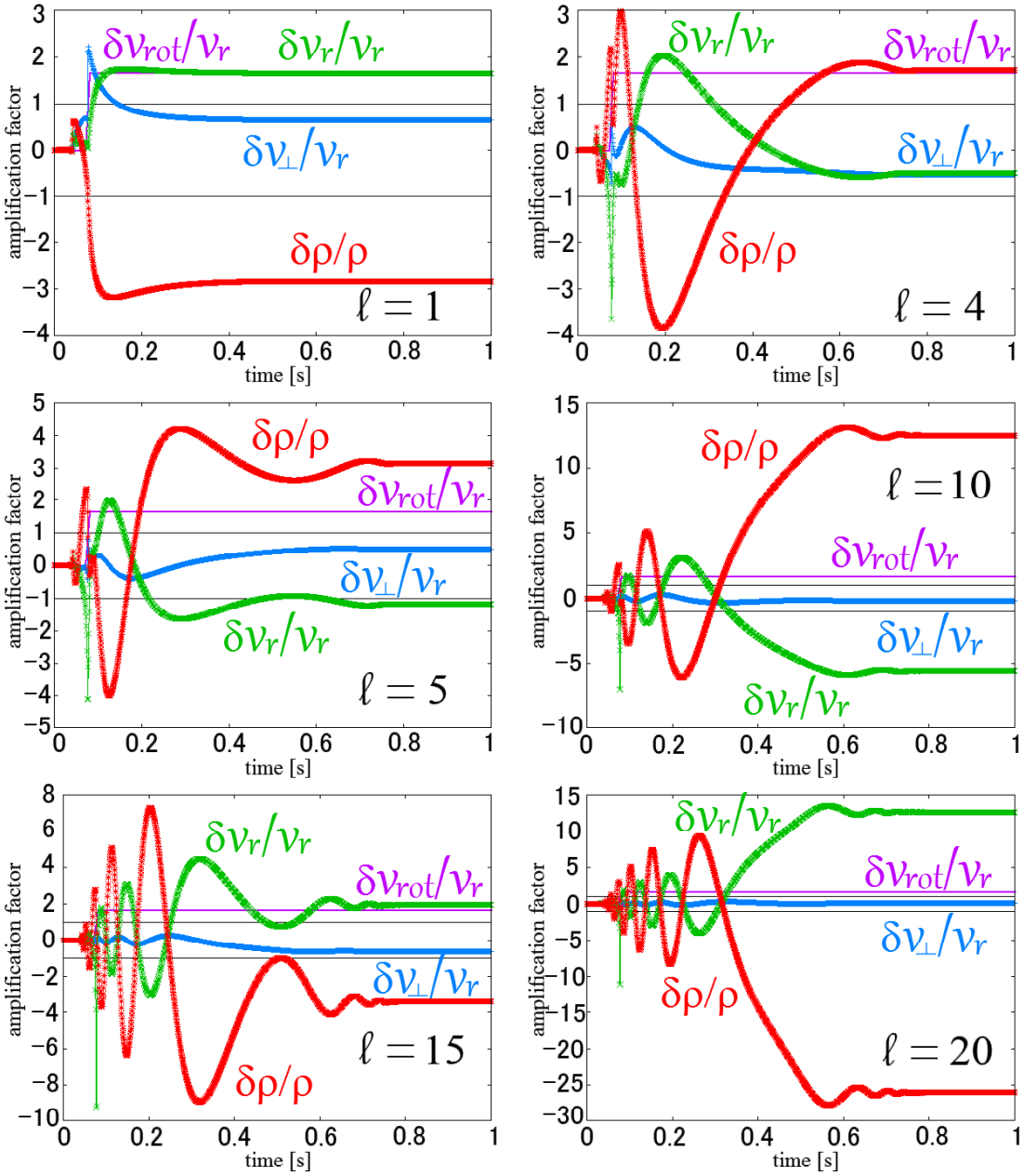

Figure 2.3: The same as Fig. 2.2 but for different l's.

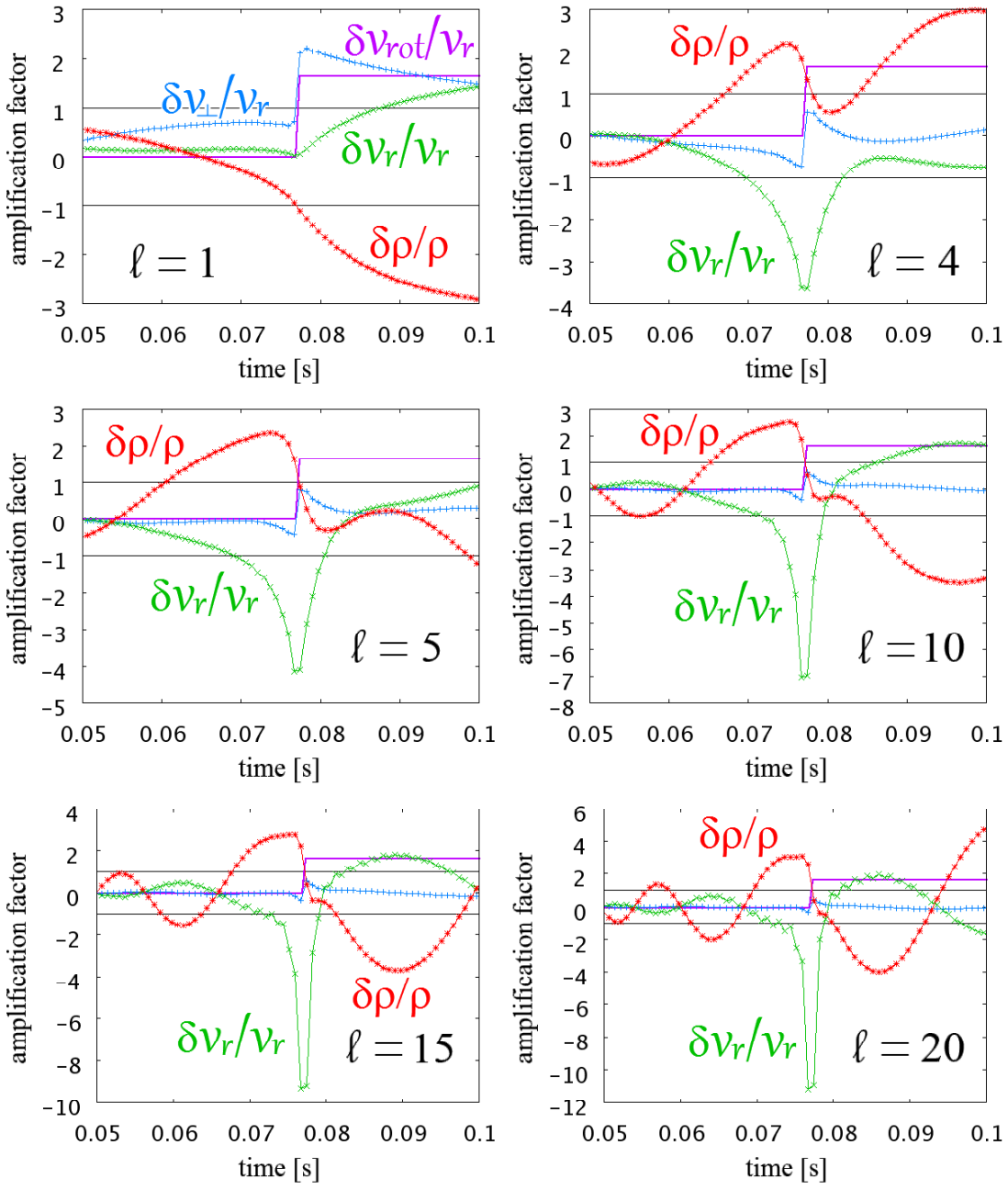

Figure 2.4: The close-ups of Fig. 2.3 around $t = t_2$.

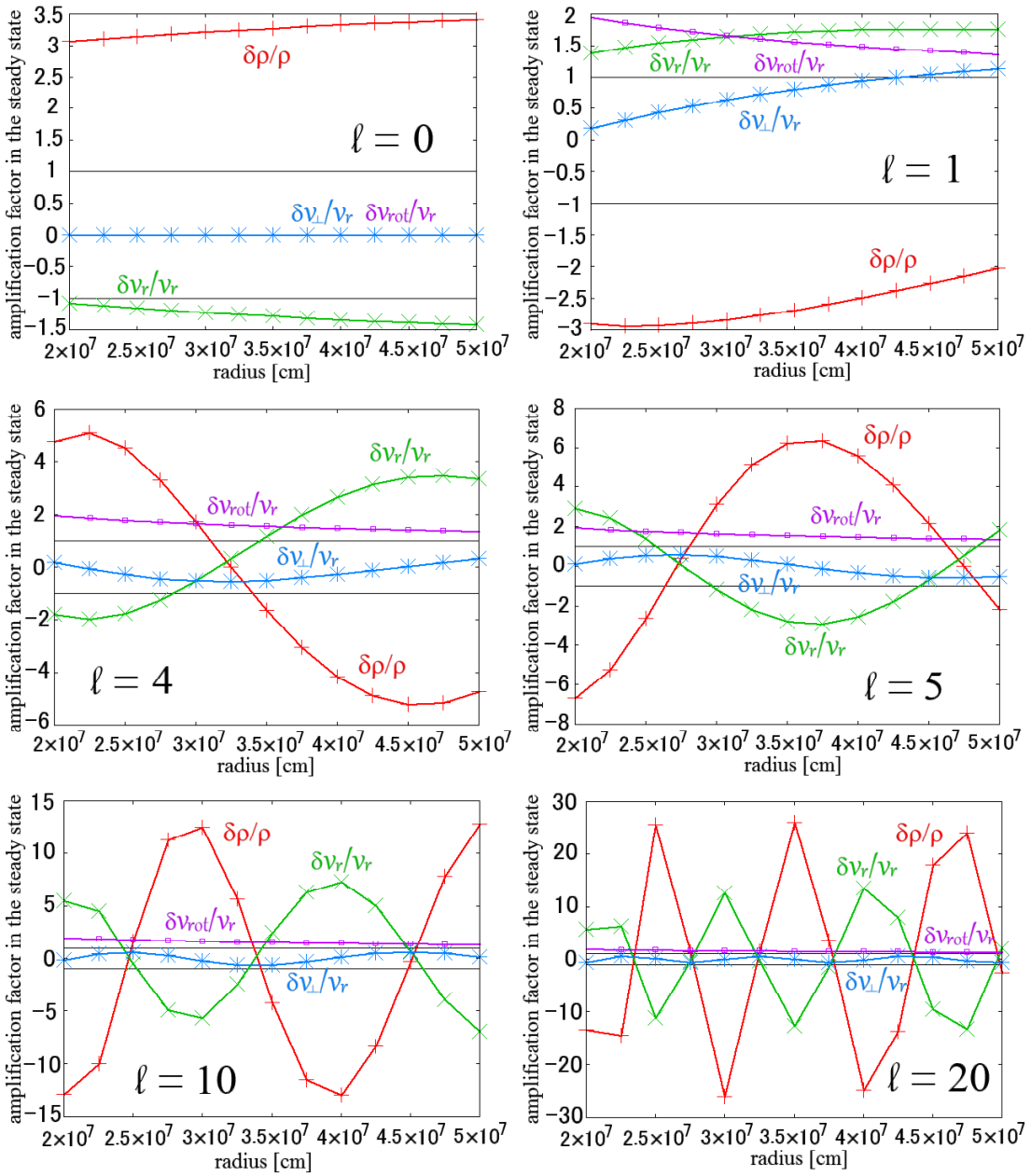

Figure 2.5: The amplification factors in the steady state as a function of radius for various l's. The red, green, blue, and purple lines represent the perturbations of density, radial-velocity, and transverse components of velocity, respectively. Two horizontal black lines represent ± 1.

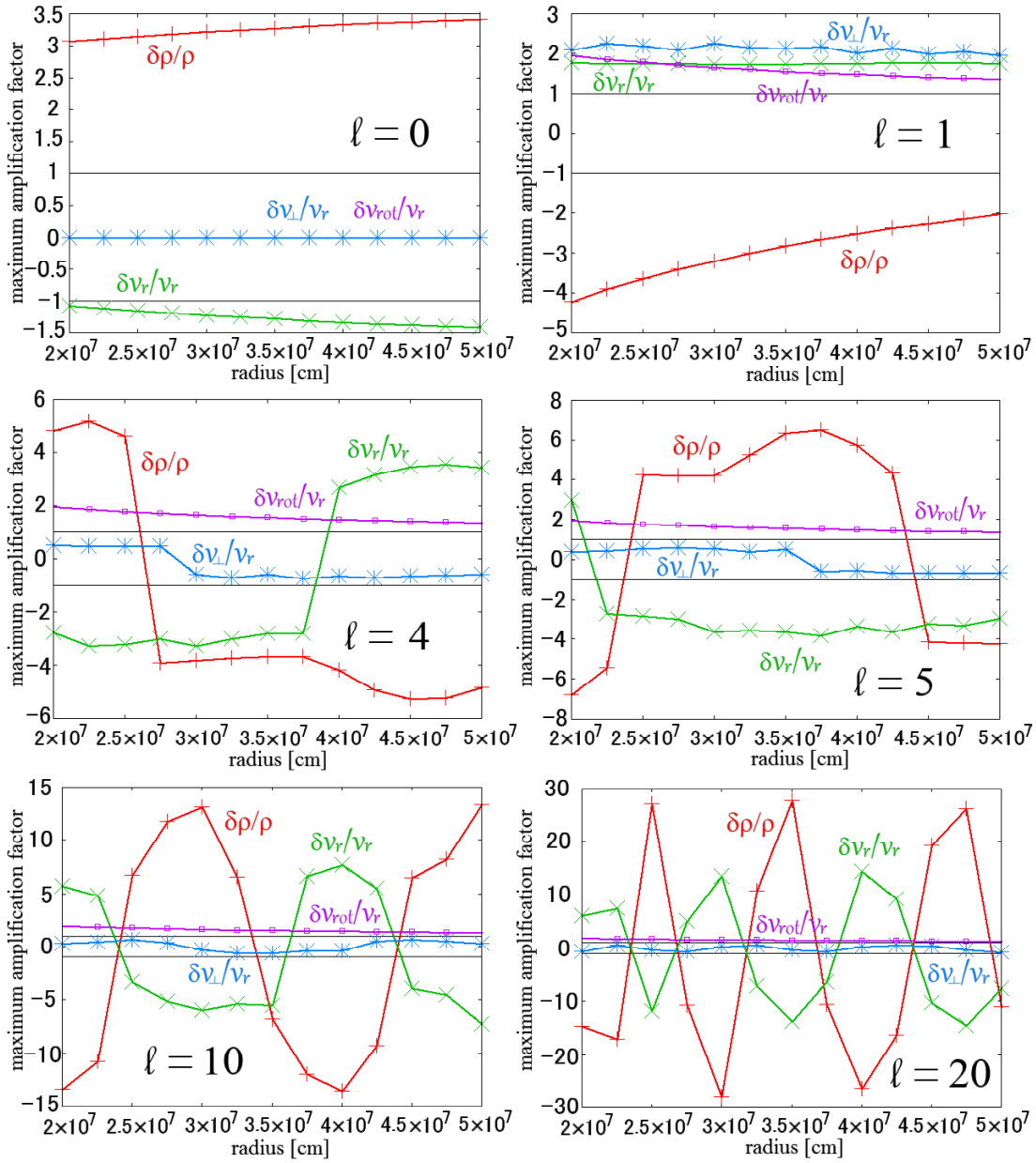

Figure 2.6: The maximum amplification factors as a function of radius for different l's. The red, green, blue, and purple lines represent the perturbations of density, radial-velocity, and transverse components of velocity, respectively. Two horizontal black lines represent ± 1.

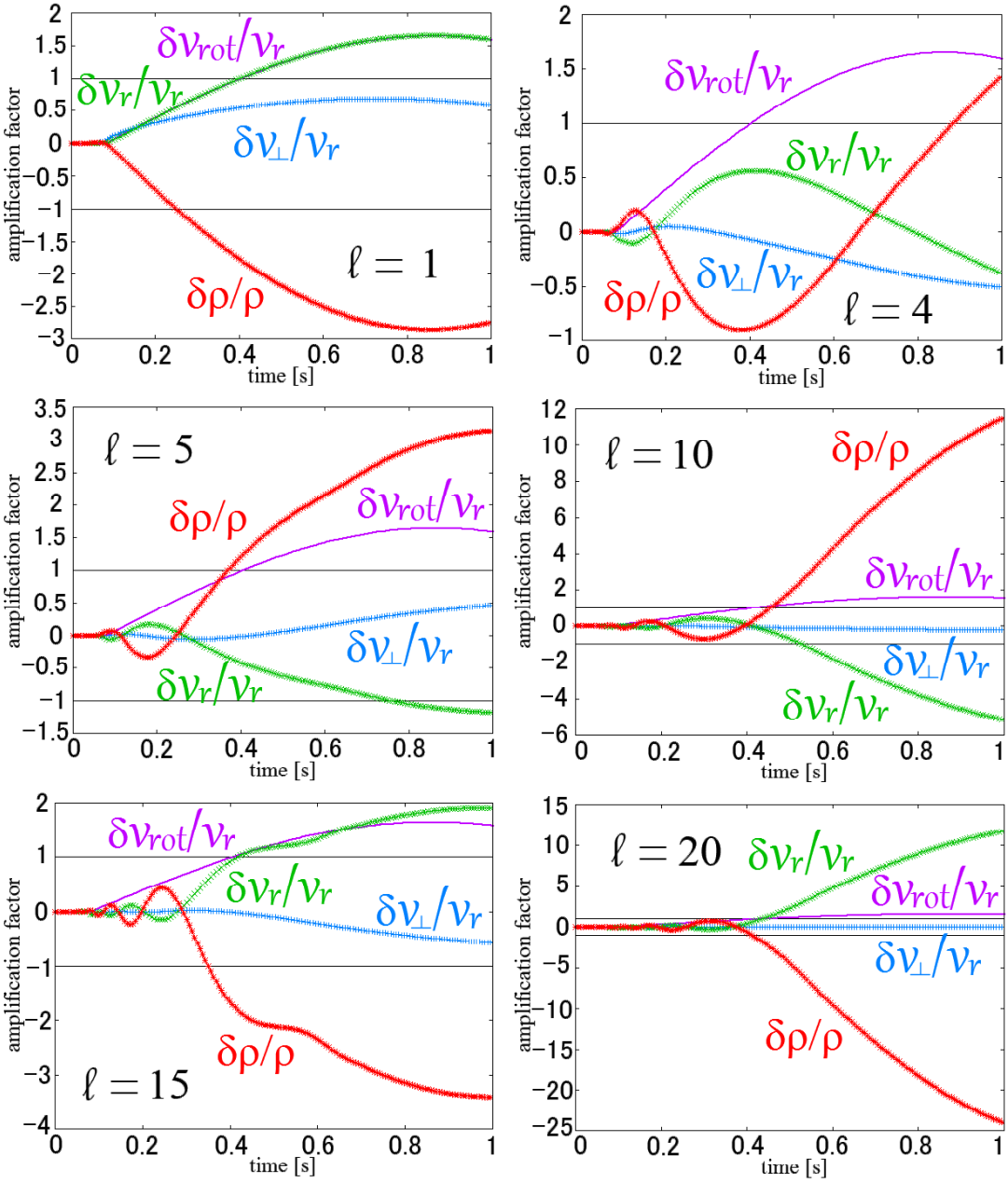

Figure 2.7: The same as Fig. 2.3 but for the sinusoidal perturbations imposed at the outer boundary.

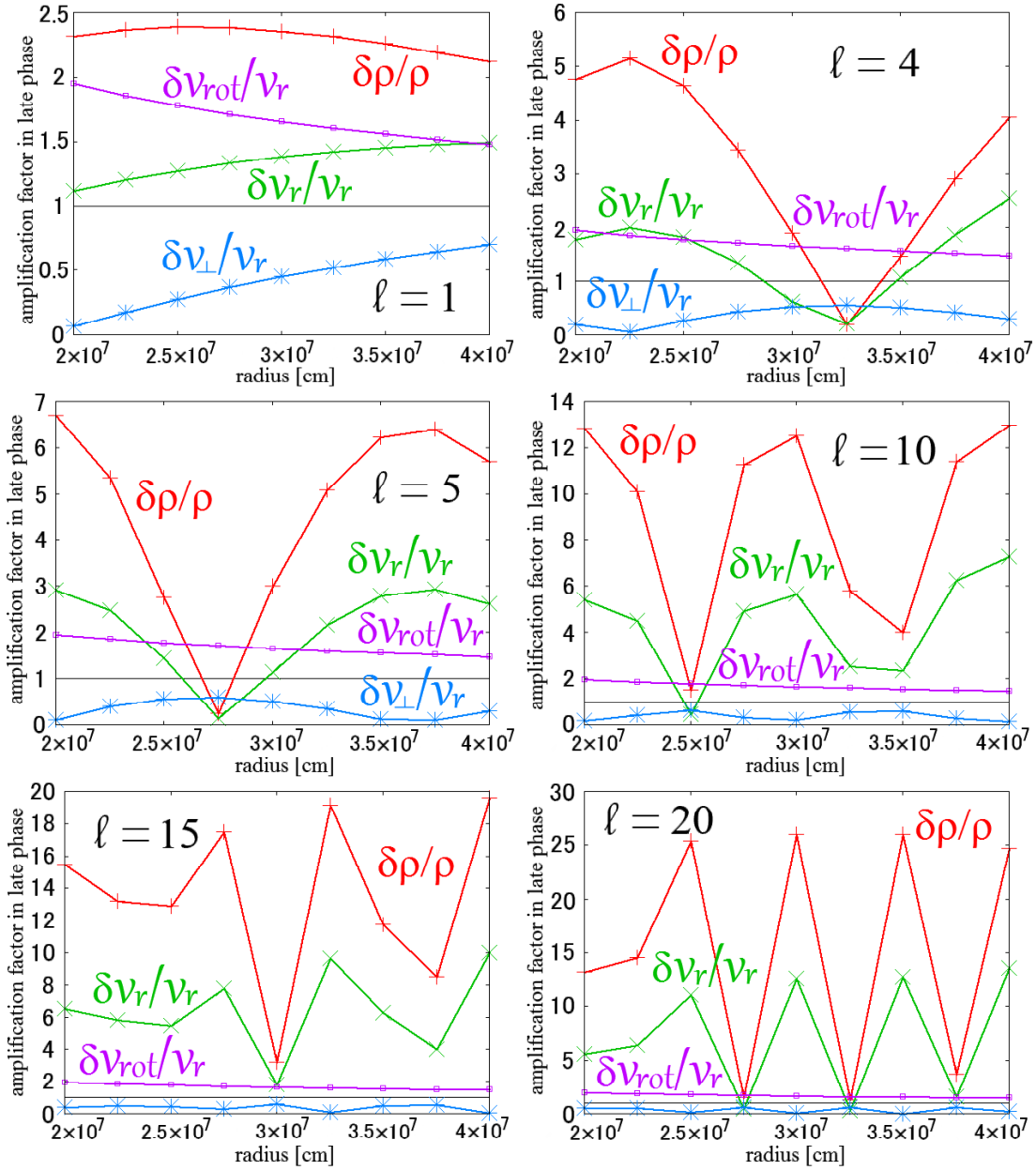

Figure 2.8: The magnitudes of amplification factors in the late phase as a function of radius for various l's. The red, green, blue, and purple lines represent the perturbations of density, radial-velocity, and transverse components of velocity, respectively. The horizontal black line represents unity.

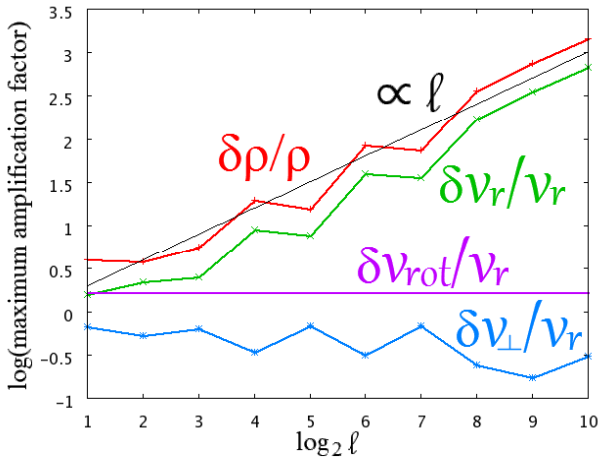

Figure 2.9: The maximum amplification factors as a function of l. The step-function type perturbations are imposed at the outer boundary. The vertical axis is in the common logarithmic scale while the horizontal axis is in the base-2 logarithmic scale. The red, green, blue, and purple lines represent the perturbations of density, radial-velocity, and transverse components of velocity, respectively. The black line is a line of $\propto l$.

Chapter 3

Analysis of the Standing Accretion Shock Instability under Non-spherical Accretion Flows

3.1 Introduction

As shown ther previous chapter, the seed perturbations that arise in the dynamical convective la

It is also found that the amplification factors are larger as the scale of fluctuations becomes smaller. In addition to the large amplitudes, they oscillate at the shock radius with frequencies that are observed in SASI simulations. These results may suggest the possibility that the fluctuations in upstream flows can affect the SASI activity. The previous studies assumed, however, that the accretion flow is a spherically symmetric steady flow (Yamasaki & Yamada, 2005, 2006, 2007; Foglizzo et al., 2007; Yamasaki & Foglizzo, 2008; Foglizzo, 2009; Sato et al., 2009; Guilet & Foglizzo, 2010, 2012). Hence we need a new analysis of SASI under non-spherical perturbed flows.

In this chapter, we perform a linear analysis to investigate the effects of such external perturbations on the shock dynamics. The problem is reduced to an eigenvalue problem as discussed below in detail. Unlike the previous studies, non-spherical time-dependent outer boundary conditions are employed. We apply Laplace transform to solve the eigenvalue problem, which turns out to work well as in the previous chapter. We perform the analysis for two different background flows and inner boundary conditions in order to study the effects of them.

This chapter is organized as follows. In Sec. 3.2, we introduce the method of our

analysis, including the basic equations and model parameters. Then we show the results in Sec. 3.3 and in Sec. 3.4. Finally we summarize our findings in Sec. 3.5.

3.2 Method

As stated in the introduction, we investigate the linear stability analysis of the standing accretion shock against the upstream perturbations. Since the SASI is a global instability, we solve the eigenvalue problem of the fluid state between the shock surface and neutrino sphere, which correspond to outer and inner boundary respectively. The linearized equations are solved with the use of the Laplace transform, which is turned out to be useful as illustrated in the previous paper.

In this section, we introduce the system of the basic equations and Laplace transformed counterpart to study the SASI. The main idea to analyze the SASI with Laplace transform is also presented.

3.2.1 basic equations

We give the basic equations that govern shocked flows as follows.

$$\frac{\partial \rho}{\partial t} + \nabla \cdot (\rho \mathbf{v}) = 0, \tag{3.1}$$

$$\frac{\partial}{\partial t}(\rho v_i) + \nabla_j (\rho v_i v^j + \delta_i^j p) = -\rho \nabla_i \phi, \tag{3.2}$$

$$\frac{\mathrm{d}\varepsilon}{\mathrm{d}t} + p \frac{\mathrm{d}}{\mathrm{d}t}\left(\frac{1}{\rho}\right) = q, \tag{3.3}$$

$$\frac{\partial}{\partial t}(nY_e) + \nabla \cdot (nY_e \mathbf{v}) = \lambda, \tag{3.4}$$

$$\Delta \phi = 4\pi G \rho, \tag{3.5}$$

as well as an equation of state (EoS). In the above expression, ρ, p, n, Y_e, ϵ and $\mathbf{v}$ are density, pressure, number density, electron fraction, specific internal energy and velocity, respectively. The gravitational potential ϕ is given by the Poisson equation (3.5) with G being the gravitational constant. We include the reactions between the electron-type neutrinos and fluid particles, which are symbolically denoted by q and λ: the former denotes the net heating rate and the latter is the net reaction rate of electrons and positrons. We use the light-bulb approximation with corrections by a geometric factor instead of solving the neutrino transport (Scheck et al., 2006). In this prescription, neutrino luminosities (L_{ν_e} and $L_{\bar{\nu}_e}$), neutrino temperatures (T_{ν_e} and $T_{\bar{\nu}_e}$) and neutrino spheres (r_{ν_e} and $r_{\bar{\nu}_e}$) are arbitrary parameters.

We employ an EoS that takes into account the contributions from nucleons, nuclei, photons, electron and positrons. The baryons are treated as ideal Boltzmann gases and we assume that the composition is obtained by the nuclear statistical equilibrium with 28 nuclei that includes p, n, D, T, ^{3}He, ^{4}He and 12 α particles as well as their neutron-rich isotopes, which are described in Yamamoto et al. (2013). Electron and positrons are treated as ideal Fermi gases with arbitrary degeneracy and relativistic parameters (Blinnikov et al., 1996). Photons are assumed to be ideal Bose gases.

Following Lai & Goldreich (2000) and the previous chapter, we linearize these equations by giving the perturbations as follows.

$$\delta X(\mathbf{r},t) = \delta X(r,t) Y_{lm}(\theta,\phi), \tag{3.6}$$

$$\begin{aligned}\delta\mathbf{v}(\mathbf{r},t) &= \delta v_r(r,t) Y_{lm}(\theta,\phi)\hat{\mathbf{r}} \\ &\quad + \delta v_\perp(r,t)\left[\hat{\theta}\frac{\partial Y_{lm}}{\partial\theta} + \frac{\hat{\phi}}{\sin\theta}\frac{\partial Y_{lm}}{\partial\phi}\right] + \delta v_{rot}(r,t)\left[-\hat{\phi}\frac{\partial Y_{lm}}{\partial\theta} + \frac{\hat{\theta}}{\sin\theta}\frac{\partial Y_{lm}}{\partial\phi}\right],\end{aligned} \tag{3.7}$$

where X denotes the scalar variables. $Y_{lm}(\theta,\phi)$ is the spherical harmonics of the indices l, m. $\hat{\mathbf{r}}, \hat{\theta}$, and $\hat{\phi}$ are unit vectors in spherical coordinates. Assuming that the background flow is spherically symmetric, the system of linearized equations is given symbolically as follows.[1]

$$M\frac{\partial\mathbf{y}}{\partial t} + P\frac{\partial\mathbf{y}}{\partial r} + Q\mathbf{y} = \mathbf{0}, \tag{3.8}$$

where $\mathbf{y} = \mathbf{y}(r,t)$ denotes the vector of perturbations that is given as

$$\mathbf{y}(r,t) = \left(\frac{\delta\rho}{\rho}, \frac{\delta v_r}{v_r}, \frac{\delta v_\perp}{v_r}, \frac{\delta T}{T}, \frac{\delta Y_e}{Y_e}, \frac{\delta v_{\rm rot}}{v_r}\right)^T, \tag{3.9}$$

and the coefficient matrices, $M = M(r)$, $P = P(r)$ and $Q = Q(r)$, whose components are made of the background quantities, are given in Appendix B.2.

We solve the linearized equations in the region between the standing shock and the surface of a proto-neutron star. The outer boundary condition imposed at the shock radius is given by the perturbed flows in front of the shock through the linearized Rankine-Hugoniot relations:

$$\mathbf{y}(r_{\rm sh},t) = \frac{\partial}{\partial t}\frac{\delta r_{\rm sh}}{r_{\rm sh}}\mathbf{c} + R\mathbf{z}^{(\rm up)}(r_{\rm sh},t), \tag{3.10}$$

[1] We assume that the perturbation of the gravitational potential is negligible. We believe that this assumption will not affect seriously the following results qualitatively nor quantitatively.

where δr_{sh} is the perturbed shock radius. R and $\mathbf{c}$ are some matrix and vector, whose components are described only by background quantities, and $\mathbf{z}^{(\mathrm{up})}$ denotes perturbed variables in front of the shock; The explicit forms are given in Appendix B.2.

The inner boundary is set at a proto-neutron star surface. We note here that we can impose only one condition, corresponding to a degree of freedom at the outer boundary, where the fluctuation of the shock radius remains as a free parameter once the upstream flow is given. Otherwise there is generally no solution that satisfies the inner and outer conditions at the same time. Hence the inner boundary condition is symbolically represented as

$$f(y_i(r_{\mathrm{PNS}}, t), t) = 0, \tag{3.11}$$

where y_i is some component of $\mathbf{y}$.

Summarizing the above setups, we solve the eigenvalue problem described by (3.8), (3.10) and (3.11) with the time-dependent shock radius, δr_{sh}, being the eigenvalue.

3.2.2 mode analysis

We solve this eigenvalue problem with the use of the Laplace transform with respect to time. Assuming that any perturbation does not exist initially ($t = 0$) in the shocked region because the seed of perturbations is supposed to be the upstream fluctuations that fall onto the standing shock, we obtain the Laplace transformed equations:

$$\frac{\mathrm{d}\mathbf{y}^*}{\mathrm{d}r} = -(sP^{-1}M + P^{-1}Q)\mathbf{y}^*, \tag{3.12}$$

$$\mathbf{y}^*(r_{\mathrm{sh}}, s) = s\frac{\delta r^*_{\mathrm{sh}}}{r_{\mathrm{sh}}}\mathbf{c} + R\mathbf{z}^*(r_{\mathrm{sh}}, s), \tag{3.13}$$

$$f^*(y_i^*(r_{\mathrm{PNS}}, s), s) = 0, \tag{3.14}$$

where the superscript, $*$, means Laplace-transformed functions. We here emphasize again that this is the system of ordinary differential equations with s being a parameter. We find the eigenvalue, δr^*_{sh}, such that both of the inner and outer boundary conditions are satisfied for each s. We note here that the eigenvalue is easily found by integrating (3.12) twice as discussed in Appendix B.1.

By solving the eigenvalue problem for a series of s and performing the inverse Laplace transform, we obtain the time evolution of the shock radius for given boundary conditions. The inverse transform should be performed by an integral along such

a path that is parallel to the imaginary axis and all singularities lie in the left of the line. If improper path is chosen, an incorrect time evolution is obtained. We note that singularities in the complex plane correspond to stable or unstable modes, which follows the fact:

$$\mathcal{L}[t^n \exp(s_0 t)] = \frac{n!}{(s - s_0)^{n+1}}, \tag{3.15}$$

where s_0 is a constant, whose real and imaginary parts correspond to the growth rate and frequency of the mode respectively. See also the left panel of Fig. 3.1. The poles can be found by observing the change of eigenvalues in the complex plane as shown in Fig. 3.2, where we gave an example of the behavior of eigenvalues near a pole.

Since the modes of SASI are not a priori known, a proper value for the real part of the integral path (x in Eq. (2.19)) is also not a priori known. In our research, an appropriate path is found by trying several integral paths, which keep a finite distance from each other. We illustrated the search paths in the right panel of Fig. 3.1. Empirically speaking, the resolution of $\Delta x = 10$ is sufficient not to miss the poles. Note that searching positive x is enough to identify unstable modes, which are more intriguing for the shock dynamics. Hence we start the search from the path near the imaginary axis ($x = x_0 \lesssim 0$) and then move to the path with $x_0 + n\Delta x$ ($n \in \mathbb{N}$).[2] If the path passes through a pole, i.e., there is a pole between n-th and $(n+1)$-th paths, then the residue of a pole is added to the integral on the $(n+1)$-th line.

In this way, we can at least reach an upper limit of the maximum growth rate since the time evolution of the shock radius is correctly obtained only for an appropriate integral path. With such a correct path, the shock radius remains stationary at $t < 0$, which follows from the initial condition, in which no perturbation exists in the shocked region. If some poles exist in thee right of the integral line (i.e., this is an inappropriate path), there remain residuals that should be included and as a result the shock moves even at $t < 0$, which violates our setting obviously.

3.2.3 models and parameters

We investigate realistic flows in CCSNe with the following two steady background models. One has a rather short distance between the shock and neutrino sphere, ~ 50 km, and the other has a larger shocked region where the distance is about 100 km.

[2]Here, we avoid the imaginary axis because the origin of the complex plane is a singular point in the sense that the eigenvalue is indeterminate, which follows from (3.13).

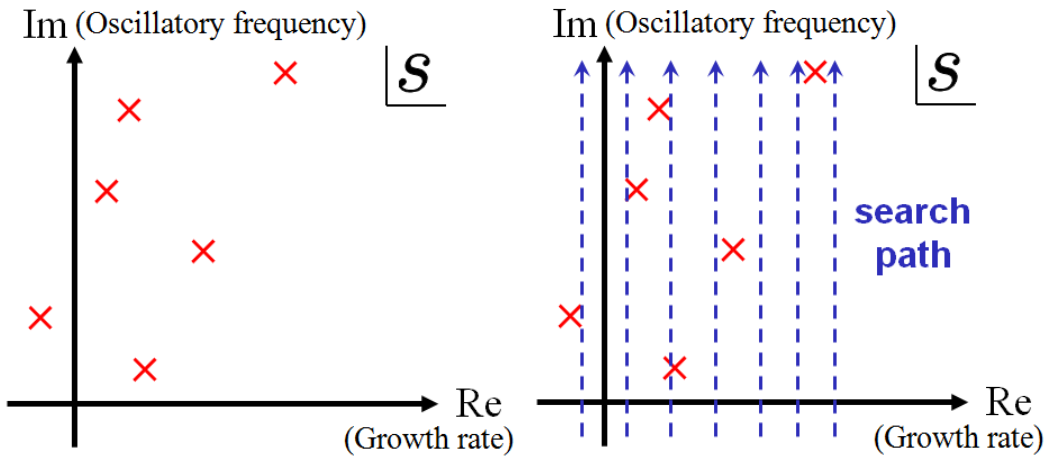

Figure 3.1: (Left) A schematic picture of the poles of the eigenvalue in the complex plane of s, which correspond to the stable/unstable modes of SASI. (Right) The chosen path to find the poles, which are also the same as the integral path for inverse transform. If there is no pole in the right hand side of the rightmost path, we see the convergence of the inverse transform for the path.

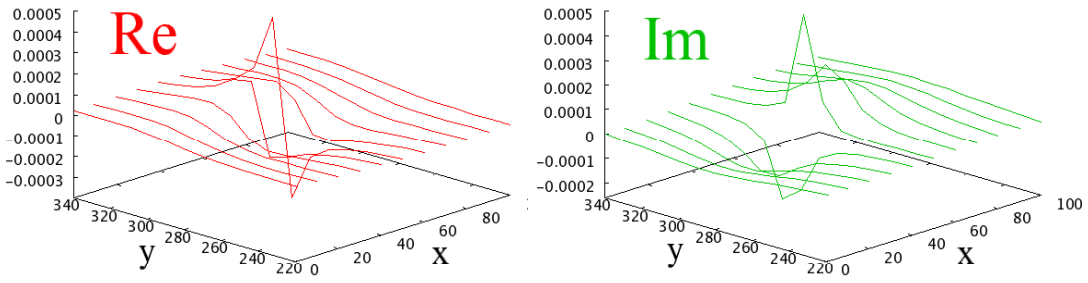

Figure 3.2: An example of the behavior of eigenvalues near a pole at (x, y) = (47.5, 288), where $x :=$ Re s and $y :=$ Im s. Left and right panel show the real and imaginary part of eigenvalues respectively. The resolutions are $\Delta x = 10$ and $\Delta y = 10$, which are sufficient to find poles in our models that are mentioned in the next section as shown in this figure.

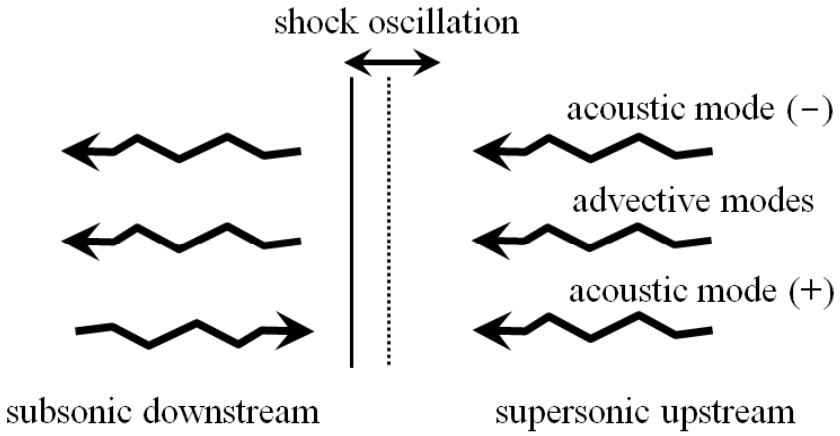

Figure 3.3: The schematic picture of the characteristics. The vertical lines represent shock radius and its oscillation. The right-hand side of the shock line corresponds to the upstream whereas the other side is the downstream. The zigzag arrows represent the waves, which also show the traveling direction. The top arrows correspond to the acoustic mode that propagates inward. Those in the bottom stand for the other acoustic mode that travels outward. Those in the middle line show the other advective modes.

The first one has the following parameter set: $\dot{M} = 1\ M_\odot$, $L_\nu = L_{\nu_e} = L_{\bar{\nu}_e} = 2 \times 10^{52}$ erg s^{-1}, $T_{\nu_e} = 5.33$ MeV, $T_{\bar{\nu}_e} = 6.33$ MeV, $r_{\nu_e} = 47.7$ km, $r_{\bar{\nu}_e} = 43.4$ km and $M_{sh} = 1.5\ M_\odot$ (the total mass in the shocked region). Here, the inner boundary is assumed to coincide with the neutrino sphere, r_{ν_e}, where the density is fixed to 10^{11} g cm^{-3}. For the quantities in upstream flows, we used those obtained from a supersonic Bondi accretion flow, which is given by the mass accretion rate and mass of the central region, a fixed ratio of specific heats, $\gamma := 1.36$, and density at the sonic point, which is set to 10^6 g cm^{-3}, in addition to a fixed nuclei, ^{56}Ni. Solving the steady spherically symmetric equations for the above parameter, we obtained the resultant shock radius of $r_{sh} \sim 99.8$ km, which gives the distance to the proto-neutron surface as about 52.2 km. This model has rather large mass accretion rate and small neutrino luminosities, which result in the short distance between the shock and the proto-neutron star. Since the distance defines the timescale of SASI provided the advective-acoustic or purely-acoustic cycle is responsible for the instability, the SASI activity is expected to be prominent in this model.

For the other model, we choose a set of parameters as $\dot{M} = 0.2\ M_\odot$, $L_\nu = L_{\nu_e} =$

$L_{\bar{\nu}_e} = 3 \times 10^{52}$ erg s^{-1}, $T_{\nu_e} = 13$ MeV, $T_{\bar{\nu}_e} = 15$ MeV, $r_{\nu_e} = 33$ km, $r_{\bar{\nu}_e} = 30$ km and $M_{sh} = 1.5\ M_\odot$. Other parameters that are necessary to obtain the steady state are the same as for the previous model. As a result, the resultant shock radius is ~ 129 km, which is apart from the proto-neutron star surface by 96.3 km. We note that this latter model resembles the numerical result of Marek & Janka (2009), where they simulated the collapse of a 15 $M_\odot$ progenitor (Woosley & Weaver, 1995) in 2D and obtained an explosion induced by SASI.

For these steady background flows, we apply the following perturbations at the shock surface. One is the delta-function type perturbation: $z_i^{(up)} \propto \delta(t)$ for any i-th component. This is a baseline model, where a seed of fluctuation is added to the shocked region only once initially ($t = 0$). Noting that no fluctuation is assumed in front of the shock at $t > 0$, we can interpret the results of this model as the intrinsic nature of SASI, where the upstream flow is spherically symmetric as assumed in the previous works.

On the other hand, we consider a simple toy model for the other case, where the perturbation changes sinusoidally in time: $z_i^{(up)} \propto \sin(\omega t)$, where ω is some constant frequency. Comparing the results with those of the baseline model, we can extract the effects of the perturbations in front of the shock.

Finally we mention the inner boundary condition. We employ the inner boundary condition that is given by

$$\mathbf{y} \cdot \mathbf{l}^{(\text{outgoing})} = 0 \quad \text{at} \quad r = r_{\nu_e} \quad \text{for} \quad {}^\forall t, \tag{3.16}$$

where $\mathbf{l}^{(\text{outgoing})}$ denotes the left eigenvector of the outgoing characteristic. This inner boundary condition hence means that there is no reflective wave at the proto-neutron star surface. Although this may appear to be artificial, it is a natural choice for the initial condition, where no fluctuation exists initially, as discussed below.

Recalling the degrees of freedom at the shock surface, we notice that there remain $n - 1$ degrees of freedom, where n denotes the number of the linearized equations, that are associated with the characteristics that emanate from the shock and another degree of freedom that corresponds to the shock oscillation (see also Fig. 3.3). We note here that the emanating characteristics exist only in the downstream because the upstream flow is supersonic and that there is an acoustic wave that comes into the shock in downstream due to the subsonic flow. Usually, all of the incoming waves are interpreted as imposed conditions whereas the outgoing waves and the oscillation amplitude of the shock are the resultant waves and motion respectively. Without the inner boundary condition that we impose at the proto-neutron star surface, the number of imposed conditions and the resultant degree of freedom match (both of

them are n).[3] This is not the case for our setup, however, due to the extra condition that is imposed at the inner boundary. Therefore, there is generally no resultant solution if we take all the incoming waves into the given conditions.

Nevertheless, we can solve the eigenvalue problem as a matter of fact. That is, we obtain the evolution of shock radius that satisfy the outer and inner boundary conditions at the same time unless they are too strange conditions. What happened? We found that the incoming wave in downstream violates the initial condition that there is no wave initially in the shocked region. In other words, we see the existence of the fluctuations in the shocked region even for $t < 0$. This outcome is quite natural, however, from another point of view: Since the degree of freedom related to the shock evolution is used to satisfy the inner boundary condition, one of the incoming waves is forced to turn out to be a 'resultant' wave. Recalling that the incoming waves in upstream are given as the outer boundary condition, the only possibility is the incoming acoustic mode. In other words, the outcome assumes such a evolution of the incoming acoustic wave that the shock evolution, which is determined by the outer and inner boundary conditions, and the evolution of the downstream, which is necessarily determined by the shock evolution due to the Rankine-Hugoniot relations, become consistent. This makes a contradiction, however, since we presumed that the shocked region is initially steady and the condition is included in the basic equation thanks to (2.13).

Hence we tried some inner boundary conditions to avoid such a contradictory outcome and the condition (3.16) is found to satisfy the initial condition consistently. This is the reason why we apply the inner boundary. We note, however, that although another condition that is given by $\delta v_r = 0$ for $^\forall t$, which is the same condition as in Yamasaki & Yamada (2007), violates the initial condition, the amplitude of the fluctuation that exists in $t < 0$ is much smaller than the perturbations that fall onto the shock surface.[4] Since it is negligible and hence thought to be approximately consistent, we also briefly mention the results that are obtained by applying this inner boundary condition in the following sections.

3.3 Analytical results

Before going to the results where the eigenvalue problem is solved numerically, we note that some important results for our setup are analytically deduced. Suppose

[3] Strictly speaking, the former statement holds because the shock wave in hydrodynamics is evolutionary. See also Chap. 4.

[4] It is 10^{-6} times as large as the infalling perturbations.

that $G(t)$ is the Green function for the eigenvalue problem: that is,

$$LG(t) = \delta(t), \tag{3.17}$$

where L is a linear operator and $G(t)$ describes the evolution of the shock radius, $\delta r_{sh}/r_{sh}$, for the impulsive input, $\mathbf{z}^{(up)} \propto \delta(t)$. Then, the evolution of the shock radius for an arbitrary input, $h(t)$, is given by

$$\frac{\delta r_{sh}}{r_{sh}} = \int_0^\infty G(t-\tau)h(\tau)\mathrm{d}\tau =: (G * h)(t), \tag{3.18}$$

where $(G * h)(t)$ denotes the convolution of G and h. Recalling that the Laplace transform of any convolution, $(f * g)(t)$, is the product of the Laplace transforms, $\mathcal{L}[f]\mathcal{L}[g]$ (e.g. Schiff, 1999), we obtain the following relation from (3.18):

$$\mathcal{L}\left[\frac{\delta r_{sh}}{r_{sh}}\right] = \mathcal{L}[G]\mathcal{L}[h]. \tag{3.19}$$

From this equation, the effects of the upstream input on the modes of SASI are discussed as follows. We note again that the left-hand side is the Laplace-transformed eigenvalue and the modes of SASI is emerged as poles of this function as stated in Sec. 3.2.2. On the other hand, $\mathcal{L}[G]$ is the Laplace-transformed solution of the baseline model and hence the poles of $\mathcal{L}[G]$ represent the modes of the intrinsic nature of SASI as mentioned in the previous section. And $\mathcal{L}[h]$ is a priori known since it is calculated once an input is given and, as a result, the poles of the function is also a priori obtained. Therefore, if the poles of $\mathcal{L}[G]$ are given, the modes of SASI under an upstream input $h(t)$ is immediately obtained by the right-hand side of (3.19).

If the poles of $\mathcal{L}[G]$ and $\mathcal{L}[h]$ overlap, then a resonant occurs, which follows from (3.15). Otherwise, the upstream perturbations do not change the unstable modes of SASI. That is, they do not change the growth rates nor frequencies.

3.4 Numerical results

Here, we show the results that are obtained by solving the eigenvalue problem (3.12)-(3.14) numerically. Since we discussed the effects of the fluctuations that fall onto the standing shock in the previous section, we focus here the intrinsic modes of SASI that are obtained by the impulsive input for our backgrounds.

We calculated the cases of $l = 1, 2$, which are the dominant modes of SASI. The integral region ranges $-40 \leq \mathrm{Re}\ s \leq \alpha$ and $-10240 \leq \mathrm{Im}\ s \leq 10240$, where α is an upper bound, which is known in the calculation as stated in Sec. 3.2.2.[5]

We listed up the peaks that we found for the inner boundary condition (3.16) in Table 3.1, 3.2, 3.3 and 3.4. In the tables, x and y denote the real and imaginary parts of the parameter, s, respectively, and represent the coordinate where the peak is found. τ and T are the corresponding growth timescale on the exponent and the period of oscillation respectively. We numbered the peaks in rank order of growth rates in the rightmost column. We also present here the characteristic timescales for the two models, t_1, t_2 and t_3, which are defined as the crossing time of the acoustic wave that travels to the central region, advection, and the other acoustic wave respectively: $t_1 = 1.622$ ms, $t_2 = 17.09$ ms, $t_3 = 2.286$ ms for the longer distance model and $t_1 = 2.811$ ms, $t_2 = 23.93$ ms, $t_3 = 4.031$ ms for the longer distance model.

We infer that there are infinite modes, which have shorter periods. Although the growth timescales of such modes become gradually smaller, we did not see such indications.

If we pick up the most dominant modes, which has smaller growth time scales, from the tables, the growth rate and periods are given as follows. For the shorter distance model, we see that $\tau = 11.7$ ms and $T = 3.15$ ms for $l = 1$ (the 7th peak) and $\tau = 8.66$ ms and $T = 2.76$ ms for $l = 2$ (the 8th peak) whereas we obtain that $\tau = 9.52$ ms and $T = 5.96$ ms for $l = 1$ (the 6th peak) and $\tau = 7.84$ ms and $T \sim 1.54$ ms for $l = 2$ (the 19th peak) for the other model.

Comparing the $l = 1, 2$ modes, we notice that the growth timescale of $l = 2$ is smaller than that of $l = 1$ and correspondingly the periods become shorter for both models, which indicates that the shorter timescale between each cycle results in the increase of cycles in a unit time and, as a result, SASI grows faster.

We see also some differences between the two models for the same l as follows. For the $l = 1$ mode, the period of the larger distance model is longer than that of the other, which is a natural result since the periods represent a crossing timescale. On the other hand, the growth timescale is smaller when the distance between the inner and outer boundaries is larger, which may indicate the model creates the acoustic wave that travels to shock surface more efficiently and it should be related to the background configurations. For the $l = 2$ mode, on the other hand, the period for the longer distance model becomes shorter, which is interpreted as the outgoing acoustic wave is produced at a different radius. In fact, this is possible since the

[5] As a matter of fact, we do not need to calculate the region with the negative imaginary part because the function before the Laplace transform is a real function and the property mentioned in the last part of Sec. 2.2.2 holds.

most dominant peak is changed from $l = 1$.

Comparing also the frequencies with the inverse of characteristic timescales, we realize that the dominant modes appears to be driven by the purely-acoustic cycles and the modes induced by the advective-acoustic cycles are sub-dominant in our models. We note that this is in sharp contrast to the previous analytical studies that support the advective-acoustic cycle (Yamasaki & Yamada, 2007; Foglizzo et al., 2007; Yamasaki & Foglizzo, 2008; Foglizzo, 2009; Sato et al., 2009; Guilet & Foglizzo, 2010, 2012). Moreover, the period of the $l = 2$ mode in the larger distance model seems to be shorter than the purely-acoustic timescale. We also note that the property that the purely-acoustic cycle seems to be dominant does not changes if we employ the other inner boundary condition.

We also realized that there is no convective modes, which are thought to grow exponentially without oscillations. In previous works, such modes are found in Yamasaki & Yamada (2007)

Finally we mention that there is no mode that oscillate without exponential growth or decay. Hence the upstream perturbations do not affect the stable nor unstable modes of SASI in these models as long as the fluctuation is represented by the sum of the sinusoidal functions without exponential growth.

3.5 Summary

We have studied the effects of non-spherical linear perturbations in upstream flows on SASI activity in CCSNe, which is reduced to an eigenvalue problem. It was solved with Laplace transform, which works well to identify the unstable modes as demonstrated in our analysis.

We investigated two different background flows, both of which employed a realistic EoS and model parameters. One model has a rather short distance between the shock and proto-neutron star surface whereas the other has a longer distance. We also employed two different inner boundary conditions.

As a result, we can concluded that upstream perturbations do not change stable nor unstable modes of SASI in general case. This is because the modes in SASI accompany with an exponential growth or decay. Hence the analogue to a spring under external forces does not holds and resonant motions never occur in SASI. This is, however, in contrast to the recent numerical results by Müller & Janka (2014); Couch & Ott (2013, 2014), who reported that the perturbations that are added in the outer regions of a progenitor lead to shock revival even for a model that fails to explode without them. This discrepancy may be interpreted as the importance of the non-linear effects of sufficiently amplified infalling perturbations as mentioned

in Müller & Janka (2014). Since our analysis can treat only the linear regime, we cannot mention the non-linear effect directly, however.

We also found that the dominant modes in our models seem to be driven by the purely-acoustic cycle for any model that we carried out. This is inferred from the fact that the oscillatory frequencies match the sound-crossing timescale. This result is opposite to those of previous linear analysis, which reported the dominant role of the advective-acoustic cycle (Yamasaki & Yamada, 2007; Foglizzo et al., 2007; Yamasaki & Foglizzo, 2008; Foglizzo, 2009; Sato et al., 2009; Guilet & Foglizzo, 2010, 2012). We also realized that convective modes are absent in our search although they are found for large neutrino luminosities in the previous studies. The latter may be the consequences of lower luminosities in our models. The former result needs obviously further investigations since we have only the information of timescales and could not make strong conclusions on the driving mechanism. For example, the radial distribution of the modes must be clarified to identify the driving cycle. Otherwise more systematic study for the background flow may help the interpretation.

Anyway, we feel that we need further studies to make more robust conclusions. Further investigations are going to be performed in the future

Table 3.1: The shorter distance model, $l = 1$

peak	x [sec^{-1}]	y [sec^{-1}]	τ [ms]	T [ms]	rank
1	0	0	0.00	0.00	29
2	47.5	288	21.05	21.82	10
3	-13.5	628	-74.07	10.01	32
4	-10.5	981	-95.24	6.40	31
5	-8.5	1331	-117.65	4.72	30
6	21.5	1685	46.51	3.73	27
7	85	1992	11.76	3.15	1
8	67	2243	14.93	2.80	2
9	22.5	2575	44.44	2.44	26
10	12.5	2928	80.00	2.15	28
11	25.5	3270	39.22	1.92	25
12	54.5	3596	18.35	1.75	4
13	63.5	3890	15.75	1.62	3
14	41	4205	24.39	1.49	17
15	30.5	4540	32.79	1.38	24
16	36.5	4878	27.40	1.29	23
17	50.5	5198	19.80	1.21	6
18	52.5	5510	19.05	1.14	5
19	42.5	5830	23.53	1.08	15
20	37.5	6160	26.67	1.02	22
21	42.5	6490	23.53	0.97	15
22	50	6810	20.00	0.92	7
23	47.5	7125	21.05	0.88	10
24	40.5	7450	24.69	0.84	18
25	39	7780	25.64	0.81	21
26	45	8105	22.22	0.78	13
27	49.5	8425	20.20	0.75	8
28	45.5	8742	21.98	0.72	12
29	39.5	9068	25.32	0.69	19
30	39.5	9338	25.32	0.67	19
31	45	9725	22.22	0.65	13
32	48.5	10045	20.62	0.63	9

Table 3.2: The shorter distance model, $l = 2$

peak	x [sec^{-1}]	y [sec^{-1}]	τ [ms]	T [ms]	rank
1	0	0	0.00	0.00	29
2	6.5	310	153.85	20.27	28
3	-12.5	651	-80.00	9.65	32
4	-8.5	1000	-117.65	6.28	31
5	-7.5	1348	-133.33	4.66	30
6	14.5	1700	68.97	3.70	27
7	73.5	2042	13.61	3.08	8
8	115.5	2279	8.66	2.76	1
9	48.5	2584	20.62	2.43	24
10	29.5	2936	33.90	2.14	26
11	36.5	3286	27.40	1.91	25
12	66.5	3622	15.04	1.73	15
13	91.5	3916	10.93	1.60	2
14	69.5	4218	14.39	1.49	11
15	52.5	4550	19.05	1.38	23
16	55.5	4890	18.02	1.28	22
17	71.5	5218	13.99	1.20	10
18	79.5	5528	12.58	1.14	3
19	68.5	5842	14.60	1.08	13
20	60.5	6172	16.53	1.02	21
21	65	6505	15.38	0.97	18
22	74.5	6825	13.42	0.92	6
23	74.5	7139	13.42	0.88	6
24	66.5	7461	15.04	0.84	15
25	62.5	7792	16.00	0.81	20
26	68.5	8121	14.60	0.77	13
27	75.5	8441	13.25	0.74	4
28	73.5	8757	13.61	0.72	8
29	65.5	9080	15.27	0.69	17
30	63.5	9410	15.75	0.67	19
31	69.5	9739	14.39	0.65	11
32	75.5	10058	13.25	0.62	4

Table 3.3: The longer distance model, $l = 1$

peak	x [sec^{-1}]	y [sec^{-1}]	τ [ms]	T [ms]	rank
1	0	0	0.00	0.00	46
2	2.5	200	400.00	31.42	45
3	44.5	457	22.47	13.75	33
4	44.5	750	22.47	8.38	33
5	5.5	1000	181.82	6.28	44
6	103	1058	9.71	5.94	1
7	46.5	1315	21.51	4.78	31
8	39.5	1590	25.32	3.95	41
9	52.5	1855	19.05	3.39	28
10	93.5	2039	10.70	3.08	3
11	42.5	2225	23.53	2.82	37
12	27.5	2475	36.36	2.54	43
13	43.5	2730	22.99	2.30	36
14	94.5	2950	10.58	2.13	2
15	66	3125	15.15	2.01	18
16	34.5	3370	28.99	1.86	42
17	40.5	3625	24.69	1.73	40
18	84.5	3855	11.83	1.63	9
19	79.5	4025	12.58	1.56	11
20	41.5	4265	24.10	1.47	39
21	42.5	4518	23.53	1.39	37
22	77.5	4755	12.90	1.32	12
23	86.5	4930	11.56	1.27	7
24	48.5	5158	20.62	1.22	30
25	44.5	5408	22.47	1.16	33
26	70.5	5650	14.18	1.11	15
27	91.5	5838	10.93	1.08	4
28	56.5	6053	17.70	1.04	25
29	46.5	6300	21.51	1.00	31
30	66.5	6545	15.04	0.96	17
31	91.5	6742	10.93	0.93	4
32	62.5	6950	16.00	0.90	20
33	49.5	7195	20.20	0.87	29
34	63.5	7438	15.75	0.84	19
35	89.5	7645	11.17	0.82	6
36	69.5	7848	14.39	0.80	16
37	53.5	8088	18.69	0.78	27
38	62.5	8330	16.00	0.75	20
39	85.5	8545	11.70	0.74	8
40	74.5	8748	13.42	0.72	14
41	56.5	8981	17.70	0.70	25
42	61.5	9222	16.26	0.68	22
43	82.5	9445	12.12	0.67	10
44	77.5	9648	12.90	0.65	12
45	59.5	9875	16.81	0.64	24
46	61.5	10118	16.26	0.62	22

Table 3.4: The longer distance model, $l = 2$

peak	x [sec^{-1}]	y [sec^{-1}]	τ [ms]	T [ms]	rank
1	0	0	0.00	0.00	44
2	-34	240	-29.41	26.18	46
3	21.5	475	46.51	13.23	42
4	21.5	761	46.51	8.26	42
5	-15	997	-66.67	6.30	45
6	110.5	1170	9.05	5.37	11
7	86.5	1319	11.56	4.76	20
8	49.5	1600	20.20	3.93	38
9	43.5	1865	22.99	3.37	41
10	83.5	2110	11.98	2.98	25
11	100.5	2240	9.95	2.80	14
12	49.5	2480	20.20	2.53	38
13	49.5	2740	20.20	2.29	38
14	84.5	2995	11.83	2.10	23
15	121	3160	8.26	1.99	4
16	62.5	3375	16.00	1.86	35
17	53.5	3632	18.69	1.73	37
18	81.5	3885	12.27	1.62	28
19	127.5	4069	7.84	1.54	1
20	75.5	4270	13.25	1.47	32
21	60.5	4524	16.53	1.39	36
22	81.5	4778	12.27	1.32	28
23	126.5	4972	7.91	1.26	2
24	86.5	5166	11.56	1.22	20
25	66.5	5419	15.04	1.16	34
26	81.5	5667	12.27	1.11	28
27	124.5	5880	8.03	1.07	3
28	96.5	6065	10.36	1.04	15
29	72.5	6310	13.79	1.00	33
30	82.5	6560	12.12	0.96	27
31	120.5	6780	8.30	0.93	5
32	104.5	6965	9.57	0.90	13
33	78.5	7205	12.74	0.87	31
34	83.5	7452	11.98	0.84	25
35	115.5	7680	8.66	0.82	8
36	112	7865	8.93	0.80	10
37	84.5	8100	11.83	0.78	23
38	85.5	8345	11.70	0.75	22
39	112.5	8578	8.89	0.73	9
40	116.5	8768	8.58	0.72	7
41	90.5	8992	11.05	0.70	17
42	87.5	9240	11.43	0.68	19
43	109.5	9475	9.13	0.66	12
44	118.5	9670	8.44	0.65	6
45	95.5	9890	10.47	0.64	16
46	90.5	10130	11.05	0.62	17

Chapter 4

Exact MHD Riemann Solver

4.1 Introduction

The Riemann problem is a kind of initial value problems for hyperbolic systems such as the system of equations of ideal hydrodynamics or ideal MHD, in which the initial condition is given by two constant states separated by a discontinuity. Not only do the solutions of Riemann problems have mathematical interest, but also solving Riemann problems is one of the main tasks in numerical schemes for fluid dynamics because the solutions are used to obtain numerical fluxes. Although the theory of partial differential equations underlies that of Riemann problems, solving Riemann problems in one-dimensional space turns to be equivalent to solving the algebraic equations and hence the solution is obtained by the Newton-Raphson method in principle. This facilitation does not necessarily mean that Riemann problems can be easily solved, however. In ideal MHD, for example, the system of algebraic equations is highly non-linear and complex in addition to the five-dimension parameter space, which reflect the non-linearity and largeness of the original system of partial differential equations.

Moreover, there exists an outstanding problem in MHD Riemann problems that there is no convincing criterion for physically relevant solutions. It is well-known that the solution of Riemann problems is generally not unique in the sense of the weak solution and some conditions should be imposed to single out the physically relevant one (Jeffrey & Taniuti, 1964). A famous and obviously acceptable condition is the so-called entropy condition, which admits only the shocks across which the entropy increases. The entropy condition discards manifestly unphysical solutions such as those including expanding shocks, across which the entropy is decreased, and the condition works well indeed in ordinary hydrodynamics to uniquely choose a solution.

In ideal MHD, however, the entropy condition is insufficient to uniquely choose a solution. In fact, some initial conditions have more than one solutions that satisfy the entropy condition (Torrilhon, 2002, 2003b,a). Therefore the so-called evolutionary conditions are introduced, which require that physically relevant shocks should be structurally stable. We must note here that the structural stability is totally different from the more familiar stability that discusses the exponentially growth. Structurally stable shocks just remain close to the initial discontinuity when they are perturbed, while structurally unstable ones will instantaneously split into other waves (Landau et al., 1984). The evolutionary conditions discard the so-called intermediate shocks, across which the transverse magnetic field is reversed (the definition and detailed classification of the shocks are given in Sec. 4.3), and the uniqueness of the solution seems to be recovered. Indeed, the intermediate shocks had been considered to be unphysical in the literatures (e.g. Jeffrey & Taniuti, 1964; Kantrowitz & Petschek, 1966).

However, the relevance of the intermediate shocks is still under debate. In fact, the intermediate shocks are commonly observed as stable shocks in numerical simulations in spite of the evolutionary conditions (Wu, 1987, 1988b,a, 1990; Brio & Wu, 1988; Wu & Kennel, 1992). The evolutionary conditions are also reconsidered in the context of dissipative MHD (Hada, 1994; Markovskii, 1998; Inoue & Inutsuka, 2007). They found that the new modes that do not exist in ideal MHD are responsible for the evolutionary conditions and the intermediate shocks become evolutionary in the dissipative system. We also note that some interplanetary experiments have reported the detection of the intermediate shocks (Chao, 1995; Feng & Wang, 2008; Feng et al., 2009). These results cast doubt on the classical theory of MHD and support the relevance of the intermediate shocks. On the other hand, there also exist completely opposite arguments, defending the classical theory. Falle & Komissarov (1997, 2001) pointed out that the intermediate shocks are observed in numerical simulations only because the initial conditions have a special symmetry, where the initial transverse magnetic fields and velocities are confined in a plane. Since there is no reason to break the symmetry, Alfvén waves, which rotate the fields, do not emerge and the absence of the waves affects the evolutionary conditions. In fact, some authors demonstrated numerically that some intermediate shocks break into other waves once the symmetry is broken by adding another component of the field (Barmin et al., 1996; Falle & Komissarov, 1997, 2001). Although Falle & Komissarov (2001) agreed with Wu (1990) that the temporary survival of some intermediate shocks in their interaction with Alfvén waves is due to non-unique dissipative structures, they claimed that the shocks should be regarded as transients. Kulikovskii et al. (2001) also came to the same conclusion.

Since the intermediate shocks are poorly understood, it is desirable for MHD Riemann solvers to treat these shocks as well as ordinary shocks. This is the reason why we will present a Riemann solver that can handle all types of the intermediate shocks. Furthermore, our solver can also treat the switch-on/off shocks and switch-on/off rarefactions (see Sec. 4.3 for the details of these waves), which are required because there are some initial conditions that have only a solution in which these non-regular shocks and switch-off rarefactions exist and do not have any other solutions without them as displayed in this chapter. Our solver can handle any initial condition: It does not matter whether a normal or transverse magnetic field is absent. Although Andreev et al. (2008) released an exact MHD Riemann solver online, their solver does not consider either of these waves and requires the initial conditions where both the normal and transverse magnetic field exist. We also note that Torrilhon (2002) proposed an idea of treating the intermediate shocks although they neglected some types. While our solver is partly based on the idea of Torrilhon (2002), we extensively modified it to handle all types of intermediate shocks. Furthermore, details of the main techniques are presented for the first time since Torrilhon (2002) did not show the details of their method, which must be rather complicated as described in Sec. 4.4 to Sec. 4.6.

Our solver has potential to solve an outstanding problem associated with the uniqueness and existence of the solution of MHD Riemann problems. In fact, even the local existence and uniqueness are no longer guaranteed by the Lax's theorem (Lax, 1957; Jeffrey & Taniuti, 1964; Serre, 1999) because the system of ideal MHD is not strictly hyperbolic and the characteristic fields are neither linear nor genuinely non-linear (Falle & Komissarov, 2001). It is worth mentioning that there are some analytical studies on the existence and uniqueness of solutions of ideal MHD Riemann problems: Gogosov (1961, 1962) investigated the wave-pattern of solutions in MHD Riemann problems, considering only the evolutionary waves and switch-off waves. Taking the intermediate shocks into account, Torrilhon (2003b) investigated the uniqueness of the solution although they assumed that a particular type of intermediate shock emerges on only one side. On the other hand, our solver can find all the solutions for a given Riemann problem and hence it is possible to study the structure of the solution space without any restriction. Therefore the solver is a powerful instrument to examine the non-uniqueness and existence of solutions. The solver may also be applicable to numerical MHD, where the Riemann solver provides numerical fluxes. Actually, there are several works on numerical MHD codes with Riemann solvers (e.g. Dai & Woodward, 1994; Sano et al., 1999; Iwasaki & Inutsuka, 2011). Moreover, using the exact solutions, our solver enables one to investigate which solutions are produced by a given approximate MHD Riemann solver, which

has never been studied. It will give one of the essential criteria for appropriate schemes if the physically relevant conditions for Riemann solutions are revealed in the future.

This chapter is organized as follows. At first, we review the theory of Riemann problems in the next section. In Sec. 4.3, we give a brief review of the shock waves and simple waves in ideal MHD, which are constituents of the solution of the Riemann problems. In Secs. 4.4 and 4.5, the main procedure to solve the Riemann problems is given. Other technical details are given in Sec. 4.6. In Sec. 4.7, we demonstrate the capability of our solver by showing the solutions of some MHD Riemann problems. We summarize the features of our solver in Sec. 4.9.

4.2 Theory of Riemann problems

4.2.1 hyperbolic equations and weak solutions

In this section we consider general conservation equations in one spatial dimension. This is sufficient since Riemann problems assume plane-symmetry. Then the coupled equations are expressed as

$$\frac{\partial \boldsymbol{u}}{\partial t} + \frac{\partial \boldsymbol{f}}{\partial x} = \boldsymbol{0}, \tag{4.1}$$

where $\boldsymbol{u}$ is a vector of conserved variables and $\boldsymbol{f}(\boldsymbol{u})$ is a flux vector. The system (4.1) is called hyperbolic if the Jacobian matrix, which is defined as

$$A_{ij} := \frac{\partial f_i}{\partial u_j}, \tag{4.2}$$

has N real eigenvalues $\lambda_k(\boldsymbol{u})$ $(k = 1, 2, \ldots, N)$ and corresponding N linealy independent right eigenvectors, $\boldsymbol{r}_k(\boldsymbol{u})$ (e.g. Falle & Komissarov, 2001). In particular, the system is called strictly hyperbolic if all eigenvalues are different from each other for any $\boldsymbol{u}$.

The k-th characteristic field is called genuinely non-linear if the following condition is satisfied for any $\boldsymbol{u}$:

$$\boldsymbol{r}_k \cdot \boldsymbol{\nabla}_{\boldsymbol{u}} \lambda_k \neq 0. \tag{4.3}$$

Here $\boldsymbol{\nabla}_{\boldsymbol{u}}$ denotes the operator, ${}^t(\partial/\partial u_1, \ldots, \partial/\partial u_N)$, where ${}^t(\ldots)$ stands for transposition. On the other hand, The k-th characteristic field is called linear if

$$\boldsymbol{r}_k \cdot \boldsymbol{\nabla}_{\boldsymbol{u}} \lambda_k = 0 \tag{4.4}$$

for all $\boldsymbol{u}$. Note that the characteristic field may be neither linear nor genuinely non-linear.

In the system described by Eq. (4.1), discontinuities are ubiquitous. Indeed they may be spontaneously produced from a continuous initial condition by wave-steepening. Since Eq. (4.1) is differential equations, these discontinuities cannot be treated as they are and some extensions are needed. The weak solutions of Eq. (4.1) are defined as the functions that satisfy the following equations instead of Eq. (4.1) in a finite domain $D(x,t)$ (e.g. Jeffrey & Taniuti, 1964):

$$\int_{-\infty}^{\infty} \boldsymbol{w}(x,0)\cdot\boldsymbol{\phi}(x)\mathrm{d}x + \int_{0}^{\infty}\mathrm{d}t\int_{-\infty}^{\infty}\mathrm{d}x\left(\frac{\partial \boldsymbol{w}}{\partial t}\cdot\boldsymbol{u}+\frac{\partial \boldsymbol{w}}{\partial x}\cdot\boldsymbol{f}\right)=0, \tag{4.5}$$

where $\boldsymbol{\phi}(x)$ is an initial condition and $\boldsymbol{w}(x,t)$ is a vector of test functions, which are differentiable with respect to x and t as many times as is required and are identically zero outside $D(x,t)$. This equation is derived by multiplying the original equations by $\boldsymbol{w}$ and integrating the product by parts. Note that the differentiability of weak solutions is not required. If the solution is differentiable and satisfies Eq. (4.1), then Eq. (4.5) is also satisfied. Hence ordinary solutions are indeed weak solutions. It should be remarked that the uniqueness of weak solution for a given initial condition is no longer guaranteed.

4.2.2 waves in the solutions of Riemann problems

The Riemann problem is an initial value problem for a system of conservation equations, in which two constant states are separated initially by a discontinuity, which is located, e.g., at $x=0$:

$$\boldsymbol{u}(x,0)=\begin{cases}\boldsymbol{u}_{\mathrm{R}} & (x>0)\\ \boldsymbol{u}_{\mathrm{L}} & (x<0).\end{cases} \tag{4.6}$$

We seek weak solutions to this problem. As remarked at the end of the previous section, the weak solutions are not unique in general and it is one of the important issues of Riemann problems to determine which solution is physically meaningful. Since there is no typical time and length scales in the problem, the solution should be self-similar. It is well known that solutions of Riemann problems consist of a couple of centered simple waves and discontinuities. The latter satisfies the Rankine-Hugoniot relations (e.g. Jeffrey & Taniuti, 1964).

The simple waves are defined as waves, in which there is only one independent component in $\boldsymbol{u}$ and all the other components are its functions. They are related

with the eigenvalues of the Jacobian matrix (4.2) in such a way that all quantities in the simple wave are constant along each characteristic given by

$$x = \lambda_k t + \text{constant}. \tag{4.7}$$

The simple wave that corresponds to eigenvalue λ_k is referred to as the k-th simple wave.

Associated with the k-th simple wave are so-called the k-th Riemann invariants denoted by $J_l^k (l = 1, 2, \ldots, N-1)$, which are constant across the k-th simple wave. They are defined to be the quantities that satisfy the following relation with the k-th right eigenvector, $\boldsymbol{r}_k$:

$$\boldsymbol{r}_k \cdot \boldsymbol{\nabla}_{\boldsymbol{u}} J_l^k = 0. \tag{4.8}$$

The k-th Riemann invariants define $N-1$ hypersurfaces in phase space and their intersection is a line, to which the k-th right eigenvector, $\boldsymbol{r}_k$, is tangential, and is called the locus of the k-th simple wave. See a schematic picture drawn in Fig. 4.1.

The Rankine-Hugoniot relations, which are satisfied by the quantities on both sides of a discontinuity, are expressed as

$$s[\![\boldsymbol{u}]\!] - [\![\boldsymbol{f}]\!] = \boldsymbol{0}, \tag{4.9}$$

where s is the velocity of the discontinuity and $[\![X]\!] := X_1 - X_0$ denotes a jump in quantity X across the discontinuity and X_0 and X_1 are the values ahead of and behind the discontinuity respectively. Since this is a system of N equations, we obtain a one-parameter family of solutions for a state given on one side of the discontinuity. Not all solutions are physical as mentioned repeatedly: Rarefaction shock waves for hydrodynamical equations are well known examples. Since entropy decreases across such shock waves, they are certainly unphysical and rejected. This entropy condition is not sufficient to eliminate all unphysical solutions in general and the so-called evolutionary conditions are introduced.

4.2.3 evolutionary conditions

Intuitively put, the evolutionary conditions require that physical solutions should be stable against splitting into other waves (see e.g. Falle & Komissarov, 2001; Polovin & Demutskii, 1990; Landau et al., 1984; Jeffrey & Taniuti, 1964; Lax, 1957). T
be more precise, when a small-amplitude wave is injected to the discontinuity, the resultant state, which should be determined uniquely, is required to still consist of
l-amplitude waves. This is satisfied

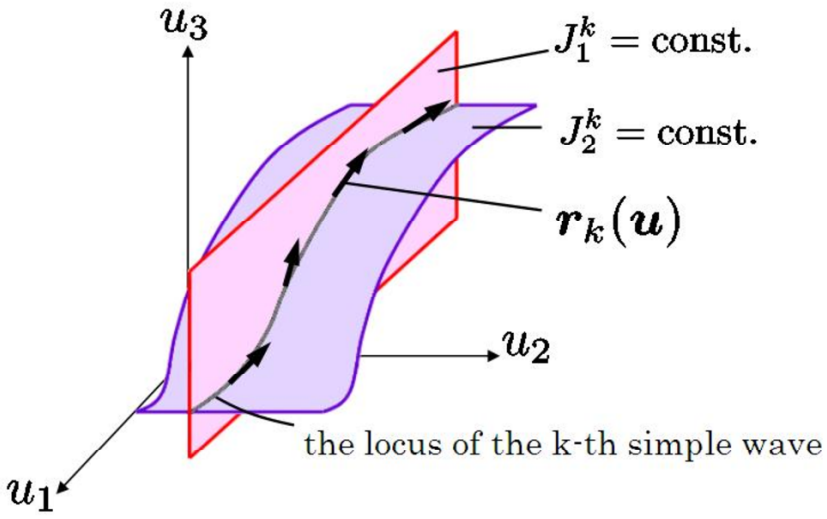

Figure 4.1: A schematic picture of the k-th Riemann invariants and corresponding locus of the k-th simple wave in the case of $N = 3$. There are two k-th Riemann invariants: J_1^k and J_2^k. The red surface is defined by $J_1^k = \text{const.}$ and the blue one is given by $J_2^k = \text{const.}$ The intersection is a line called the locus of the k-th simple wave, to which the k-th right eigenvector, $r_k(\boldsymbol{u})$, is tangential.

if the number of characteristics emanating from the discontinuity is $N+1$ and if the initial jump, $[\![\boldsymbol{u}]\!]$, is linearly independent of the eigenvectors that correspond to the outgoing characteristics.

4.3 Ideal MHD

In plane symmetry, the ideal MHD equations are given by

$$\frac{\partial \rho}{\partial t} + \frac{\partial}{\partial x}(\rho v_n) = 0, \tag{4.10}$$

$$\frac{\partial}{\partial t}(\rho v_n) + \frac{\partial}{\partial x}\left(\rho v_n^2 + p + \frac{\boldsymbol{B}_t^2}{2}\right) = 0, \tag{4.11}$$

$$\frac{\partial}{\partial t}(\rho \boldsymbol{v}_t) + \frac{\partial}{\partial x}(\rho v_n \boldsymbol{v}_t - B_n \boldsymbol{B}_t) = \boldsymbol{0}, \tag{4.12}$$

$$\frac{\partial \boldsymbol{B}_t}{\partial t} + \frac{\partial}{\partial x}(v_n \boldsymbol{B}_t - B_n \boldsymbol{v}_t) = \boldsymbol{0}, \tag{4.13}$$

$$\frac{\partial e}{\partial t} + \frac{\partial}{\partial x}\left[\left(e + p + \frac{\boldsymbol{B}^2}{2}\right) v_n - B_n \boldsymbol{B}\cdot\boldsymbol{v}\right] = 0, \tag{4.14}$$

where ρ, p, $\boldsymbol{v}$ and $\boldsymbol{B}$ are density, pressure, flow velocity and magnetic field respectively (Landau et al., 1984). The subscripts n and t indicate the normal component, i.e. x-component, and transverse component, i.e. y or z-component respectively. The total energy density is denoted by $e = p/(\gamma-1) + \rho\boldsymbol{v}^2/2 + \boldsymbol{B}^2/2$, where the equation of state for ideal gas is assumed and γ is the ratio of specific heats. The normal component of magnetic field, B_n, is constant owing to the divergence-free condition.

4.3.1 simple waves

The eigenvalues of the Jacobian matrix for the system of Eqs. (4.10)-(4.14) are

$$v_n \mp c_f, \quad v_n \mp c_A, \quad v_n \mp c_s, \quad v_n, \tag{4.15}$$

where c_f, c_A and c_s are called the fast, Alfvén and slow speeds respectively. They are expressed as

$$c_{f,s} := \left[\frac{1}{2}\left(\frac{\boldsymbol{B}^2}{\rho} + a^2\right) \pm \sqrt{\frac{1}{4}\left(\frac{\boldsymbol{B}^2}{\rho} + a^2\right)^2 - a^2\frac{B_n^2}{\rho}}\right]^{1/2}, \tag{4.16}$$

$$c_A := \sqrt{\frac{B_n^2}{\rho}}. \tag{4.17}$$

In the above expressions, $a = \sqrt{\gamma p/\rho}$ is the acoustic speed. In Eq. (4.15), the minus (plus) sign is applied to the left-going (right-going) waves. The simple waves corresponding to these eigenvalues are referred to as the fast, Alfvén, slow and entropy

waves respectively. The right eigenvectors for fast and slow waves are given as

$$\boldsymbol{r}_{f,s}^{\mp} = \xi_{f,s} \begin{bmatrix} -\rho \\ -\gamma p \\ \pm c_{f,s} \\ \pm \dfrac{c_{f,s}}{1-(c_{f,s}/c_A)^2} \dfrac{\boldsymbol{B}_t}{B_n} \\ \dfrac{\boldsymbol{B}_t}{(c_A/c_{f,s})^2 - 1} \end{bmatrix}, \tag{4.18}$$

in which the new variables, ξ_f and ξ_s, are introduced as follows:

$$\xi_f := \sqrt{\frac{a^2 - c_s^2}{c_f^2 - c_s^2}}, \quad \xi_s := \sqrt{\frac{c_f^2 - a^2}{c_f^2 - c_s^2}}. \tag{4.19}$$

These factors are necessary to ensure that the eigenvectors do not vanish for any $\boldsymbol{u}$. In deriving the above expressions of right eigenvectors we assume that $\boldsymbol{u} = (\rho, p, v_n, \boldsymbol{v}_t, \boldsymbol{B}_t)$. Since we do not use the right eigenvectors for the Alfvén and entropy waves in solving MHD Riemann problems, we do not give their explicit forms here. Note that the Alfvén and entropy waves are linear whereas the fast and slow waves are neither linear nor genuinely non-linear.

The eigenvalues are degenerate in the following two cases:

$$B_n = 0 \quad : \qquad c_f = \sqrt{a^2 + \frac{\boldsymbol{B}_t^2}{\rho}}, \quad c_s = c_A = 0, \tag{4.20}$$

$$B_n \neq 0, \ \boldsymbol{B}_t = \boldsymbol{0} \quad : \qquad c_f = \max(a, c_A), \quad c_s = \min(a, c_A). \tag{4.21}$$

In the latter case the limits of the right eigenvectors for fast and slow waves as $\boldsymbol{B}_t \to \boldsymbol{0}$ depend on the magnitudes of the acoustic and Alfvén speeds. For $a > c_A$ we obtain

$$\boldsymbol{r}_f^{\mp} \to \begin{bmatrix} -\rho \\ -\gamma p \\ \pm a \\ \boldsymbol{0} \\ \boldsymbol{0} \end{bmatrix}, \quad \boldsymbol{r}_s^{\mp} \to a \begin{bmatrix} 0 \\ 0 \\ 0 \\ \pm \mathrm{sgn}(B_n)\, \boldsymbol{e}_t \\ \sqrt{\rho}\, \boldsymbol{e}_t \end{bmatrix}, \tag{4.22}$$

where $\boldsymbol{e}_t$ is a unit vector that has the same direction as the transverse magnetic field. Note that $\boldsymbol{r}_f^{\mp}$ is reduced to the eigenvectors for the rarefaction waves in the ordinary

hydrodynamics. In the opposite case, i.e. $a < c_A$, we get

$$\boldsymbol{r}_f^{\mp} \to a \begin{bmatrix} 0 \\ 0 \\ 0 \\ \mp \mathrm{sgn}(B_n)\boldsymbol{e}_t \\ -\sqrt{\rho}\boldsymbol{e}_t \end{bmatrix}, \quad \boldsymbol{r}_s^{\mp} \to \begin{bmatrix} -\rho \\ -\gamma p \\ \pm a \\ \mathbf{0} \\ \mathbf{0} \end{bmatrix}, \tag{4.23}$$

in which $\boldsymbol{r}_s^{\mp}$ is reduced to the eigenvectors for the ordinary rarefaction waves in hydrodynamics. Finally in the case of $a = c_A$, we find

$$\boldsymbol{r}_f^{\mp} \to \frac{1}{\sqrt{2}} \begin{bmatrix} -\rho \\ -\gamma p \\ \pm a \\ \mp a\boldsymbol{e}_t \\ -a\sqrt{\rho}\boldsymbol{e}_t \end{bmatrix}, \quad \boldsymbol{r}_s^{\mp} \to \frac{1}{\sqrt{2}} \begin{bmatrix} -\rho \\ -\gamma p \\ \pm a \\ \pm a\boldsymbol{e}_t \\ a\sqrt{\rho}\boldsymbol{e}_t \end{bmatrix}. \tag{4.24}$$

As mentioned earlier, the right eigenvectors are chosen in our code so that these degenerate cases could be properly handled as the limits of non-degenerate cases.

In the fast rarefaction wave the magnitude of transverse magnetic field is decreased and, as a limiting case, it vanishes behind the so-called switch-off rarefaction wave. Since the fast rarefaction wave cannot reverse the direction of the transverse magnetic field, the switch-off rarefaction is the end point of the fast rarefaction locus.

4.3.2 discontinuities

As mentioned earlier, discontinuities are another important element in the solutions of Riemann problem. The quantities on both sides of a discontinuity satisfy the Rankine-Hugoniot relations, which in ideal MHD are expressed as

$$m = \text{const.}, \tag{4.25}$$

$$m^2[\![v]\!] + \left[\!\!\left[p + \frac{\boldsymbol{B}_t^2}{2} \right]\!\!\right] = 0, \tag{4.26}$$

$$m[\![\boldsymbol{v}_t]\!] - B_n[\![\boldsymbol{B}_t]\!] = \mathbf{0}, \tag{4.27}$$

$$m[\![v\boldsymbol{B}_t]\!] - B_n[\![\boldsymbol{v}_t]\!] = \mathbf{0}, \tag{4.28}$$

$$m\left(\left[\!\!\left[\frac{pv}{\gamma - 1} \right]\!\!\right] + \langle p \rangle [\![v]\!] + \frac{1}{4}[\![v]\!][\![\boldsymbol{B}_t]\!]^2 \right) = 0, \tag{4.29}$$

in the rest frame of the discontinuity. In the above expressions, $m := \rho_0 v_{n0} = \rho_1 v_{n1}$ is the mass flux, $v := 1/\rho$ is the specific volume and $\langle X \rangle := (X_0 + X_1)/2$ stands

for the arithmetic mean of upstream and downstream quantities. The solutions can be classified into the fast, slow or intermediate shock or into the rotational, contact or tangential discontinuity. Details of the classification are found in the literature (e.g. Jeffrey & Taniuti, 1964; Polovin & Demutskii, 1990; Torrilhon, 2002, 2003b). In what follows, we summarize only those features that are needed for later discussions.

Following Torrilhon (2002, 2003b), we normalize all quantities with those upstream as

$$\hat{v} := \frac{v_1}{v_0}, \quad \hat{p} := \frac{p_1}{p_0}, \quad \hat{\boldsymbol{B}}_t := \frac{\boldsymbol{B}_{t1}}{\sqrt{p_0}}, \tag{4.30}$$

$$\boldsymbol{A} := \frac{\boldsymbol{B}_{t0}}{\sqrt{p_0}}, \quad B := \frac{B_n}{\sqrt{p_0}}, \quad M_0 := \frac{v_{n0}}{a_0}, \tag{4.31}$$

and employ in the following the dimensionless MHD Rankine-Hugoniot relations, which are obtained by substituting Eqs. (4.30)-(4.31) and eliminating $[\![\boldsymbol{v}_t]\!]$ in Eqs. (4.25)-(4.29):

$$\hat{p} - 1 + \gamma M_0^2(\hat{v} - 1) + \frac{1}{2}(\hat{\boldsymbol{B}}_t^{\,2} - \boldsymbol{A}^2) = 0, \tag{4.32}$$

$$\gamma M_0^2(\hat{v}\hat{\boldsymbol{B}}_t - \boldsymbol{A}) - B^2(\hat{\boldsymbol{B}}_t - \boldsymbol{A}) = 0, \tag{4.33}$$

$$M_0\left[\frac{1}{\gamma - 1}(\hat{p}\hat{v} - 1) + \frac{1}{2}(\hat{v} - 1)(\hat{p} + 1) + \frac{1}{4}(\hat{v} - 1)(\hat{\boldsymbol{B}}_t - \boldsymbol{A})^2\right] = 0. \tag{4.34}$$

Fixing the upstream quantities, A, B and M_0, we solve Eqs. (4.32)-(4.34) and use Eqs. (4.30)-(4.31) to obtain v_1, p_1 and $\boldsymbol{B}_{t1}$. The other downstream quantities can be calculated as

$$v_{n1} = \hat{v} v_{n0}, \tag{4.35}$$

$$\boldsymbol{v}_{t1} = \boldsymbol{v}_{t0} \pm \frac{a_0 B}{\gamma M_0}[\![\hat{\boldsymbol{B}}_t]\!]. \tag{4.36}$$

In Eq. (4.36), the plus and minus signs correspond to the left- and right-going discontinuities respectively.

4.3.3 contact, tangential and rotational discontinuities

The solutions of Eqs. (4.32)-(4.34) that have a vanishing mass flux, $M_0 = 0$, but a non-vanishing normal component of magnetic field, $B \neq 0$, are called contact discontinuities and satisfy the following relations:

$$\hat{v} = \text{arbitrary}, \quad \hat{p} = 1, \quad \hat{\boldsymbol{B}}_t = \boldsymbol{A}, \tag{4.37}$$

$$[\![\boldsymbol{v}]\!] = \boldsymbol{0}. \tag{4.38}$$

The solutions with $M_0 = 0$ and $B = 0$, on the other hand, are named tangential discontinuities, for which the following relations hold:

$$\hat{v} = \text{arbitrary}, \quad \hat{p} - 1 + \frac{1}{2}(\hat{\boldsymbol{B}}_t{}^2 - \boldsymbol{A}^2) = 0, \tag{4.39}$$

$$[\![v_n]\!] = 0, \quad [\![\boldsymbol{v}_t]\!] = \text{arbitrary}. \tag{4.40}$$

The last equation in Eq. (4.39) means that the total pressures are equal on both sides of the discontinuity.

The solution with $M_0 \neq 0$ and $B \neq 0$ is either a linear wave ($\hat{v} = 1$) or a shock wave ($\hat{v} > 1$). The former is referred to as a rotational discontinuity, since the transverse component of magnetic field rotates, not varying its magnitude during its passage. The rotational discontinuities meet the following conditions:

$$\hat{v} = 1, \quad \hat{p} = 1, \quad \hat{\boldsymbol{B}}_t{}^2 = \boldsymbol{A}^2, \quad M_0^2 = \frac{B^2}{\gamma}, \tag{4.41}$$

$$[\![v_n]\!] = 0, \quad [\![\boldsymbol{v}_t]\!] = \pm\frac{1}{\sqrt{\rho}}[\![\boldsymbol{B}_t]\!], \tag{4.42}$$

where the plus and minus signs correspond to the left- and right-going waves respectively. These relations imply that the upstream and downstream Mach numbers are equal to the ratio of the Alfvén velocity to the acoustic speed there.

All the above discontinuities satisfy the evolutionary conditions except for the rotational discontinuity in which the transverse magnetic field rotates by 180°. The latter is sometimes called weakly evolutionary in the literature (Jeffrey & Taniuti, 1964), since the neighboring rotational discontinuities are all evolutionary. Following this point of view, we treat the solutions with weakly evolutionary discontinuities as regular solutions in this thesis.[1]

4.3.4 shock waves

The solutions of Eqs. (4.32)-(4.34), for which $M_0 \neq 0$ and $\hat{v} > 1$, i.e., the matter is compressed as it passes through the discontinuities, are called shock waves. Their notable feature is that magnetic fields are either planar or coplanar. This is apparent from Eq. (4.33). Indeed, recalling $\hat{v} > 1$, we obtain

$$\hat{\boldsymbol{B}}_t = \frac{\gamma M_0^2 - B^2}{\gamma M_0^2 \hat{v} - B^2}\boldsymbol{A}. \tag{4.43}$$

[1]This may need reconsideration, however, and will be addressed elsewhere.

Substituting $v_{n1} = \hat{v} v_{n0}$ in order to eliminate $\hat{v}$, we also obtain the following relation:

$$\hat{\boldsymbol{B}}_t = \frac{v_{n0}^2 - c_{A0}^2}{v_{n1}^2 - c_{A1}^2} \boldsymbol{A}, \tag{4.44}$$

which shows immediately that transverse magnetic fields are coplanar if and only if the upstream flow velocity is super-Alfvénic whereas the downstream speed is sub-Alfvénic.

The shocks with planar transverse magnetic fields are either fast or slow shocks, the former of which amplifies the magnitude of transverse magnetic fields whereas the latter reduces it. The shocks that change the direction of transverse magnetic fields are referred to as intermediate shocks. The fast and slow shocks are evolutionary whereas the intermediate ones are non-evolutionary as pointed out below.

Recalling $c_f \geq c_A \geq c_s$, we assign 1 to the states with super-fast velocities, 2 to those with sub-fast and super-Alfvénic velocities, 3 to those with sub-Alfvénic and super-slow velocities and 4 to those with sub-slow velocities in the shock-rest frame. With this allocation, the fast shock is denoted by $1 \to 2$ shock, since the upstream velocity is super-fast (state 1) whereas the downstream speed is sub-fast and super-Alfvénic (state 2) (e.g. De Sterck, 1999). Similarly the slow shock is designated as $3 \to 4$ shocks. The intermediate shocks normally belong to one of the following four types: $1 \to 3$, $1 \to 4$, $2 \to 3$ and $2 \to 4$ shocks. The $1 \to 3$ and $2 \to 4$ intermediate shocks are called over-compressive shocks and 9 out of $14 (= 7 \times 2)$ characteristics run into these shock waves. To the $1 \to 3$ and $2 \to 4$ shocks converge the fast and Alfvén characteristics and the Alfvén and slow characteristics respectively. The $1 \to 4$ intermediate shock is doubly over-compressive and 10 characteristics of all types go into the shock. In the case of $2 \to 3$ shock, only the Alfvénic characteristic converges to the shock wave and the numbers of in- and out-going waves are right. However, the other condition on the linear independence of eigenfunctions is violated and the shock is hence classified as non-evolutionary.

In some cases, the flow velocity coincides with one of the characteristic velocities. We employ a pair of numbers to specify those states; "$1, 2$ ", "$2, 3$" and "$3, 4$" represent those states whose flow speed are equal to the fast, Alfvén and slow speeds respectively. The shock wave with the upstream velocity being super-Alfvénic and the downstream speed being equal to the slow velocity, for example, is designated as $2 \to 3, 4$ shocks. Of our special concern among these intermediate shocks are the so-called switch-on $(1 \to 2, 3)$ and switch-off $(2, 3 \to 4)$ shocks, the details of which will be given shortly. Note that none of the intermediate shocks and switch-on/off shocks satisfies the evolutionary conditions.

fast and slow loci

We regard the shock solutions of (4.32)-(4.34) as functions of the upstream Mach number (M_0), normal (B) and transverse ($\hat{\boldsymbol{B}}_t$ or $\boldsymbol{A}$) components of magnetic field. Then we divide them into two families and look into their loci in some detail. Since magnetic fields in shock waves are either planar or coplanar as pointed out earlier, we assume without loss of generality that magnetic fields are confined in the (x, y)-plane and treat $\hat{B}_t$ and A (≥ 0) as scalar variables in the following.

Eliminating $\hat{p}$ and $\hat{B}_t$ from (4.32)-(4.34), we obtain the following cubic equation for the specific volume, $\hat{v}$:

$$\begin{aligned}
&(\gamma M_0^2\hat{v})^3 - \left[\frac{2}{\gamma+1} + \frac{\gamma-1}{\gamma+1}\gamma M_0^2 + 2B^2 + \frac{\gamma A^2}{\gamma+1}\right](\gamma M_0^2\hat{v})^2 \\
&+ \left[2B^2\left(\frac{2\gamma}{\gamma+1} + \frac{\gamma-1}{\gamma+1}\gamma M_0^2\right) + B^4 - \frac{2-\gamma}{\gamma+1}\gamma M_0^2 A^2 + A^2B^2\right]\gamma M_0^2\hat{v} \\
&- \left[B^4\left(\frac{2\gamma}{\gamma+1} + \frac{\gamma-1}{\gamma+1}\gamma M_0^2\right) + \frac{\gamma-1}{\gamma+1}\gamma M_0^2 A^2 B^2\right] = 0,
\end{aligned} \tag{4.45}$$

where we used the assumption of $\hat{v} \neq 1$ in deriving the equation. Or, alternatively, we obtain the following quadratic equation for the specific volume by eliminating M_0:

$$\begin{aligned}
&\left\{\frac{\hat{B}_t}{2}\left[\frac{4\gamma}{\gamma-1} + (\hat{B}_t - A)^2 + \frac{\gamma+1}{\gamma-1}(A^2 - \hat{B}_t^2)\right] - \frac{\gamma+1}{\gamma-1}B^2(\hat{B}_t - A)\right\}\hat{v}^2 \\
&+\frac{2\gamma}{\gamma-1}\left[\frac{A}{2}(\hat{B}_t^2 - A^2) + B^2(\hat{B}_t - A) - (\hat{B}_t + A)\right]\hat{v} \\
&+\frac{2\gamma A}{\gamma-1} - (A^2 + B^2)(\hat{B}_t - A) = 0.
\end{aligned} \tag{4.46}$$

The family of fast shocks is the solutions characterized by the feature that the matter is compressed and the transverse magnetic field is amplified by the passage. It is then found that this branch of solutions satisfies the inequality $\hat{v}_{\min} < \hat{v} < 1$, where the minimum is given by

$$\hat{v}_{\min} = \max\left(\frac{B^2}{\gamma M_0^2}, \frac{\gamma-1}{\gamma+1}\right). \tag{4.47}$$

The loci of the solutions are shown in Fig. 4.2 as a function of the upstream Mach number (M_0) for some combinations of the upstream normal (B) and transverse (A) components of magnetic fields. As seen in the figure, the fast shocks can be

parameterized by the upstream Mach number if one fixes the other parameters (A and B), which are given by the upstream variables. The only case where some special treatment is required is seen in the right panel of Fig. 4.2, where the fast locus is divided into two branches for the special case of $A = 0$ with Mach numbers satisfying the following inequalities:

$$\hat{c}_{f0} < M_0 < \sqrt{\frac{\gamma+1}{\gamma-1}\frac{B^2}{\gamma} - \frac{2}{\gamma-1}}, \tag{4.48}$$

where $\hat{c}_{f0} := c_{f0}/a_0$ is a normalized fast velocity. One of the branches that generates non-vanishing transverse magnetic fields by the shock passage is called the switch-on shock branch and the other is referred to as the Euler shock branch, in which the transverse components of magnetic fields remain zero. The post-shock specific volume and transverse magnetic field are given by

$$\hat{v} = \frac{2+(\gamma-1)M_0^2}{(\gamma+1)M_0^2}, \quad \frac{B^2}{\gamma M_0^2}, \tag{4.49}$$

$$\hat{B}_t = 0, \quad \sqrt{\frac{\gamma M_0^2 - B^2}{B^2}\left[(\gamma-1)\left(\frac{\gamma+1}{\gamma-1}B^2 - \gamma M_0^2\right) - 2\gamma\right]}, \tag{4.50}$$

respectively. In the above expressions, the first options correspond to the Euler shocks and the second ones to the switch-on shocks. The requirement that the quantity in the square root be non-negative gives the inequality (4.48).

It is noted that the flow speed behind switch-on shocks is equal to an Alfvén speed. They are hence designated as $1 \to 2, 3$ shocks and are non-regular. We also note that Euler shocks are essentially hydrodynamical shock waves and the locus is extended to $M_0 < \hat{c}_{f0}$, where it is smoothly connected to the slow-shock counterpart. They are evolutionary except the range within which the switch-on shock branch appears, i.e., the range satisfying the inequality (4.48).

The slow family is characterized by the feature that the matter is compressed but the transverse magnetic field is reduced and in some cases reversed by the shock passage. The slow loci are shown in Fig. 4.3 as a function of the upstream Mach number (M_0) for a number of combinations of the upstream normal (B) and transverse (A) components of magnetic fields. It is evident that some loci are two-valued as a function of M_0. In the figure, the intermediate shocks are those that give a negative downstream transverse magnetic field. The shocks that nullify the transverse magnetic field are called switch-off shocks ($2, 3 \to 4$ shocks). They are located at the boundary between the regular slow shocks and the intermediate shocks. Each locus

is terminated at the point that corresponds to a rotational discontinuity, which is incompressible and rotates magnetic field by 180°, i.e., $\hat{B}_t = -A$.

The minimum value of the downstream transverse magnetic field, $\hat{B}_{t,\min}$, is given as

$$\hat{B}_{t,\min} = -\frac{4(B^2-\gamma)^2 + \gamma^2 A^4 + 4A^2(B^2+\gamma^2)}{2\gamma AB^2 + \gamma(2-\gamma)A(2+A^2) + 4B\sqrt{(\gamma-1)\Delta(A,B)}}, \tag{4.51}$$

$$\Delta(A,B) := (B^2-\gamma)^2 + A^2\frac{\gamma(\gamma^2-2\gamma+2)}{\gamma-1} + A^2(2B^2+A^2), \tag{4.52}$$

which satisfies the condition that the discriminant of (4.46) becomes zero (Torrilhon, 2002). Note that $\hat{B}_{t,\min} \leq -A$ as seen in the figure. We shall divide a locus by this minimum point. The part from the maximum in $(M_0, \hat{B}_t)$-plane, i.e., corresponding to $\hat{B}_t = A$, to the minimum is called the 'plus-branch', named after a fact that the branch gives a larger $\hat{v}$ in (4.46) (Torrilhon, 2002). The other part, from the minimum to the end point, is called the 'minus-branch', which gives a smaller $\hat{v}$. Note that the minus-branch does not always exist as seen in the figure. In the limit of $B \to 0$ or $A \to 0$, the whole slow branch vanishes. That is, there is no solution that satisfies (4.45) and the inequalities: $\hat{c}_{s0} < M_0 < \hat{c}_{f0}$ and $0 < \hat{v} < 1$, except when $A = 0$ and the upstream Alfvén speed is larger than the acoustic speed, i.e., $\hat{c}_{A0}(:= c_{A0}/a_0) > 1$, in which case the Euler shock branch takes its place. This Euler branch is extended to the regime of $M_0 > \hat{c}_{f0}$ and connected smoothly to the fast-shock counterpart as mentioned earlier.

4.3.5 shock waves with no normal magnetic fields

Without normal magnetic fields, the structure of the shock solutions becomes much simpler because the slow shock loci disappear. In fact, (4.45) becomes a quadratic equation with the assumption of $\hat{v} \neq 0$ and one obtains a unique solution by discarding the solutions that satisfy $\hat{v} \leq 0$:

$$\hat{v} = \frac{(\gamma-1)M_0^2 + A^2 + 2}{2(\gamma+1)M_0^2} + \sqrt{\left[\frac{(\gamma-1)M_0^2 + A^2 + 2}{2(\gamma+1)M_0^2}\right]^2 + \frac{(2-\gamma)A^2}{\gamma(\gamma+1)M_0^2}}. \tag{4.53}$$

The solution belongs to the family of fast shocks because the transverse magnetic field behind the shock is amplified, which follows from (4.33). Otherwise the shock is an Euler shock provided there is no transverse magnetic field. It is noteworthy here that switch-on shocks are never realized when no normal magnetic fields exist.

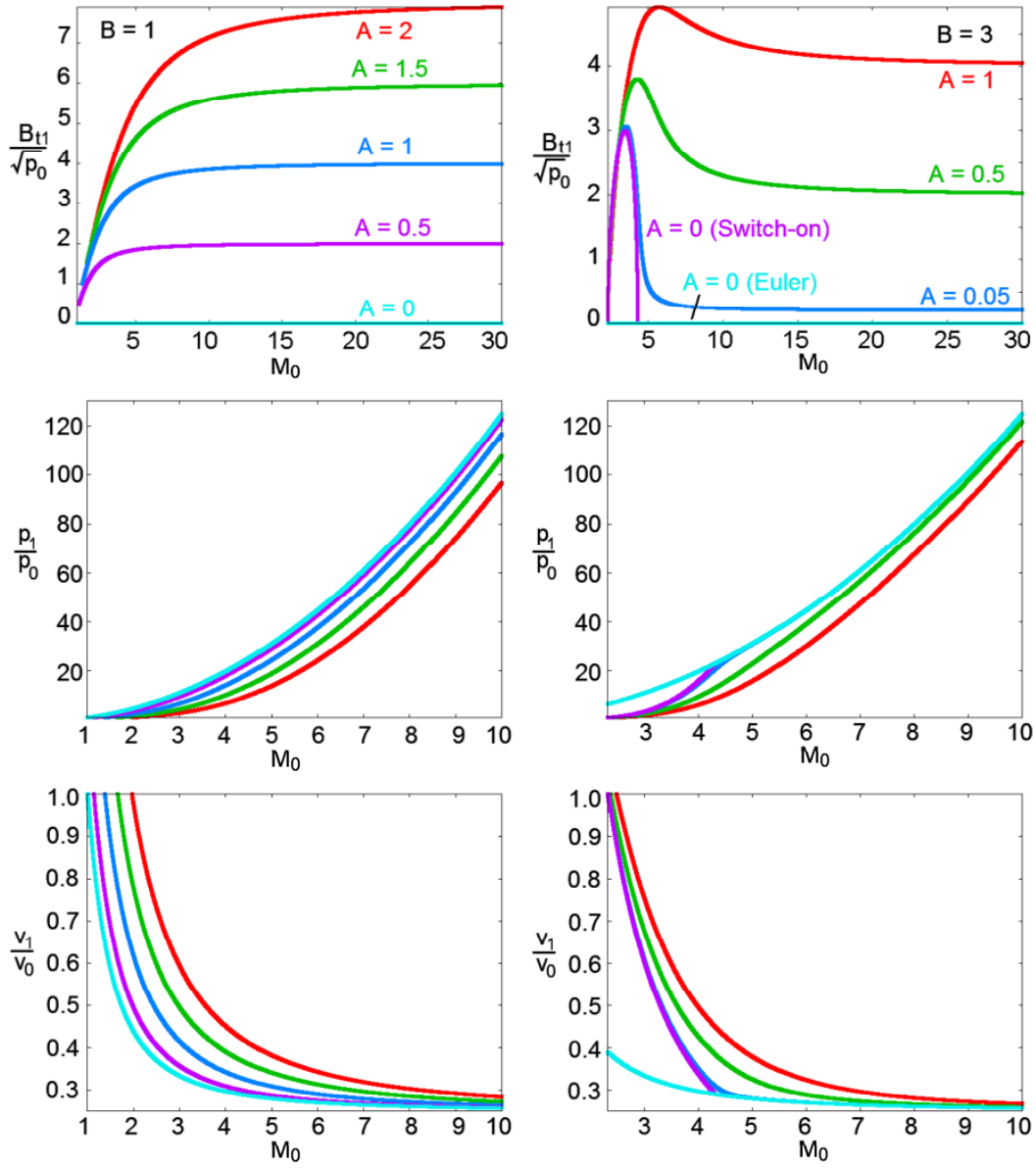

Figure 4.2: The fast loci for different combinations of the normal (B) and transverse (A) component of magnetic field. The left panels: $B = 1$ and $A = 2$ (red), 1.5 (green), 1 (blue), 0.5 (purple) and 0 (light blue). The right panels: $B = 3$ and $A = 1$ (red), 0.5 (green), 0.05 (blue), 0 (purple, switch-on shock) and 0 (light blue, Euler shock). The switch-on shock does not exist for $B = 1$. See the text for details.

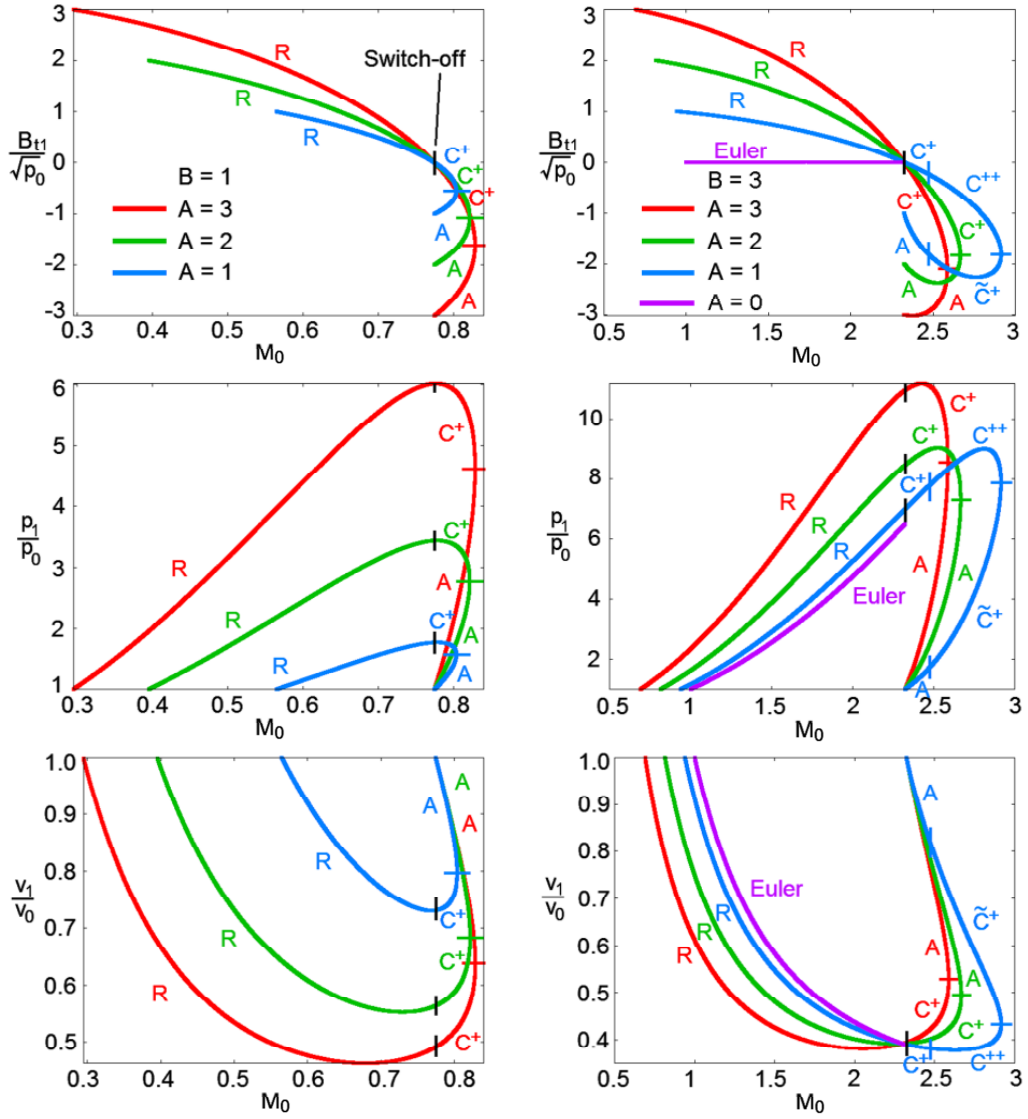

Figure 4.3: The slow loci for different combinations of the normal (B) and transverse (A) component of magnetic field. The left panels: $B = 1$ and $A = 3$ (red), 2 (green) and 1 (blue). The vertical black dashes indicate the points, at which $M_0 = \hat{c}_{A0}$ and switch-off shocks ($2, 3 \to 4$ shocks) occur. Since $\hat{c}_{A0}$ is independent of A, the Mach numbers, M_0's, at the points for all loci coincide with one another. These points mark the boundary between the regular slow shocks and non-regular intermediate shocks. The characters, R, C^+ and A, attached to each locus stand for the regular slow ($3 \to 4$), $2 \to 4$ intermediate and $2 \to 3$ intermediate shocks, respectively. The horizontal dash on each locus shows the point, at which the Mach number reaches its maximum on the locus and a $2 \to 3, 4$ shock occurs. This is the boundary between the $2 \to 4$ (C^+) and $2 \to 3$ (A) intermediate shocks. The right panels: $B = 3$ and $A = 3$ (red), 2 (green), 1 (blue) and 0 (purple, Euler shocks). The vertical black dashes again give the boundary between the regular and non-regular shocks, at which switch-off shocks ($2, 3 \to 4$ shocks) occur. The characters, R, C^+ and A, have the same meaning as in the left panels whereas C^{++} and $\tilde{C}^+$, which emerge only for small A's, represent the $1 \to 4$ and $1 \to 3$ intermediate shocks, respectively. The horizontal dash on each locus marks again the point, at which the maximum Mach number is reached. On the other hand, the two vertical blue dashes on each blue locus indicate the points, at which $M_0 = \hat{c}_{f0}$. A $1, 2 \to 4$ shock occurs at the point closer to the vertical black dashes whereas a $1, 2 \to 3$ shock emerges at the other point. A $1 \to 3, 4$ shock occurs at the point indicated by the horizontal blue dash. Note in passing that the locus vanishes at $B = 0$.

4.4 How to solve MHD Riemann problems I: the regular solutions without switch-off rarefactions

4.4.1 structure of the regular solutions without switch-off rarefactions

We review here the way to find regular solutions, in which no non-regular shock exists, in the case that neither normal nor transverse magnetic field vanishes in order to show the basic idea to solve Riemann problems. Then we propose a new strategy to obtain non-regular solutions, which can also handle vanishing magnetic fields, in the next sub-section.

Assuming that both normal and transverse magnetic fields have some finite values initially on both sides and ignoring intermediate shocks and switch-off waves, the structure of the solutions is known *a priori*: fast, Alfvén, and slow waves fanning out in this order on both sides of a contact discontinuity. Since each wave forms a one-parameter family and seven waves exist in the solutions, the structure of a solution is determined by fixing the seven parameters. One of degrees of freedom is the magnitude of a jump of density at the contact discontinuity, where other six quantities, i.e., pressure, three components of the velocity field and two components of the transverse magnetic field, should be continuous. Therefore solving the MHD Riemann problems reduces to finding the six parameters that satisfy a requirement that the six quantities other than density are continuous across the contact discontinuity. Then remaining parameter associated with the contact discontinuity is necessarily determined. Furthermore, we can omit another degree of freedom that parameterizes a rotational discontinuity in either side as pointed out by Torrilhon (2002). Thanks to the fact that only the rotational discontinuities can rotate magnetic fields, if an angle of the rotation is fixed on either side, then another angle on the other side is necessarily determined to adjust the angle of the transverse magnetic field. Eventually, there remain five parameters that should be determined to satisfy the conditions of continuity at the contact discontinuity.

The five parameters can be found, e.g., by the Newton-Raphson method and the system of equations to be solved is schematically given as

$$\boldsymbol{F}^s_L(\psi_s^-;\boldsymbol{u}^r_L(\psi_r;\boldsymbol{u}^f_L(\psi_f^-;\boldsymbol{u}_L))) - \boldsymbol{F}^s_R(\psi_s^+;\boldsymbol{u}^r_R(\psi_r;\boldsymbol{u}^f_R(\psi_f^+;\boldsymbol{u}_R))) = \boldsymbol{0}, \tag{4.54}$$

where $\psi_f^{\mp}$, $\psi_s^{\mp}$ and ψ_r are the parameters of the left/right fast wave, left/right slow wave and rotational discontinuity respectively. $\boldsymbol{u}_{L,R}$ is a given initial state on

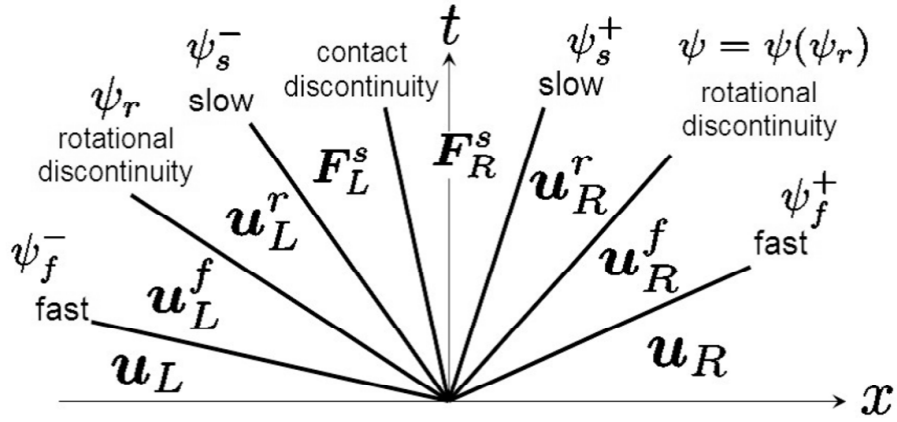

Figure 4.4: A schematic picture of the regular solution of the MHD Riemann problem in (x, t)-plane. There are generally seven waves, i.e., a contact discontinuity and fast waves, rotational discontinuities and slow waves running in both sides, provided the solution is restricted to a regular one. The letters with suffices, ψs, attached to each wave stand for the parameters of each wave. The other characters with suffices, $\boldsymbol{u}$s and $\boldsymbol{F}$s, represent vectors of the conserved quantities in each states and vectors of the quantities which should be continuous across the contact discontinuity respectively.

left/right side, i.e., $\boldsymbol{u}_{L,R} = {}^t(\rho_{L,R}, p_{L,R}, \boldsymbol{v}_{L,R}, \boldsymbol{B}_{tL,R})$. $\boldsymbol{u}^f_{L,R}$ is the left/right fast-wave function, which represents the downstream state of the fast wave and is a function of upstream variables, $\boldsymbol{u}_{L,R}$, and a parameter of the fast wave, $\psi_f^{\mp}$. Similarly, $\boldsymbol{u}^r_{L,R}$ is the left/right rotational discontinuity function and $\boldsymbol{F}^s_{L,R}$ is the left/right slow-wave function. Here, the slow-wave function represents the five downstream variables of the slow wave that have to be continuous across the contact discontinuity, i.e., p, $\boldsymbol{v}$ and $|\boldsymbol{B}_t|$. See also a schematic picture of regular solutions presented in Fig. 4.4.

4.4.2 parameterization of the regular waves

Although each wave forms a one-parameter family as mentioned earlier, it is not a simple task to find the variables that are convenient to control each wave. For

instance, the slow shock family seems to have no convenient variables to parameterize the Hugoniot loci that include the non-regular branch. We review here a parameterizations to handle the regular waves by neglecting intermediate shocks and switch-on/off waves (see also Torrilhon, 2002).

The problem is how to map the parameters of the waves, which are directly improved by the Newton-Raphson method, to physical quantities, which have some appropriate ranges. For example, the fast waves with the shock- and rarefaction-wave branches form a one-parameter family and let ψ_f denote the parameter of the waves. ψ_f is improved by the Newton-Raphson method as well as the other parameters, ψs, which are associated with the other waves (we here omit the plus and minus signs for notational simplicity) and the domain of the parameters is $\mathbb{R}$. On the other hand, fast shocks can be parameterized by the Mach number, $M_0 \in [\hat{c}_{f0}, \infty)$, as mentioned earlier and fast rarefactions can be parameterized by the length of a fast rarefaction locus in phase space, s.[2] That is, the state behind a rarefaction wave, $\boldsymbol{r}_{\rm behind}$, can be described as

$$\boldsymbol{r}_{\rm behind} = \int_0^s \boldsymbol{r}_f(s')\mathrm{d}s'. \tag{4.55}$$

Note that $s \in [0, s_{\rm max})$, where $s_{\rm max}$ corresponds to the maximum strength of the fast rarefaction wave, i.e., the strength of a switch-off rarefaction. Now, our concern is to construct a function that maps ψ_f into M_0 or s.

Ignoring switch-off rarefactions and switch-on shocks, one can define the fast-wave function as (Torrilhon, 2002)

$$\begin{cases} M_0 = \hat{c}_{f0} + \psi_f & (\psi_f > 0) \quad \text{(Shock)}, \\ s = s_{\rm max}\tanh(-\psi_f) & (\psi_f \le 0) \quad \text{(Rarefaction)}. \end{cases} \tag{4.56}$$

By this parameterization, the fast wave is given as the fast shock whose strength is determined by the upper part of (4.56) for positive ψ_f while it is the fast rarefaction whose strength is given by the lower part of (4.56) for non-positive ψ_f and it is never a switch-off rarefaction. The fast-shock solution is obtained from the cubic equation (4.45) by substituting the M_0. Although there are three roots in general (Delmont & Keppens, 2011), we can easily pick up the correct root that corresponds to a fast shock as described in Sec. 4.6.6. In the above expression, we omitted the case of $M_0 = \hat{c}_{f0}$ because both $s = 0$ and $M_0 = \hat{c}_{f0}$ mean that there is no fast

[2] The rarefaction locus in phase space connects the points that correspond to the state in front of the rarefaction wave and a state behind it. The locus is constructed by integrating the eigenvector, $\boldsymbol{r}_f$. Hence, the behind state is uniquely given by the length of the locus, s, once the front state is given.

wave. Note also that (4.56) is applicable to both left-going and right-going fast waves while we omitted plus and minus signs from the variables, $M_0, \hat{c}_{f0}, \psi_f, s$ and $s_{\max}$, for notational simplicity.

Similarly, discarding the non-regular branch, the slow family can be constructed as

$$\begin{cases} \hat{B}_t = A(1 - \tanh(\psi_s)) & (\psi_s > 0) \quad \text{(Shock)}, \\ s = -\psi_s & (\psi_s \leq 0) \quad \text{(Rarefaction)}. \end{cases} \tag{4.57}$$

Here, s is the length of a slow rarefaction locus in phase space. The ranges of this transformation are $\hat{B}_t \in (0, A)$ and $s \in [0, \infty)$. Therefore only regular slow shocks are possible and neither switch-off nor intermediate shocks are realized. We omitted the case of $\hat{B}_t = A$ here in order to prevent from doubly counting the situation that there is no slow wave, which is also described as $s = 0$. Note that (4.57) is applicable to both left-going and right-going slow waves.

With respect to rotational discontinuities, the degree of freedom is the rotational angle of the transverse magnetic field. Hence the parameter, ψ_r, can be transformed into the rotational angle, φ, as

$$\varphi \equiv \psi_r \pmod{2\pi}. \tag{4.58}$$

This relation is used only for a rotational discontinuity on either side because the rotational angle on the other side is necessarily fixed as mentioned in Sec. 4.4.1; The angle is automatically adjusted to $\theta_L - \theta_R + \varphi$, where $\theta_{L,R}$ are the initial rotational angles of the magnetic fields on the left and right sides respectively. If ψ_r is the parameter of the right rotational discontinuity, then the rotational angle on left side should be $\theta_R - \theta_L + \varphi$.

4.5 How to solve MHD Riemann problems II: the solutions with intermediate shocks, switch-on/off shocks or switch-on/off rarefactions

In this section, we discuss the solutions of MHD Riemann problems, including intermediate shocks, switch-on/off shocks and switch-on/off rarefactions. Furthermore, we take into account the initial conditions with vanishing magnetic fields. There are mainly two differences from the previous section. Firstly, the parameterizations of waves should be modified to cover all the branches. Secondly, the structure of non-regular solutions cannot be known *a priori* because some waves prohibit the

emergence of other waves: If a left-going $2 \to 4$ intermediate shock exists, for example, then the left-going rotational discontinuity and slow wave do not appear in the solution because $2 \to 4$ intermediate shocks skip the Alfvén and slow speeds. Therefore all the possible combinations of waves should be tried to find the solution and the procedure to construct the solution should arrange the waves in appropriate order. We discuss the parameterizations of the waves at first. Then we discuss the arrangement of the waves, which is associated with the parameterization, in the latter part.

4.5.1 parameterization of the non-regular shocks and switch-on/off rarefactions

Including switch-off rarefactions, we modify the fast-wave function (4.56) as follows.

$$\begin{cases} M_0 = \hat{c}_{f0} + \psi_f & (0 \le \psi_f) & \text{(Shock)}, \\ s \quad = \begin{cases} -\psi_f & (-s_{\max} < \psi_f < 0) & \text{(Rarefaction)}, \\ s_{\max} & (\psi_f \le -s_{\max}) & \text{(Switch-off rarefaction)}, \end{cases} \end{cases} \tag{4.59}$$

where we omitted plus and minus signs for notational simplicity as in the previous section. This function gives a switch-off rarefaction if $\psi_f \le -s_{\max}$. Note, however, that (4.59) is no longer injective since $\psi_f \le -s_{\max}$ always gives a certain value, $s_{\max}$. This property may cause a trouble in the Newton-Raphson iteration, where the derivative of the function is required, and the issue is discussed in Sec. 4.6.1. Note also that the shock's part of (4.59) may not determine the downstream state uniquely because the two branches, the switch-on branch and ordinary Euler one, exist for a given Mach number provided the upstream transverse magnetic field is absent and the upstream Mach number satisfies the inequality (4.48). We need hence other rules to choose a branch to determine the downstream state uniquely. In our code, this degree of freedom remains as a setting parameter, i.e., we select a branch before running the program. If one chooses the switch-on shock branch, one should set the direction of the downstream transverse magnetic field as well because the shock can produce the field in an arbitrary direction. There is a good way, however, to adjust the direction automatically for the initial conditions where the transverse magnetic filed is absent on only one side. For such conditions, one does not have to mind the direction beforehand and the way is presented later.

For slow waves, the intermediate shock branches and switch-on rarefactions should be included. No special modification is necessary for the rarefactions while the pa-

rameterization of slow shocks becomes rather complicated, which is given as

$$\begin{cases} \hat{B}_t = g(A, \hat{B}_{t,\min}, \psi_s) & (\psi_s > 0) \quad \text{(Discontinuity)}, \\ s = -\psi_s & (\psi_s \leq 0) \quad \text{(Rarefaction)}, \end{cases} \tag{4.60}$$

where $\hat{B}_{t,\min}$ is the minimum value of the transverse magnetic field in the slow Hugoniot locus given by (4.51). The function g is defined for $A > 0$ by

$$g(A, \hat{B}_{t,\min}, \psi_s) = \begin{cases} A - \psi_s & (0 < \psi_s \leq A + |\hat{B}_{t,\min}|), \\ \psi_s - A - 2|\hat{B}_{t,\min}| & (A + |\hat{B}_{t,\min}| < \psi_s \leq 2|\hat{B}_{t,\min}|), \\ -A & (2|\hat{B}_{t,\min}| < \psi_s). \end{cases} \tag{4.61}$$

The range of the top equation in (4.61) is $[\hat{B}_{t,\min}, A) \ni \hat{B}_t$ while that of the middle one is $(\hat{B}_{t,\min}, -A] \ni \hat{B}_t$. Note that the post-shock state may not be determined uniquely by (4.61) because two branches can exist for a given $\hat{B}_t$ as mentioned in Sec. 4.3.4. Hence we divide the slow Hugoniot loci into 'plus-branches' and 'minus-branches' as mentioned earlier. We take the quantities from the plus-branch, which includes regular slow shocks, a switch-off shock and a portion of the intermediate shock branch, for $\psi_s \in (0, A + |\hat{B}_{t,\min}|]$, i.e., corresponding to the top equation in (4.61). Otherwise, we use the minus-branch, which includes a part of intermediate shocks and the rotational discontinuity located at the end point, for $\psi_s \in (A + |\hat{B}_{t,\min}|, \infty)$, corresponding to the middle and bottom equations. In case that there is no minus-branch, i.e., $\hat{B}_{t,\min} = -A$, the domain for the middle equation becomes the empty set. Another noteworthy property is that the function gives 180° rotational discontinuities, i.e., $\hat{B}_t = -A$ and $\hat{v} = 1$, provided $\psi_s \in (2|\hat{B}_{t,\min}|, \infty)$, reflecting the fact that the terminating points of slow Hugoniot loci give 180° rotational discontinuities. The advantage that stems from this property is discussed in Sec. 4.6.4. For $A = 0$, i.e., when the upstream transverse magnetic field is absent, the Euler shock branch may traverse the slow and fast Hugoniot locus plane. The Euler shocks that belong to a slow branch can be parameterized as follows:

$$M_0 = 1 + (\hat{c}_{f0} - 1)\tanh(\psi_s) \quad (\psi_s > 0). \tag{4.62}$$

This function maps ψ_s into the upstream Mach number of the Euler shock, $M_0 \in (1, \hat{c}_{f0})$. And we use this function instead of g in order to treat the slow shock.

With respect to rotational discontinuities, we use the same function (4.58) for determining a rotational angle provided neither intermediate shock nor switch-off wave exists in the solution. Once intermediate shocks or switch-off waves emerge, however, the degree of freedom associated with a rotational discontinuity disappears

as discussed below. We begin from the case that an intermediate shock or a switch-on/off wave exists only in one side: (i) If an intermediate shock exists, the rotational discontinuity is skipped by the shock and the transverse magnetic field is reversed in the side. As a result, the rotational angle on the other side is necessarily fixed to $\theta_{L,R} - \theta_{R,L} + \pi$ for the right/left side to adjust the direction of the field. (ii) If a switch-off shock ($2, 3 \to 4$ shock) or switch-off rarefaction exists, the wave quenches the transverse magnetic field and, as a consequence, the rotational discontinuity vanishes. And no wave produces the magnetic field in the side since only an ordinary rarefaction or ordinary Euler shock can exist behind the switch-off waves. This situation requires that any switch-off wave also appears on the other side and, as a result, the rotational discontinuity disappears. When such waves that prohibit the rotational discontinuity emerge in both sides, no rotational discontinuity exists in the solution, of course. In this way, if non-regular shocks or switch-off rarefactions emerge in one side, we do not need consider the rotational angle of the rotational discontinuity in the other side, if any. The problem associated with the disappearance of the degree of freedom is discussed in Sec. 4.6.1.

4.5.2 structure of the non-regular solutions and how to arrange the waves

We discuss here the structure of non-regular solutions and propose a process to arrange the waves in the appropriate order, which is associated with the parameterization that was discussed in the previous sub-section. As mentioned repeatedly, the structure of the solution is not known *a priori* when the non-regular shocks and switch-on/off rarefactions are included and all possible combinations of waves should be tried to find the solution. Our method realizes this requirement: It searches all the patterns and finds the solution automatically in the Newton-Raphson iterations.

The outline of the process to arrange the waves is as follows. At first, we treat the waves that run in a side, say right, of the contact/tangential discontinuity, based on a given initial guess that controls the right-going waves. After arranging the right-going waves, we obtain the right state of the contact/tangential discontinuity. Then we treat the other side similarly and we will obtain the left state of the discontinuity, where the left and right states should satisfy the Rankine-Hugoniot conditions. Until the conditions are satisfied, the process is iterated by the Newton-Raphson method. Hereafter, we explain the process to arrange waves on the left side. The procedure on the other side is almost the same.

The case that both the transverse and normal magnetic fields exist in the left initial condition

We discuss the way to arrange the left-going waves in the case both the transverse and normal magnetic fields exist in the left initial condition. In this case, the first wave running in the left side is a fast-family wave, i.e., a fast rarefaction or fast shock, or an intermediate shock whose upstream speed in the rest frame is super-fast or equal to the fast speed, i.e., a '$1 \to 3$', '$1 \to 4$', '$1, 2 \to 3$', '$1, 2 \to 4$', '$1 \to 3, 4$' or '$1, 2 \to 3, 4$' shock.[3]

If the parameter that controls the left-going slow wave is positive, i.e., $\psi_s^- > 0$, we consider the pattern that includes such an intermediate shock at first and we try inserting an intermediate shock which is given by ψ_s^- and its upstream state through the slow-shock function (4.60). Note that the 'trial intermediate shock' may not satisfy the assumption that the upstream flow speed is not slower than the fast speed, $M_0 \geq \hat{c}_{f0}$, or the trial shock may not be even an intermediate shock since the function (4.60) includes regular slow shocks. Moreover, it is also possible that the slow shock branch does not include the intermediate shock that is appropriate now, as seen in the left panels in Fig. 4.3. In such cases, we reject the assumption that the leftmost wave is an intermediate shock and then we alternatively insert a fast wave as the leftmost wave, whose strength is given by ψ_f^- through the fast-wave function (4.59). Only if the shock satisfies $M_0 \geq \hat{c}_{f0}$, we accept the trial intermediate shock.

If $\psi_s^- \leq 0$, on the other hand, we need not consider any intermediate shock because $\psi_s^- \leq 0$ gives only slow rarefactions and hence the first wave is necessarily a fast wave, which is given by ψ_f^- through (4.59). We discuss below the case that the leftmost wave is (a) a fast wave or (b) an intermediate shock.[4]

(a): We further divide the situation into the four cases as follows. (a-i) $\psi_s^- \leq 0$ and the fast wave is not a switch-off rarefaction. (a-ii) $\psi_s^- \leq 0$ and the fast wave is a switch-off rarefaction. (a-iii) $\psi_s^- > 0$ and the fast wave is not a switch-off rarefaction. (a-iv) $\psi_s^- > 0$ and the fast wave is a switch-off rarefaction. Note that (a-i) and (a-ii) are the simplest cases, where no intermediate shock follows.

(a-i): In this case, the fast wave is followed by a rotational discontinuity and a slow rarefaction in this order. The slow rarefaction is controlled by ψ_s^- through the slow-wave function (4.60). The treatment of a rotational discontinuity is different

[3]It is shown that the shocks designated as '$1, 2 \to 2, 3$' do not exist.

[4]We should note that the intermediate shocks whose upstream flow speed is super-f
be discarded in some cases because a class of solutions may be missed as mentioned in Sec. 4.6.3. Due to this problem, we designed our code so that we choose whether we neglect such intermediate shocks or not before running the program. In the case that we discard such shocks, the path starts always at (a).

on the right and left sides. On the right side, where we assumed that the waves are arranged before the left side, the rotation angle is given by ψ_r through (4.58) while the counterpart on the left side is necessarily determined by the waves on the right side as mentioned in the previous sections.

(a-ii): Since the transverse magnetic field vanishes behind switch-off rarefactions, rotational discontinuities do not appear and only an ordinary rarefaction or ordinary Euler shock follows. We note here that behind switch-off rarefactions, $a_1 < c_{A1}$ is always satisfied, i.e., the fast speed and Alfvén speed always degenerate and the acoustic speed and slow speed coincide with each other. Therefore the ordinary wave belongs to the slow family and, hence, we here control it by $\psi_s^- \le 0$ through the slow-wave function (4.60). Since $\psi_s^- \le 0$ gives rarefactions, the third wave is necessarily an ordinary rarefaction wave.

(a-iii): When $\psi_s^- > 0$, we need consider the possibility of intermediate shocks for the second wave. Since the downstream state of the fast wave is designated as '2' or '1, 2' for the shocks and rarefactions respectively, the fast shock can be followed by a '$2 \to \star$' or switch-off ($2, 3 \to 4$) shock, where '$\star$' stands for '3', '4' or '3, 4', and the fast rarefaction can be also followed by one of these non-regular shocks or a '$1, 2 \to \star$' shock.[5] Therefore a trial intermediate shock is given again by ψ_s^- through (4.60). Note that the upstream quantities are now given by the downstream state of the fast wave. As before, the trial intermediate shock may not be an intermediate shock that is appropriate here and we should confirm that the shock does not overtake the preceding fast wave.[6] If the trial shock does not satisfy such conditions, we discard it and, as consequences, the following waves are a rotational discontinuity and a regular slow shock, which are handled in the same manner as in (a-i). If the trial shock is acceptable as the second wave, on the other hand, then the downstream state is designated as '3', '4' or '3, 4', i.e., $\hat{c}_{s1} < M_1 < \hat{c}_{A1}$, $M_1 < \hat{c}_{s1}$ or $M_1 = \hat{c}_{s1}$ respectively. For the second case, including the case of switch-off shocks, no wave follows and the non-regular shock is the last wave. For the third case, only a slow rarefaction can follow while the possible wave for the first case is either a slow rarefaction or regular slow shock whose shock speed is smaller than the preceding intermediate shock. Note, however, that there remains no parameter associated with the left slow wave because we have already used ψ_s^- for the intermediate shock. Hence we control the slow wave behind the intermediate shock by introducing an extra parameter, ψ_{ex}^-,

[5] It is shown that the shocks designated as '$2, 3 \to 3, 4$' do not exist.

[6] Note that the slow-shock function (4.60) contains a rotational discontinuity as mentioned earlier and rotational discontinuities can also be inserted behind the fast waves. We hence accept the rotational discontinuity that emerges as a trial 'shock' in this moment. The advantage of this treatment is discussed in Sec. 4.6.

which gives the strength of the slow wave through the regular-slow-wave function (4.57). This parameter is also iteratively improved by the Newton-Raphson method, which is discussed in Sec. 4.6.1.

(a-iv): As mentioned in (a-ii), the switch-off rarefaction is followed only by an ordinary wave. Since $\psi_s^- > 0$, the following wave is an ordinary Euler shock whose strength is given by ψ_s^- through the Euler-shock function (4.62).

(b): If the first wave is an intermediate shock, which is controlled by the slow function (4.60), then the downstream state is either '3', '4' or '3, 4'. Therefore the patterns of the following waves are the same as that discussed in the latter part of (a-iii); That is, no wave or an extra slow wave follows. Here, we also introduce the extra parameter ψ_{ex}^- for the slow wave.

Note that the number of the waves and, as consequences, the number of the free parameters are different for each case. The issue is associated with the way to treat the parameters in the Newton-Raphson method, which is discussed in Sec. 4.6.1.

The procedure to arrange the waves discussed above are summarized in Fig. 4.5 as a flow chart. In the figure, the functions entitled 'trial IS' give a trial intermediate shock whose strength is determined by ψ_s through (4.60). The 'Fast' functions give a fast wave, controlled by ψ_f through (4.59), including switch-off rarefactions. The 'Euler' function gives an ordinary Euler shock, controlled by ψ_s through (4.62). The 'Ordinary RW' function gives an ordinary rarefaction, controlled by ψ_s through (4.60). The 'Rot.' functions give a rotational discontinuity whose rotational angle is determined by ψ_r unless other rules determine the angle due to the waves on the other side. The 'Regular Slow' function gives a regular slow wave, controlled by ψ_{ex} through (4.57). The 'Slow RW' function gives a slow rarefaction, controlled by ψ_s or ψ_{ex} through (4.60). The 'Slow SW' function gives a regular slow shock, controlled by ψ_s through (4.57).

The case that the initial transverse magnetic field is absent in the left side

If the transverse magnetic field exists on the other side, then we arrange the waves from the right side. This is because some switch-on wave may emerge on the left side. Because the magnetic field should coincide at the contact discontinuity, the direction of the transverse magnetic field that is produced by the switch-on wave is necessarily determined by arranging the waves on the right side. In this sub-section, we suppose that we have already arranged the waves on the right side.

Without a transverse magnetic field, the fast and slow speeds degenerate into an Alfvén or acoustic speed, depending on the magnitudes of those speeds. Accordingly, we separately discuss the two situations: (p) $\hat{c}_{A0} \leq 1$ and (q) $\hat{c}_{A0} > 1$, where $\hat{c}_{A0}$ is

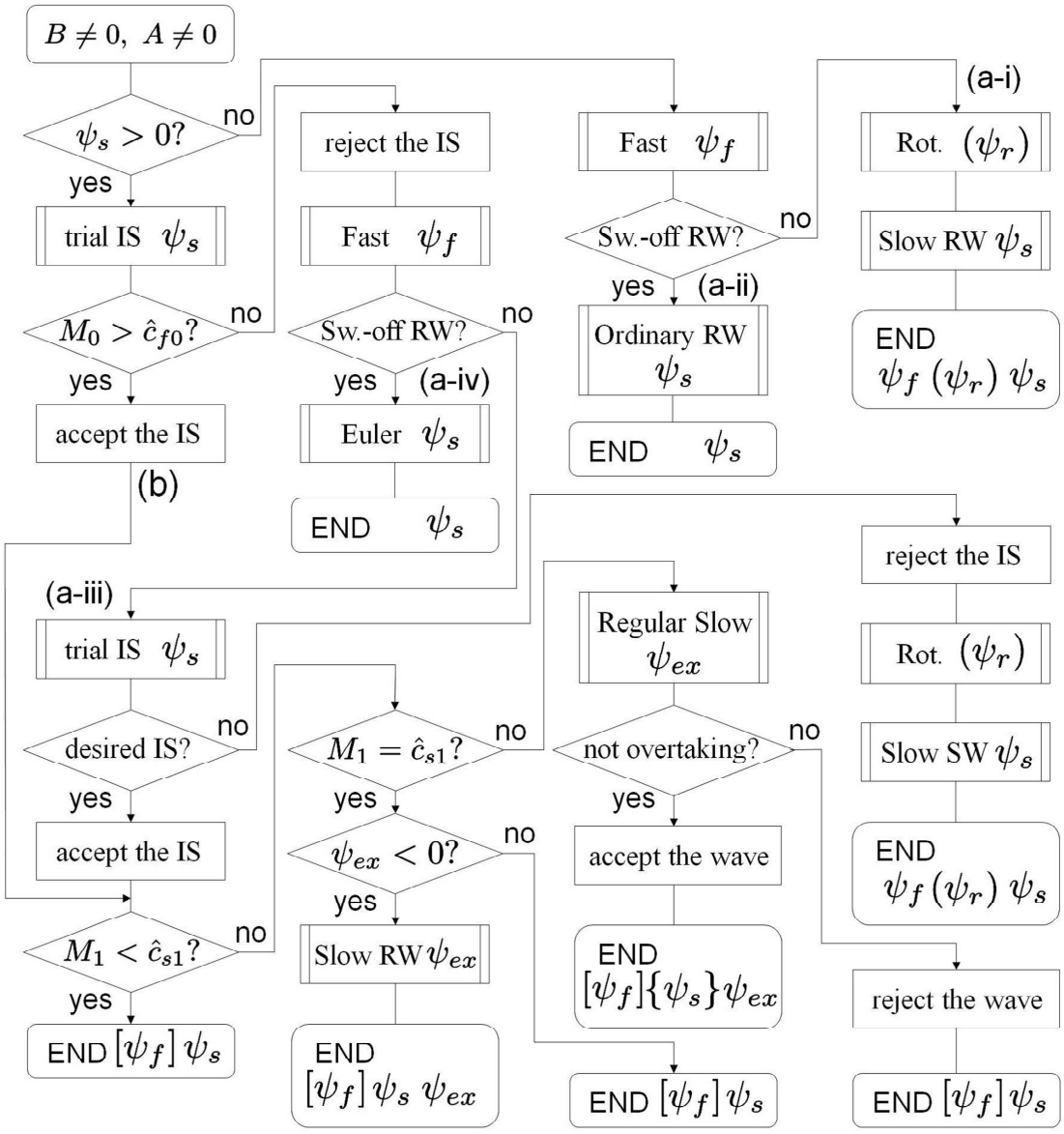

Figure 4.5: The flow chart for arranging the waves on one side where there are both the transverse and normal magnetic fields. The squares with double lines on each side represent the subroutines that insert a wave with the use of the corresponding function and parameter. The letters, ψs, that are attached to these functions are the parameters that are used in the subroutines. The designations, (a-i)-(a-iv) and (b), that are attached to the branches correspond to the paths that are mentioned in Sec. 4.5.2. The letters, ψs, in the terminals are the free parameters that are used in the path and improved by the Newton-Raphson method in the succeeding process. Note that a parameter given in square brackets mean that it is not a free parameter if the path passes through (b) as discussed in Sec. 4.6.1. Similarly, the letter in curly parentheses means that the parameter is not a free parameter only if the accepted trial 'shock' is a rotational discontinuity. The parameters given in round brackets mean that the parameter is not always used in the path.

the Alfvén speed of the given state normalized by the acoustic speed.

(p): As shown in Sec. 4.6.5, there is no chance for switch-on shocks to emerge in this case and, hence, only an Euler shock is allowed if any shock runs. Recalling $\hat{c}_{f0} = 1 \geq \hat{c}_{A0} = \hat{c}_{s0}$ and the fact that the flow speed changes from super-acoustic to sub-acoustic across the Euler shocks, the flow speed in front of the Euler shock is super-fast. Therefore the Euler shock belongs to the fast branch in this case and is controlled by $\psi_f^- \geq 0$ through (4.59). Similarly, the ordinary rarefaction is controlled by $\psi_f^- < 0$ since the ordinary rarefactions flow with an acoustic speed. After the ordinary wave, a switch-on slow rarefaction can follow if $\hat{c}_{A1} \leq 1$, where $\hat{c}_{A1}$ stands for the Alfvén speed behind the first wave normalized by the acoustic speed. Since we control the switch-on rarefactions through (4.60), the wave follows only if ψ_s^- is negative. Otherwise, no wave follows and only the ordinary wave runs on the side.

(q): In this case both Euler shocks and switch-on shocks are allowed. Recalling $\hat{c}_{f0} = \hat{c}_{A0} > 1 = \hat{c}_{s0}$, the Euler shock lies in both the fast and slow branches. Note here that we need select either of the switch-on-shock branch or Euler-shock one that is used for the Mach numbers in the overlap region before running the program as mentioned in Sec. 4.5.1. And two wave-patterns are possible as explained below: (q-i) an Euler shock or ordinary rarefaction that is possibly followed by a switch-on rarefaction and (q-ii) a switch-on shock followed by a slow shock or rarefaction wave.

The wave-pattern is determined as follows. If $\psi_f^- > 0$, the first wave is either a switch-on or Euler shock, which is given by ψ_f^- through (4.59). In the case of the Euler shock, there is a chance for a following switch-on rarefaction like the case of (p). Hence, the pattern (q-i) where the flow speed is super-fast in front of the shock is realized. In the case of the switch-on shocks, on the other hand, the pattern (q-ii) is realized. The following slow wave is given by ψ_s^- through (4.60).

If $\psi_f^- \leq 0$, on the other hand, the parameter has no corresponding rarefaction waves now. Hence the first wave is controlled by ψ_s^- through (4.60). $\psi_s^- \leq 0$ gives an ordinary rarefaction and the wave pattern is (q-i). Note that switch-on rarefactions never follow in this case because $\hat{c}_A$ increases across rarefaction waves and $\hat{c}_{A1}$ is necessarily larger than unity. On the other hand, $\psi_s^- > 0$ gives an Euler shock whose flow speed is super-slow and sub-fast. The shock is followed by a switch-on rarefaction if $\hat{c}_{A1} \leq 1$. Since we have already used ψ_s^-, we control the switch-on rarefaction by introducing ψ_{ex}^-. Then the pattern (q-i) where the flow speed is sub-fast and super-slow in front of the shock is realized. Note that the number of the waves is one or two in these cases. See also the flow chart presented in Fig. 4.6.

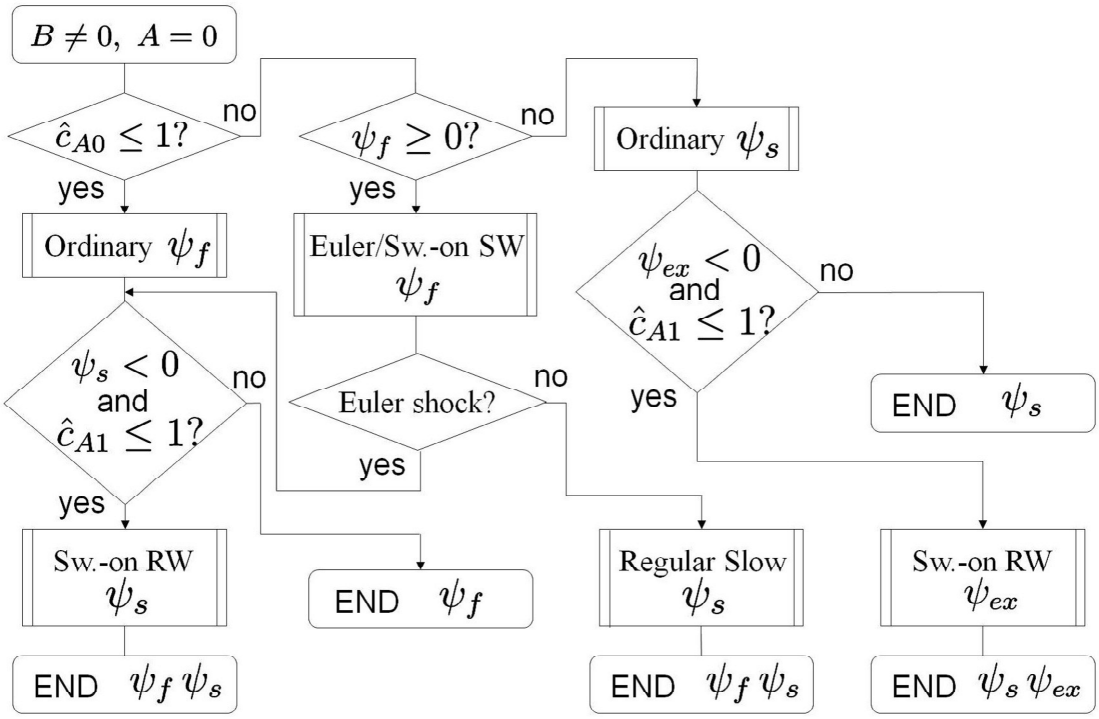

Figure 4.6: The flow chart for arranging the waves when there is no transverse magnetic field initially while the normal magnetic field exists. The function entitled 'Euler/Sw.-on SW' is controlled by ψ_f through (4.59) and gives an ordinary rarefaction wave if $\psi_f < 0$ or Euler or Switch-on shock otherwise. Note here that the switch-on branch is used only when the branch is selected beforehand. The 'Regular Slow' function gives a regular slow shock, controlled by ψ_s through (4.57). The 'Sw.-on RW' function handles a switch-on slow rarefaction which is given through (4.60). The 'Ordinary' function gives an ordinary rarefaction or Euler shock. Here, the function with ψ_f is controlled through (4.59) while that with ψ_s is handled through (4.60) and (4.62) for rarefactions and shocks respectively.

The case without normal magnetic fields

In this case, the structure of solutions is *a priori* known: two fast waves fanning out on both sides of a tangential discontinuity. The fast waves are controlled by $\psi_f^{\mp}$ through (4.59) on the left and right sides respectively. Note that switch-off rarefaction waves do not exist and $s_{\max} = \infty$. The Rankine-Hugoniot conditions for tangential discontinuities require the continuity of the total pressure and normal velocity. Hence, there are always two fast waves and two matching conditions.

4.6 Other technical details

4.6.1 modified Newton-Raphson method

We discuss how to modify the Newton-Raphson method in order to handle the case that the number of the parameters changes in the iteration process. This modification is necessary because the number of the waves in the solution changes due to the intermediate shocks, switch-on/off waves or extra waves as mentioned in the preceding section. Furthermore, since the mappings (4.59) and (4.60) are not injective for switch-off rarefactions and the rotational discontinuities respectively, the differential values of the quantities at the contact discontinuity with respect to ψ_f or ψ_s are zero for such waves and, as a result, the Jacobi matrix becomes singular. Therefore, in order to avoid the singularity, the parameters associated with those waves should be omitted in the Newton-Raphson procedure, i.e., the parameters are not improved but hold their values.

On the other hand, there are always five conditions that should be satisfied at the contact discontinuity provided normal magnetic fields exist. Hence, we need ignore some equations and find the solution of the reduced system and then, as a post process, we check whether the other conditions are satisfied. There seems to be no special strategy for selecting the equations that are omitted although the code is designed so that the equations for the magnitude of the transverse magnetic field, z, y, x-components of the velocity and pressure are omitted in this order when the number of equations is adjusted.

We also note that the number of equations may be reduced when the initial condition is confined in the (x, y)-plane due to the non-existence of the z-components of the velocity and magnetic fields. If none of the waves arranged on both sides cannot produce the z-components, for example, such a case that two fast waves and two slow waves fan out on both sides of the contact discontinuity and a $2 \to 3$ intermediate shock runs in the right side, then the differential values of the differences of v_z and

B_z at the contact discontinuity with respect to any parameter become zero since v_z and B_z are absent throughout the space for any combination of the parameters unless the wave-pattern changes and the rotational discontinuities appear. Therefore these equations associated with z-component should be neglected, otherwise the corresponding rows of the Jacobi matrix lead to the singularity. Accordingly, we also reduce the number of the parameters to three, corresponding to that of the equations, provided there remain more than three parameters. Since there seems to be no general prescription for choosing the parameters that are discarded, our code treats it as a setting parameter, i.e., we should plan which parameters are neglected before running the program.

If the normal magnetic field is absent, on the other hand, these modifications are never necessary because there are always two fast waves, which are not switch-off rarefactions, running in both sides of the tangential discontinuity, where there are just two matching conditions: the continuity of the total pressure and normal velocity. That is, the Jacobian is always a 2×2 matrix and does not become singular.

4.6.2 how to obtain the maximum strength of fast rarefactions

As mentioned repeatedly, the fast rarefaction branches terminate at switch-off rarefactions and there is the maximum strength of the fast rarefaction for the given upstream state provided the normal magnetic field exists. Once the initial condition is given, the maximum strength is known since the state in front of the switch-off rarefaction is the given state. The strength, $s_{\max}$, is given by solving the equation below.

$$\boldsymbol{B}_{t,\mathrm{behind}}(s_{\max}) = \int_0^{s_{\max}} \frac{\boldsymbol{B}_t(s')}{(c_A(s')/c_f(s'))^2 - 1} \mathrm{d}s' = \boldsymbol{0}, \tag{4.63}$$

where we integrate the fast eigenfunction, $\boldsymbol{r}_f$, and pick up the component of the transverse magnetic field. The equation is solved by numerically integrating the integrand and finding the value of s such that the transverse magnetic field is quenched. Then the $s_{\max}$ is used throughout the calculation. Note that the values of $s_{\max}$ on the right and left sides are generally different.

4.6.3 remark on the class of solutions that eludes the search

As mentioned in the footnote in Sec. 4.5.2, there is the class of solutions that the algorithm cannot find unless we discard the intermediate shocks whose upstream flow

speed is greater than the fast speed. More specifically, we may miss the solutions that include $2 \to \star$ intermediate shocks, where '$\star$' stands for '3', '4' or '3, 4', if the initial condition allows the $1 \to \star$ intermediate shocks. For example, suppose that an initial condition whose left state allows the emergence of the $1 \to \star$ intermediate shocks has a solution that includes a left-going $2 \to 4$ intermediate shock whose strength is given by $\psi_s^- = \psi_0 > 0$ through (4.60). And suppose also that we know all the other values of the ψs that parametrize each wave in the solution as well. Then, if we give the parameters as the initial guess and follow naively the flow chart (Fig. 4.5), can we obtain the solution? The answer might be no because, following the flow chart, the first step is inserting a trial intermediate shock with a hope that the fastest wave is a $1 \to \star$ intermediate shock. If the ψ_0 gives a $1 \to \star$ shock in this first step, then we follow the path (b) and there is no chance for the $2 \to 4$ intermediate shock to be considered. To produce the solution that includes the $2 \to 4$ shock, we should reject the first trial intermediate shock. Hence we designed our code so that we can find such hidden solutions by always discarding the first trial intermediate shock. It is a setting parameter whether the first trial intermediate shock is always neglected or not. Trying both the settings, we can find all the solutions.

4.6.4 advantage of including the rotational discontinuity in the slow-shock function

The non-regular-slow-shock function (4.60) includes the rotational discontinuity, as mentioned earlier, which lies at the end point of the slow Hugoniot locus. Owing to this feature, a rotational discontinuity followed by a slow wave can be realized with two ways: the combination of ψ_r and ψ_s, where the parameters give the rotational discontinuity and slow wave through the function of rotational discontinuities (4.58) and the slow-wave function (4.57) respectively, or the pair of ψ_s and ψ_{ex}, where the ψ_s now gives the rotational discontinuity through (4.60) while the ψ_{ex} gives the slow wave through (4.57). Since the degeneracy violates the one-to-one correspondence between the wave parameters and the structure of the solution, this parameterization may seem to be awkward. Thanks to this parameterization, however, the non-regular solutions and regular solution can form a one-parameter family as the $2 \to 3$ intermediate shocks continuously change to the rotational discontinuity. In fact, some initial conditions have uncountably infinite solutions that form a one-parameter family of ψ_s whose end point is the regular solution and smoothly connected to the non-regular solutions that include a $2 \to 3$ intermediate shock instead of the rotational discontinuity. Such examples are shown in the following sections.

4.6.5 the valid range of switch-on shocks

As mentioned in Sec. 4.3.4, switch-on shocks are possible only when the Mach number satisfies the inequality (4.48). Such Mach numbers exist only if $\hat{c}_{A0} := c_{A0}/a_0 = \sqrt{B^2/\gamma} > 1$ as shown below.

(i) In the case of $\sqrt{B^2/\gamma} > 1$. Recalling the degeneracy (4.21), the fast speed equals to the Alfvén speed, i.e., $\hat{c}_{f0} = \hat{c}_{A0} = \sqrt{B^2/\gamma}$. Then,

$$\left(\frac{\gamma+1}{\gamma-1}\frac{B^2}{\gamma} - \frac{2}{\gamma-1}\right) - \hat{c}_{f0}^2 = \frac{2}{\gamma-1}\left(\frac{B^2}{\gamma} - 1\right) > 0, \tag{4.64}$$

and, since $\gamma > 1$, the value in the square root is positive. Therefore there is a finite range in (4.48) where the switch-on shocks are possible.

(ii) $\sqrt{B^2/\gamma} \le 1$. In this case, the fast speed degenerates into the acoustic speed, i.e., $\hat{c}_{f0} = 1$. Then

$$\left(\frac{\gamma+1}{\gamma-1}\frac{B^2}{\gamma} - \frac{2}{\gamma-1}\right) - \hat{c}_{f0}^2 = \frac{\gamma+1}{\gamma-1}\left(\frac{B^2}{\gamma} - 1\right) \le 0. \tag{4.65}$$

Therefore there is no Mach number that satisfies the inequality (4.48) and switch-on shocks are never possible.

4.6.6 the correct root in the cubic equation

We use the cubic equation for $\hat{v}$ (4.45) to obtain the fast shock solution. This equation has three roots in general and hence we should find the correct root. Here, we discuss how to pick it up, which turns out to be easy as shown below.

The point is that we use (4.45) only for fast shocks. Then, since the state in front of the shock is super-fast, the parameter M_0 in (4.45) is always larger than $\hat{c}_{f0}$ when we solve it. Therefore all the roots correspond to some super-fast solution; One is a fast shock and the others, if any, are intermediate shocks whose upstream flow speed is super-fast. We note here that $\hat{v}$ is larger than $B^2/(\gamma M_0^2)$ if we assume that the shock is super-Alfvénic and the transverse magnetic field is not reversed. It is also shown that $\hat{v}$ is smaller than $B^2/(\gamma M_0^2)$ for intermediate shocks. Therefore, the correct root is always larger than the others. Then, we can easily get the fast shock solution by giving an initial guess as $\hat{v} = 1.0$ in the Newton-Raphson method.

4.7 Examples of the exact solutions

In this section, we show some examples of the exact solutions of MHD Riemann problems in order to demonstrate the capability of our code.

Firstly, we present the solutions for a Riemann problem whose initial condition satisfies the Rankine-Hugoniot conditions of a $1 \to 4$ intermediate shock:

$$(\rho_L,\ p_L,\ v_{xL},\ v_{yL},\ v_{zL},\ B_{yL},\ B_{zL}) = (1,\ 1,\ 0,\ 0,\ 0,\ 1,\ 0), \tag{4.66}$$

$$\begin{aligned}&(\rho_R,\ p_R,\ v_{xR},\ v_{yR},\ v_{zR},\ B_{yR},\ B_{zR})\\ &\quad = (2.622826,\ 8.930218,\ -2.196843,\ -1.571584,\ 0,\ -0.8600000,\ 0),\end{aligned} \tag{4.67}$$

with $B_n = 3$ and $\gamma = 5/3$. The discontinuity is initially located at $x = 0$. Some of the solutions at $t = 0.1$ are shown in Fig. 4.7, where we showed the profiles of the density and transverse magnetic field. Note that the transverse magnetic fields are confined in (x, y)-plane in these solutions.

As shown in the figure, the initial condition can be connected not only by a $1 \to 4$ shock (the bottom panels) but also by other wave patterns. The top panels are the regular solution, which consists of a fast shock, 180°-rotational discontinuity and slow shock that run into the left side of the contact discontinuity and a fast and slow rarefaction waves that run on the other side. The second and third rows show some non-regular solutions that contain a $2 \to 3$ intermediate shock instead of the rotational discontinuity, which is responsible for reversing the transverse magnetic field. Although these two solutions resemble each other, the close-ups reveal the difference that the three shock waves change their strengths as well as the fast and slow rarefactions. In fact, we discovered a series of uncountably many solutions that contain a $2 \to 3$ intermediate shock whose strength is different from each other.

The sequence of the infinite solutions is parameterized by the strength of the left-going $2 \to 3$ intermediate shock, i.e., ψ_s^-, and is obtained by gradually changing ψ_s^- that is fixed in the modified Newton-Raphson method. Note that the rotational discontinuity in the regular solution is represented by the terminal point of the slow Hugoniot locus as mentioned in Sec. 4.6.4. As ψ_s^- approaches a certain finite value, the speeds of the left-going fast, slow and $2 \to 3$ shocks come closer to each other while the right-going fast and slow rarefactions weaken their strength. The solution that includes only a $1 \to 4$ intermediate shock corresponds to the limit of the coincidence of the three shock speeds.

The reason why there are uncountably infinite solutions is explained as follows; Since the fields are confined in (x, y)-plane, there are only four non-trivial Rankine-Hugoniot conditions, continuity of p, v_x, v_y, B_y; On the other hand, there are five waves in the solutions as long as a rotational discontinuity or $2 \to 3$ intermediate shock exists; That is, the system is under-determined and hence there remains an extra degree of freedom, which brings the existence of the uncountably many solutions.

As the second example, we present the solutions for an initial condition that is connected by a $1 \to 3$ intermediate shock. The initial discontinuity located at $x = 0$ is given as

$$(\rho_L,\ p_L,\ v_{xL},\ v_{yL},\ v_{zL},\ B_{yL},\ B_{zL}) = (1,\ 1,\ 0,\ 0,\ 0,\ 1,\ 0), \tag{4.68}$$

$$(\rho_R,\ p_R,\ v_{xR},\ v_{yR},\ v_{zR},\ B_{yR},\ B_{zR}) = (2.272607,\ 7.696652,\ -2.106806,\ -2.280515,\ 0,\ -1.8600000,\ 0), \tag{4.69}$$

with $B_n = 3$ and $\gamma = 5/3$. Some of the solutions at $t = 0.1$ are shown in Fig. 4.8, displaying the profiles of the density and transverse magnetic field. We note that the transverse magnetic fields are confined in (x, y)-plane in these solutions.

We again obtained a sequence of the solutions composed by various waves. The top panels show the regular solution that consists of a 180° rotational discontinuity and fast and slow shocks fanning out on the left side of the contact discontinuity and fast and slow rarefactions on the other side. The second and third rows show some non-regular solutions that include a $2 \to 3$ intermediate shock, which reverses the transverse magnetic field instead of the rotational discontinuity. The bottom panels show a non-regular solution that consists of only a $1 \to 3$ intermediate shock. The close-ups reveal the difference of these solutions while we note that the strengths of the rarefactions also differ from each other.

Like the previous example, these solutions form a one-parameter family that is parameterized by ψ_s^-, which controls the left-going slow-family wave. Asymptotically, the fast shock and $2 \to 3$ intermediate shock appear to merge at first while all the three shock speeds are coming closer to each other as ψ_s^- reduces. Although this asymptotic behavior infers the existence of the solutions that include a left-going $1 \to 3$ intermediate shock and slow shock, such a solution is not found. Hence, the solution that includes three shocks jumps to one that is composed of only a $1 \to 3$ shock before the two shocks merge. Considering the reason why there are uncountably infinite solutions, we can interpret this feature naturally. Once a $1 \to 3$ intermediate shock is formed, the under-determination of the system is lost and the system becomes determined. Therefore there is only one solution that includes a $1 \to 3$ intermediate shock (the bottom panels).

As the third example, we pick up an initial condition that is connected by a $2 \to 4$ intermediate shock:

$$(\rho_L,\ p_L,\ v_{xL},\ v_{yL},\ v_{zL},\ B_{yL},\ B_{zL}) = (1,\ 1,\ 0,\ 0,\ 0,\ 1,\ 0), \tag{4.70}$$

$$(\rho_R,\ p_R,\ v_{xR},\ v_{yR},\ v_{zR},\ B_{yR},\ B_{zR}) = (2.593746,\ 7.352303,\ -1.897120,\ -1.068836,\ 0,\ -0.1000000,\ 0), \tag{4.71}$$

with $B_n = 3$ and $\gamma = 5/3$. Some of the solutions at $t = 0$ for the initial discontinuity located at $x = 0$ are presented in Fig. 4.9. Note that the transverse magnetic fields are confined in (x, y)-plane in these solutions.

The top panels show the regular solution that consists of a fast shock, 180° rotational discontinuity and slow shock running in the left side of the contact discontinuity and a fast rarefaction and slow shock running on the other side. The second and third panels present some non-regular solutions that include a $2 \to 3$ intermediate shock, which is responsible for reversing the transverse magnetic field. The solution including a $2 \to 4$ intermediate shock is shown in the bottom panels.

There are also uncountably infinite solutions like the previous examples since these solutions form a one-parameter family parameterized by ψ_s^-. Although all the left-going shocks come closer asymptotically, the $2 \to 3$ shock and slow shock appear to merge before the fast shock and $2 \to 3$ shock converge, which infers the asymptotic solution that includes a fast shock and $2 \to 4$ intermediate shock. However, like the previous example, such a solution is not found. Hence, the solution including three shocks jumps to one that includes only a $2 \to 4$ intermediate shock.

Finally, we give the solutions for an initial condition that is connected by a $2 \to 3$ intermediate shock:

$$(\rho_L,\ p_L,\ v_{xL},\ v_{yL},\ v_{zL},\ B_{yL},\ B_{zL}) = (1,\ 1,\ 0,\ 0,\ 0,\ 1,\ 0), \tag{4.72}$$

$$\begin{aligned}&(\rho_R,\ p_R,\ v_{xR},\ v_{yR},\ v_{zR},\ B_{yR},\ B_{zR})\\ &\quad = (1.159467,\ 1.479053,\ -0.4315320,\ -2.541677,\ 0,\ -1.658269,\ 0),\end{aligned} \tag{4.73}$$

with $B_n = 3$ and $\gamma = 5/3$. Some of the solutions at $t = 0.1$ for the discontinuity located at $x = 0$ are shown in Fig. 4.10. Note that the transverse magnetic fields are confined in (x, y)-plane in these solutions.

The top panels are the regular solution that consists of a 180° rotational discontinuity and fast and slow shocks on the left side of the contact discontinuity and a fast and slow rarefactions on the other side. The second panels present a non-regular solution that includes a $2 \to 3$ intermediate shock instead of the rotational discontinuity, which reverses the transverse magnetic field. The third panels present the non-regular solution that is composed of only a $2 \to 3$ intermediate shock. The bottom ones show a non-regular solution that consists of a fast rarefaction, $2 \to 3$ intermediate shock and slow rarefaction fanning out on the left side of the contact discontinuity and a fast and slow shock on the other side.

Different from the previous examples, these solutions cannot be parameterized by ψ_s^-. Instead, they are parameterized by ψ_s^+ that controls the right-going slow wave. As ψ_s^+ increases, the left-going fast shock in the solutions becomes weaker and changes into a rarefaction wave across the solution that includes only a $2 \to 3$

intermediate shock. As ψ_s^+ increases further, the tail of the fast rarefaction and the $2 \to 3$ intermediate shock come closer to each other, and the fast rarefaction becomes stronger. Therefore we concluded that the solution will reach one that includes a compound wave formed by a left-going $1, 2 \to 3$ intermediate shock attached to a fast rarefaction wave. The solution that includes a compound wave must be an end point of the sequence because the value of ψ_s^+ asymptotically approaches a finite value and appears to converge in the limit and we can find no solution for ψ_s^+ larger than the asymptotic value.

4.8 Analysis of the Brio & Wu problem

In this section, we apply our new code to two specific initial conditions and their neighbors. One of them is first picked up by Brio & Wu (1988) and is known to have a non-regular solution with a compound wave. This is one of the initial conditions in the MHD Riemann problem that are best known to developers of numerical MHD codes. As demonstrated by Andreev et al. (2008) there is also a regular solution to this problem. The puzzle in the literatures is why the former is almost always obtained in the numerical solutions. After confirming the above regular and non-regular solutions by our code, we show that there are actually uncountably many non-regular solutions to this problem. By studying the properties of these solutions as well as exploring the neighboring solutions, we obtain new insights into the problem.

In the second application, we present an initial condition, for which there seems to be no regular solution. In fact the non-regular solution we found is a limit of a sequence of regular solutions and include a switch-off shock wave. We investigate the neighboring solutions in detail and reveal how the solution is approached by various sequences of solutions. The result forces us to rethink the interpretations of the regular waves and switch-off shocks.

4.8.1 Brio & Wu problem

We present here the solutions for the initial condition in the MHD Riemann problem solved numerically by Brio & Wu (1988). The left and right states in the initial condition are given by

$$(\rho_L,\ p_L,\ v_{xL},\ v_{yL},\ v_{zL},\ B_{yL},\ B_{zL}) = (1,\ 1,\ 0,\ 0,\ 0,\ 1,\ 0), \tag{4.74}$$

$$(\rho_R,\ p_R,\ v_{xR},\ v_{yR},\ v_{zR},\ B_{yR},\ B_{zR}) = (0.125,\ 0.1,\ 0,\ 0,\ 0,\ -1,\ 0). \tag{4.75}$$

The normal component of magnetic field is $B_n = 0.75$ and we take for the adiabatic index $\gamma = 5/3$ instead of $\gamma = 2$, the value adopted by Brio & Wu (1988). This

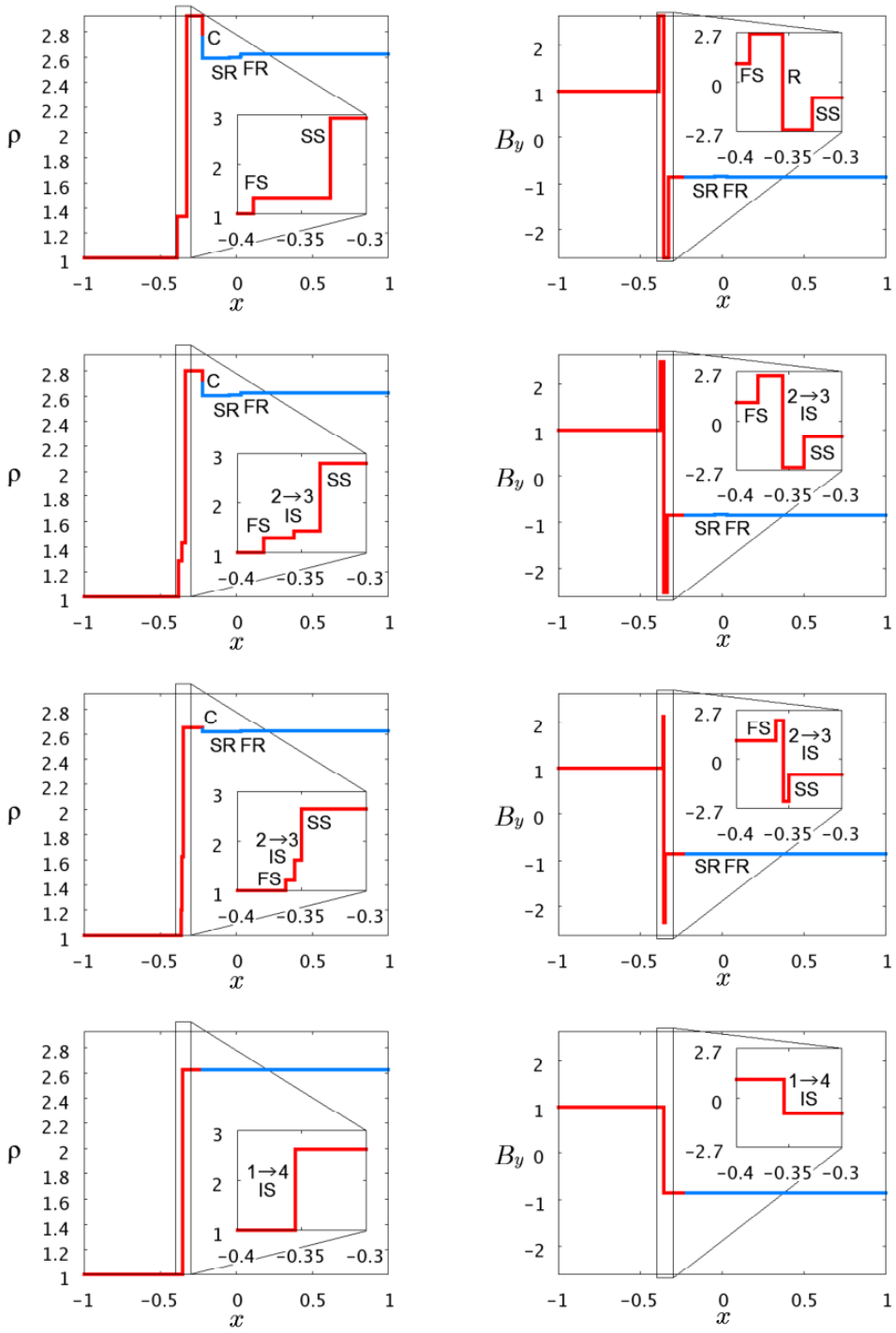

Figure 4.7: The regular solution and some non-regular solutions for an initial condition which can be connected by a $1 \rightarrow 4$ intermediate shock. The waves in the red and blue portions that are separated by the contact discontinuity are left- and right-going respectively. The designations FS, SS, R, FR, SR, C and IS represent the fast shock, slow shock, rotational discontinuity, fast rarefaction, slow rarefaction, contact discontinuity and intermediate shock respectively. The insets are the close-ups of indicated regions.

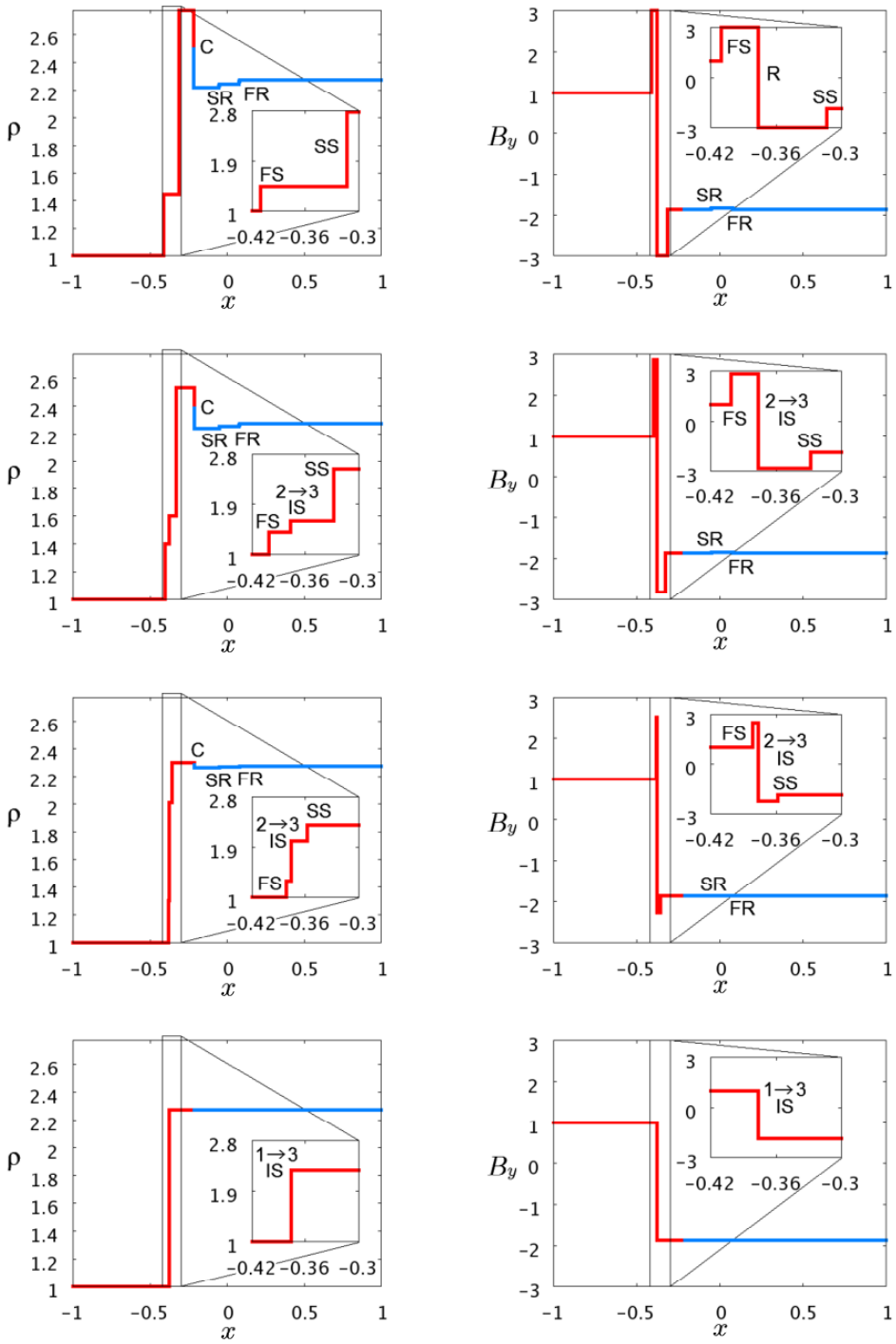

Figure 4.8: The regular solution and some non-regular solutions for an initial condition which can be connected by a $1 \rightarrow 3$ intermediate shock. The notations are the same as in Fig. 4.7.

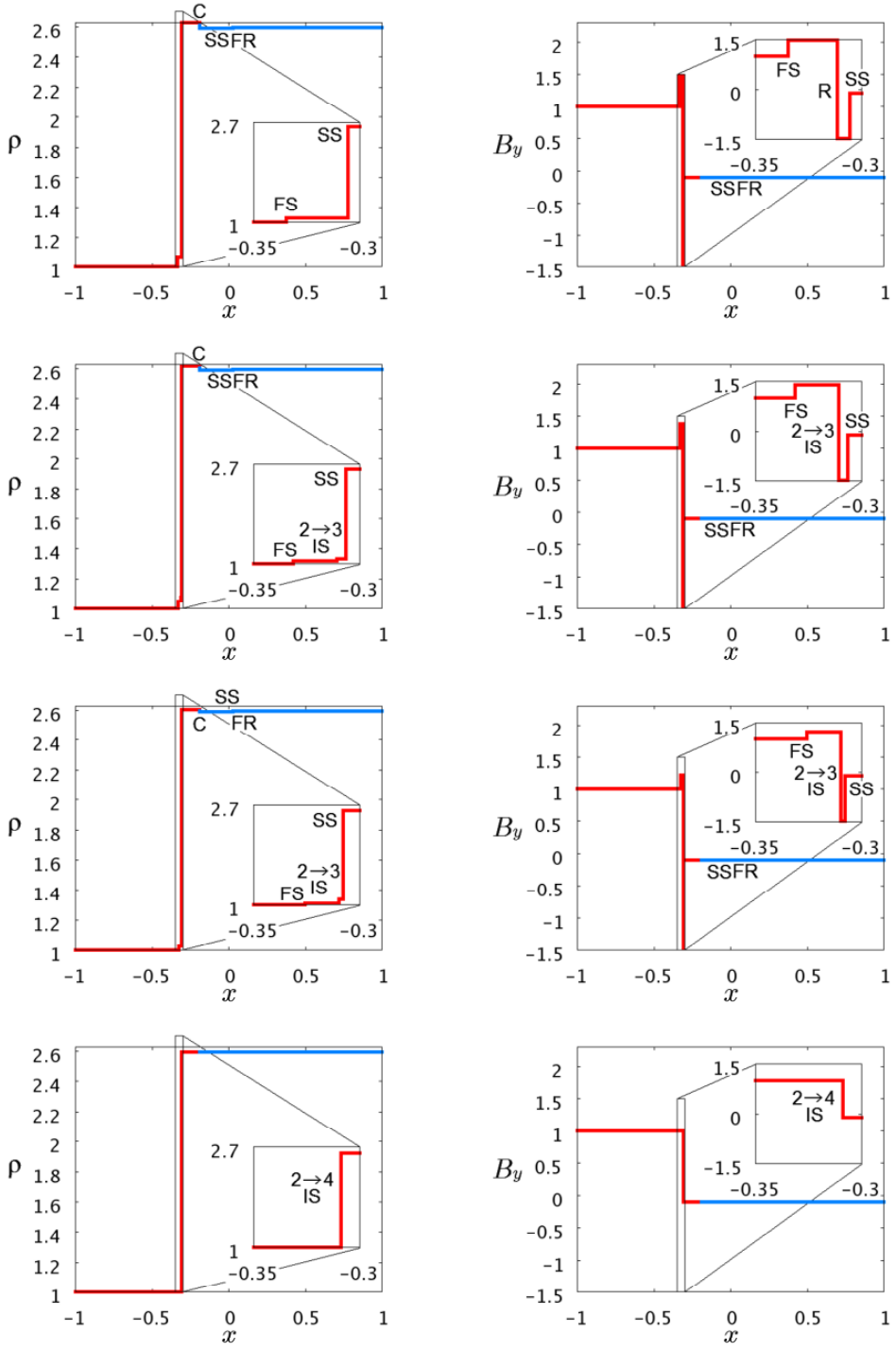

Figure 4.9: The regular solution and some non-regular solutions for an initial condition which can be connected by a $2 \to 4$ intermediate shock. The notations are the same as in Fig. 4.7.

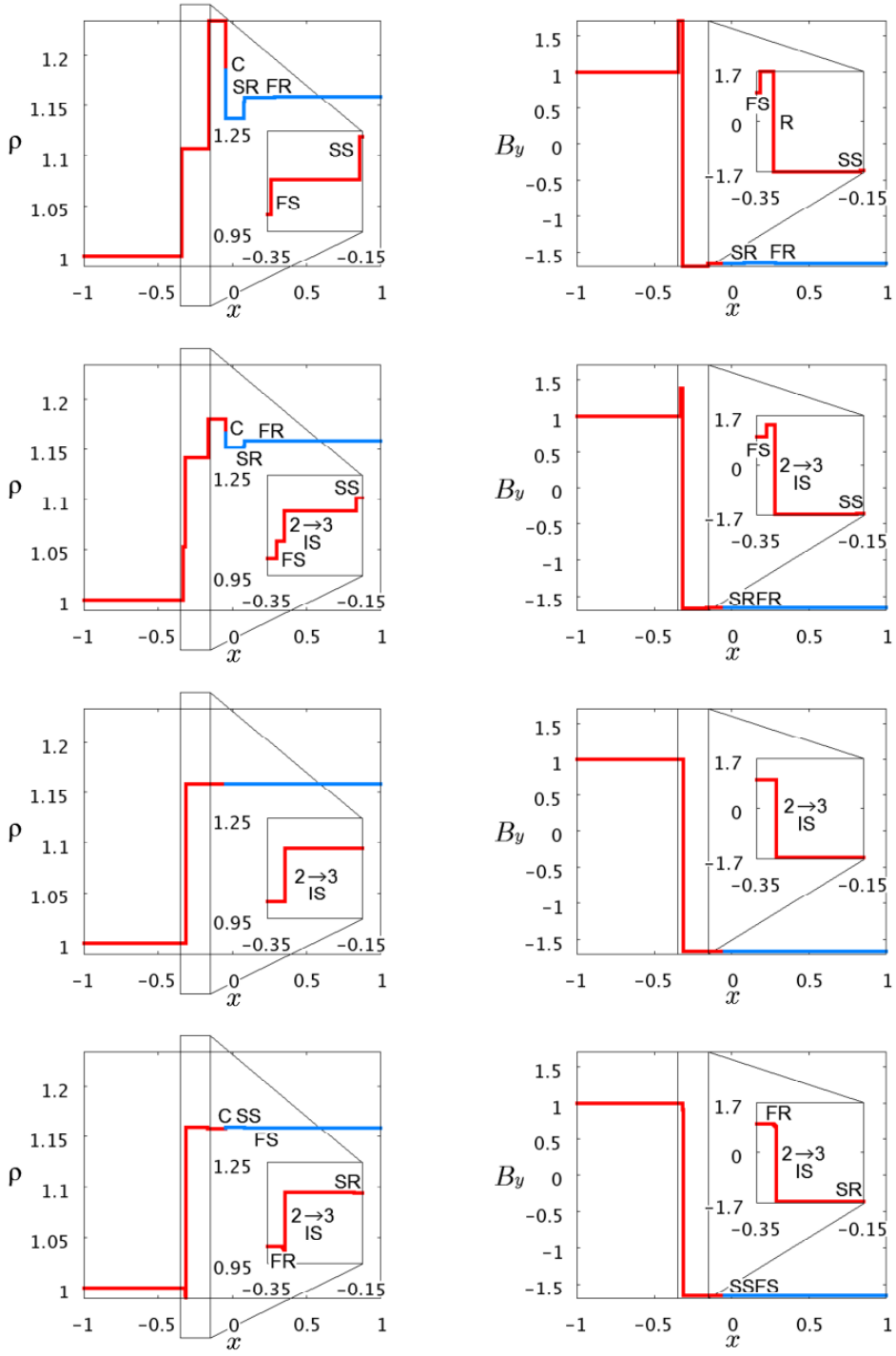

Figure 4.10: The regular solution and some non-regular solutions for an initial condition which can be connected by a $2 \to 3$ intermediate shock. The notations are the same as in Fig. 4.7. In this sequence, the left-going fast shock becomes rarefaction across the solution that consists of only a $2 \to 3$ intermediate shock. The tail of the left-going fast rarefaction and $2 \to 3$ intermediate shock are gradually coming closer, which infers that the end point of this sequence is the solution that includes a left-going $1, 2 \to 3$ intermediate shock attached to a fast rarefaction.

is because the Riemann invariants are singular at $\gamma = 2$ and cannot be used for check. Note, however, that there is no problem to search solutions by our code even in this case. In fact, we confirmed that the solutions are not different qualitatively between $\gamma = 5/3$ and $\gamma = 2$. This is a coplanar problem, for which both regular and non-regular solutions are expected. It is also noted that this can be regarded as a Riemann problem of the reduced MHD system.

We begin with the regular solution. In Fig. 4.11 we show various quantities in the solution at $t = 0.1$. v_z and B_z are identically zero and omitted in the figure. The solution consists of a fast rarefaction wave, rotational discontinuity and slow shock going leftwards and a fast rarefaction wave, slow shock and contact discontinuity running in the right direction in addition to the contact discontinuity. No right-going rotational discontinuity exists because the left-going one has rotated the magnetic field by π radian already. This is the same solution as the one obtained by Andreev et al. (2008).

Next we present a non-regular solution, various quantities in which are displayed at $t = 0.1$ in Fig. 4.12. As is evident, this solution contains a compound wave (denoted by $2 \to 3, 4$ IS and SR in the figure) and is exactly the solution Brio & Wu (1988) obtained in their numerical simulations. The compound wave is a $2 \to 3, 4$ intermediate shock, to which a slow rarefaction wave is attached. Other waves that constitute the solution are a left-going fast rarefaction wave and a contact discontinuity, slow shock and fast rarefaction wave going rightward. Note that the compound wave is responsible for changing the direction of magnetic field. It should be also pointed out that the strengths of the waves other than the compound wave are different between the regular and non-regular solutions.

In addition to these solutions, we found that other non-regular solutions exist, which involve various $2 \to 3$ intermediate shocks. Some of such solutions are shown at $t = 0.1$ in Fig. 4.13. The solution given in the top panel resembles the non-regular solution with the compound wave presented above. A closer look (see the inset), however, reveals a difference: a $2 \to 3$ intermediate shock is closely followed by a slow rarefaction wave but they are detached. The separation of the two waves are more apparent in the middle panel, in which the strengths of the intermediate shock and rarefaction wave are also weaker than in the top panel. In the bottom panel, the solution does not include a slow rarefaction wave but a slow shock instead. The $2 \to 3$ intermediate shock is even weaker in this case. It is noted that the strengths of other waves than the intermediate shock do not change very much. It should be emphasized here that these are solutions to the same initial condition, the Brio & Wu problem.

As a matter of fact, these solutions form a one-parameter family, with the Brio

& Wu solution with the compound wave at one end and the regular solution with a rotational discontinuity at the other end point of the sequence. The parameter that characterizes the solution family is a magnitude of jump in the transverse magnetic field across the $2 \to 3$ intermediate shock. Since the sequence of solutions is obtained by gradually changing this parameter, we can deduce that there are uncountably many solutions like the examples shown in the previous section. As already mentioned, of these non-regular solutions and the unique regular solution it is the Brio & Wu non-regular solution that numerical simulations almost always obtain. From the point of view of the evolutionary conditions, the regular solution is the only solution that contains evolutionary shocks alone. Both $2 \to 3, 4$ and $2 \to 3$ shocks are non-evolutionary. Hence numerical simulations seem to prefer the non-evolutionary solution to the evolutionary solution. This is the original controversy. Now we have added another question: why is the Brio & Wu solution is singled out from the uncountably many non-regular solutions with non-evolutionary shocks?

Since the evolutionary conditions are related with the neighboring solutions, we consider the initial conditions that are close to the original one. Both non-coplanar and coplanar perturbations are discussed in turn separately. As a non-coplanar initial configuration we take the following:

$$(\rho_L,\ p_L,\ v_{xL},\ v_{yL},\ v_{zL},\ B_{yL},\ B_{zL}) = (1,\ 1,\ 0,\ 0,\ 0,\ 1,\ 0), \tag{4.76}$$

$$(\rho_R,\ p_R,\ v_{xR},\ v_{yR},\ v_{zR},\ B_{yR},\ B_{zR}) = (0.125,\ 0.1,\ 0,\ 0,\ 0,\ \cos 3.0,\ \sin 3.0). \tag{4.77}$$

The transverse magnetic field in the right state is rotated slightly with other quantities being unchanged. In accord to the evolutionary condition, we found only a regular solution, which is shown in Fig. 4.14. The solution includes left- and right-going rotational discontinuities, which are responsible for the rotation of magnetic fields. As is evident from the comparison (see Fig. 4.11), this solution is indeed close to the regular solution to the original problem and can be regarded as the perturbed solution. On the other hand, no neighboring non-regular solution exists in this case. Wu (1988b,a) observed in his dissipative MHD simulations, however, a new type of non-coplanar shock-like structures that do not satisfy the Rankine-Hugoniot relations. They concluded that this time-dependent "intermediate shocks" are the neighboring states to the ordinary intermediate shocks. It is noted, however, that the time-dependent non-coplanar structures of these new "intermediate shocks" depend upon the dissipation coefficients as shown in Wu (1988b,a) and his succeeding paper (Wu, 1990) and may not be realized in ideal MHD.

It is of great interest to investigate coplanar perturbations, since the coplanarity is maintained even in numerical simulations unless it is broken explicitly. If the

symmetry is retained indeed, we are essentially dealing with the reduced MHD system, in which the Alfvén characteristics do not exist. It should be noted then that the evolutionary conditions will be modified as pointed out by Falle & Komissarov (2001). For example, the $1 \rightarrow 3$ and $2 \rightarrow 4$ shocks become evolutionary and the rotational discontinuities become non-evolutionary. On the other hand, the $2 \rightarrow 3$ shock remains non-evolutionary with no converging characteristic. It is noteworthy that the $2 \rightarrow 3, 4$ shock is evolutionary, since the slow characteristics are marginally converging and the linear independence of the eigenfunctions of outgoing waves and the initial jumps is recovered. As a consequence of these changes the Brio & Wu solution should be regarded as a regular solution in the reduced system whereas the other solutions with $2 \rightarrow 3$ shocks are still non-regular even in this system. Falle & Komissarov (1997, 2001) claimed that this is the reason why numerical simulations almost always obtain the Brio & Wu solution. The problem may be a bit more complicated, however, as will be demonstrated shortly.

In Fig. 4.15 we present the solutions we found with our code for the following initial condition:

$$(\rho_L,\ p_L,\ v_{xL},\ v_{yL},\ v_{zL},\ B_{yL},\ B_{zL}) = (1,\ 1,\ 0,\ 0,\ 0,\ 1,\ 0), \quad (4.78)$$

$$(\rho_R,\ p_R,\ v_{xR},\ v_{yR},\ v_{zR},\ B_{yR},\ B_{zR}) = (0.125,\ 0.1,\ 0,\ 0,\ 0,\ -0.95,\ 0). \quad (4.79)$$

This time we reduced the transverse magnetic field in the right state slightly, retaining the coplanarity. We then found essentially the same types of solutions as in the original problem: (1) the solution with a rotational discontinuity[7], (2) the solution with the compound wave consisting of a $2 \rightarrow 3, 4$ shock and slow rarefaction wave, and (3) the solutions with a $2 \rightarrow 3$ shock. As mentioned, the second solution is regular and the first and third are now non-regular in the reduced MHD system. The three types of solutions actually form a one-parameter solution family with the first and second solutions being the end points. As shown in Fig. 4.16 this is also the case for the following initial condition:

$$(\rho_L,\ p_L,\ v_{xL},\ v_{yL},\ v_{zL},\ B_{yL},\ B_{zL}) = (1,\ 1,\ 0,\ 0,\ 0,\ 1,\ 0), \quad (4.80)$$

$$(\rho_R,\ p_R,\ v_{xR},\ v_{yR},\ v_{zR},\ B_{yR},\ B_{zR}) = (0.125,\ 0.1,\ 0,\ 0,\ 0,\ -1.05,\ 0), \quad (4.81)$$

in which the transverse magnetic field in the right state is slightly amplified.

These results show clearly that the Brio & Wu solution, or the 'regular' solution with the compound wave, has a unique neighboring solution of the same type

[7]The rotational discontinuity may be an inappropriate term in the reduced system, in which the Alfvén characteristic ceases to exist. We use it, however, to make clear the correspondence to the full system.

as expected from the evolutionary conditions in the reduced system. In the case of the 'non-regular' solutions either with the $2 \to 3$ shock or with the rotational discontinuity, however, the perturbed solutions are not uniquely determined, since there are too many outgoing characteristics. And the existence of uncountably many non-regular solutions is a manifestation of this under-determination. Unlike the over-determination and, as a consequence, the non-existence of neighboring solution, the meaning of the non-uniqueness of perturbed solutions is rather obscure. The results of numerical simulations indicate, however, the evolutionary conditions in the reduced system appear to work in selecting the solution.

4.8.2 an initial condition with no regular solution

In the continuous modifications of the Brio & Wu problem, we ran into an interesting initial condition, for which there seems to be no regular solution. This initial condition is truly a special point unlike the Brio & Wu problem. In fact, the regular and non-regular solutions of the Brio & Wu problem are shared by the neighboring coplanar initial conditions as demonstrated above. This is not the case for the problem considered here.

The initial condition is given by the following:

$$(\rho_L,\ p_L,\ v_{xL},\ v_{yL},\ v_{zL},\ B_{yL},\ B_{zL}) = (1,\ 1,\ 0,\ 0,\ 0,\ 1,\ 0), \tag{4.82}$$

$$(\rho_R,\ p_R,\ v_{xR},\ v_{yR},\ v_{zR},\ B_{yR},\ B_{zR}) = (0.125,\ 0.1,\ 0,\ 0,\ 0,\ -0.329875,\ 0), \tag{4.83}$$

in addition to $B_n = 0.75$ and $\gamma = 5/3$. This differs from the Brio & Wu problem only on the magnitude of the transverse magnetic field ($-B_{yR} = B_{\rm crit} = 0.329875$) of the right state[8]. This is again a coplanar configuration. The only solution our code obtained is a non-regular solution, which is presented in Fig. 4.17 at $t = 0.1$. Note that v_z and B_z are identically zero in this solution.

As can be seen, the solution consists of a fast rarefaction wave and switch-off shock, both of which go leftward, and a switch-off rarefaction wave and Euler shock, which proceed rightward, as well as a contact discontinuity. Although it may seem that the shocks and rarefaction waves form compound waves on both sides of the contact discontinuity, they are actually detached. As a matter of fact, it is theoretically shown that the switch-off waves, irrespective of shock or rarefaction, never form compound waves. As mentioned earlier, the switch-off shock is a $2, 3 \to 4$ shock, with

[8]The ratio of the specific heats is not set to 2, the value adopted by Brio & Wu (1988), but to 5/3 for the same reason as given for the first case.

the Alfvén speed being equal to the upstream flow speed. Preceded by the switch-off rarefaction, which is actually one of the fast rarefaction waves, the fast speed and Alfvén speed are degenerate ahead of the Euler shock, which is itself an evolutionary shock not only in the full system but also in the reduced MHD system in this case although it is possible to be non-evolutionary in principle as mentioned in Sec. 4.3.4. It is normally impossible to prove the non-existence of particular solutions by numerical computations. We think, however, that no regular solution exists indeed to the current problem. In order to demonstrate why we think so and elucidate the special place that the current initial condition occupies, we study the neighborhood of this problem in detail.

Presented in Fig. 4.18 are the solutions to coplanar neighboring problems. More specifically, we vary the strength of the transverse magnetic field of the right state, B_{yR}. The critical value $B_{\rm crit}$ is approached both from above and below. We are concerned here only with the regular solutions. As shown in the figures, in the case of $|B_{yR}| > B_{\rm crit}$ the solutions consist of a fast rarefaction wave, rotational discontinuity and slow shock going leftward and a fast rarefaction wave and slow shock going to the right in addition to a contact discontinuity. As the initial strength of the transverse magnetic field in the right state becomes smaller, the left-going rotational discontinuity and slow shock come closer to each other. Among the right-going waves, the fast rarefaction wave approaches the slow shock. At the critical point the left-going rotational discontinuity and slow shock merge into the switch-off shock and the right-going fast rarefaction wave and slow shock become the switch-off rarefaction wave and the Euler shock respectively.

As the initial strength of the transverse magnetic field becomes even smaller and $|B_{yR}| < B_{\rm crit}$ is satisfied, the right-going rotational discontinuity emerges and is responsible for the inversion of the transverse magnetic field. The Euler shock is replaced by the rotational discontinuity and a slow shock whereas the switch-off rarefaction is modified to an ordinary fast rarefaction wave again at first as long as $|B_{yR}|$ is not very different from $B_{\rm crit}$. A fast shock appears instead of the fast rarefaction wave when $|B_{yR}|$ becomes smaller than a certain value. On the left side of the contact discontinuity, on the other hand, the switch-off shock is changed to an ordinary slow shock and no rotational discontinuity exists. It is stressed that the unique non-regular solution at the critical point is connected continuously to the sequences of the regular solutions obtained for $|B_{yR}| > B_{\rm crit}$ and $|B_{yR}| < B_{\rm crit}$ respectively.

Next we turn to non-coplanar neighboring problems. This time we change the direction of the initial transverse magnetic field in the right state, keeping its strength at the critical value $B_{tR} = B_{\rm crit}$. In this case we always found regular solutions alone,

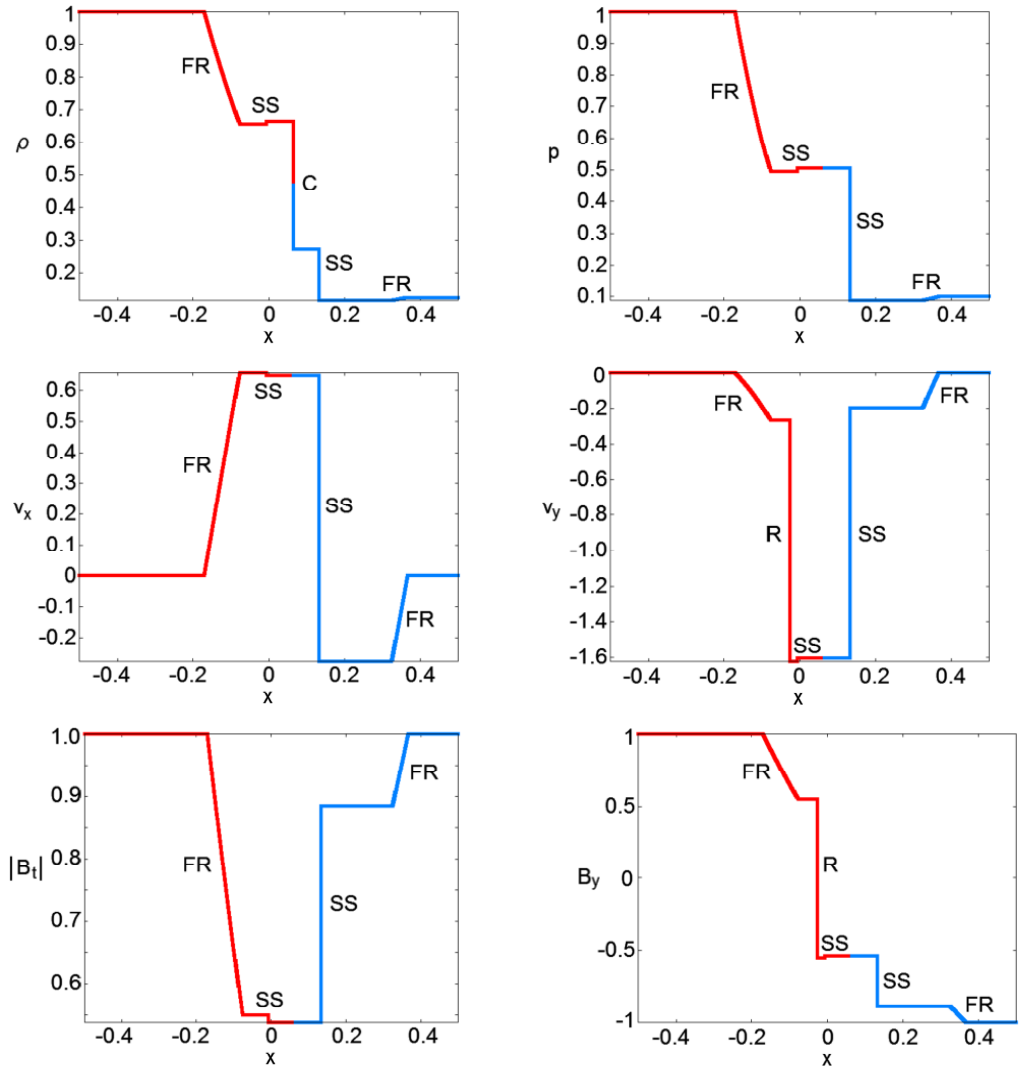

Figure 4.11: The regular solution for the Brio & Wu (1988) problem. The designations are the same as in Fig. 4.7.

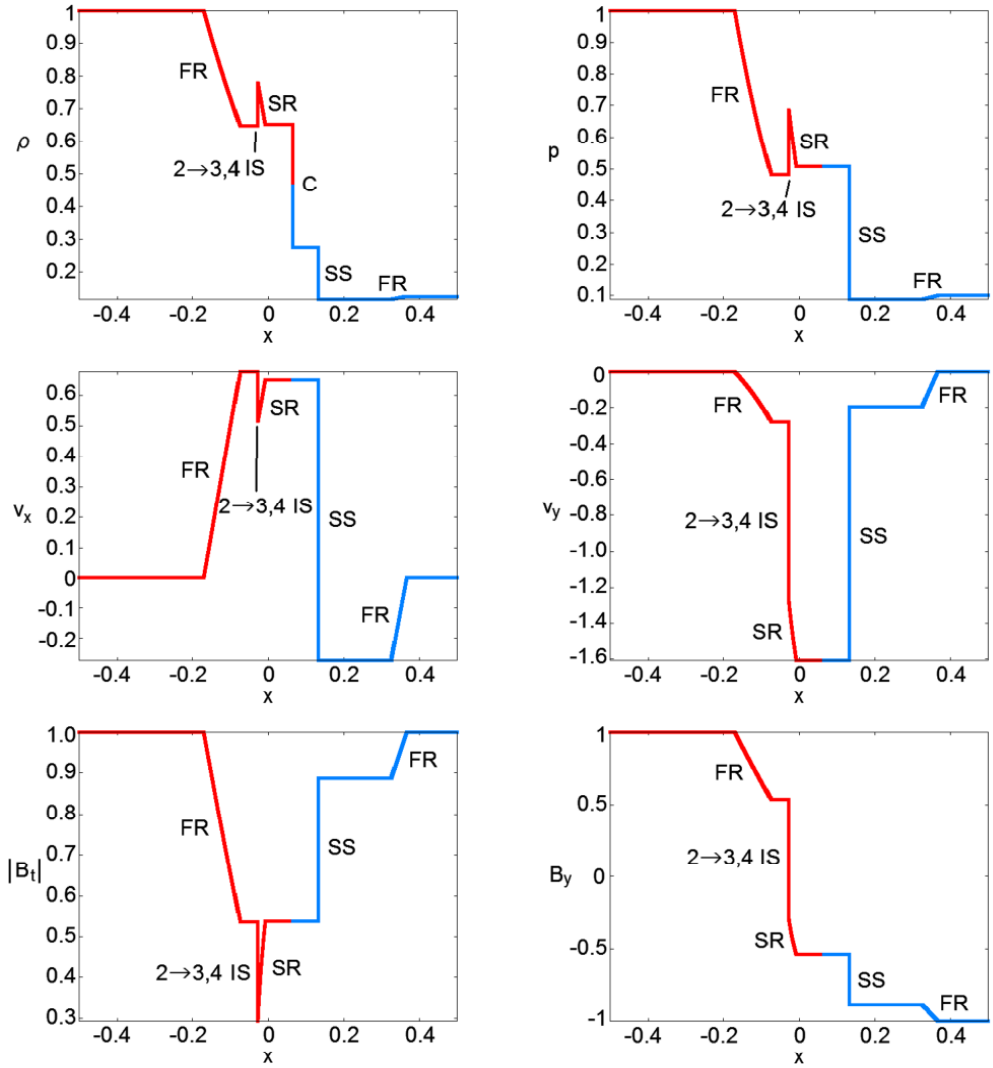

Figure 4.12: The non-regular solution for the Brio & Wu problem that contains a compound wave. The notation is the same as in Fig. 4.7.

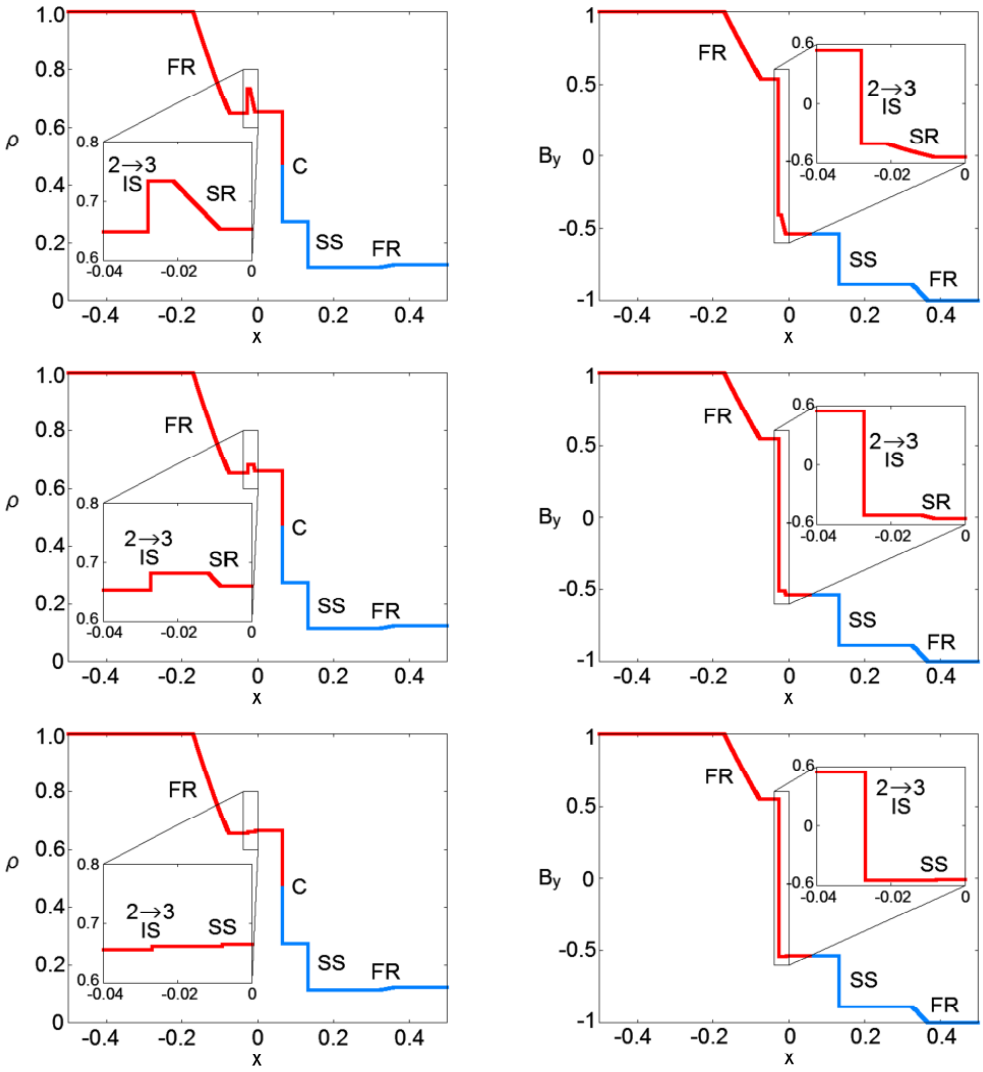

Figure 4.13: Some of the uncountably many non-regular solutions for the Brio & Wu problem that contain a $2 \to 3$ intermediate shock. The notation is the same as in Fig. 4.7. The insets are the close-ups of indicated regions.

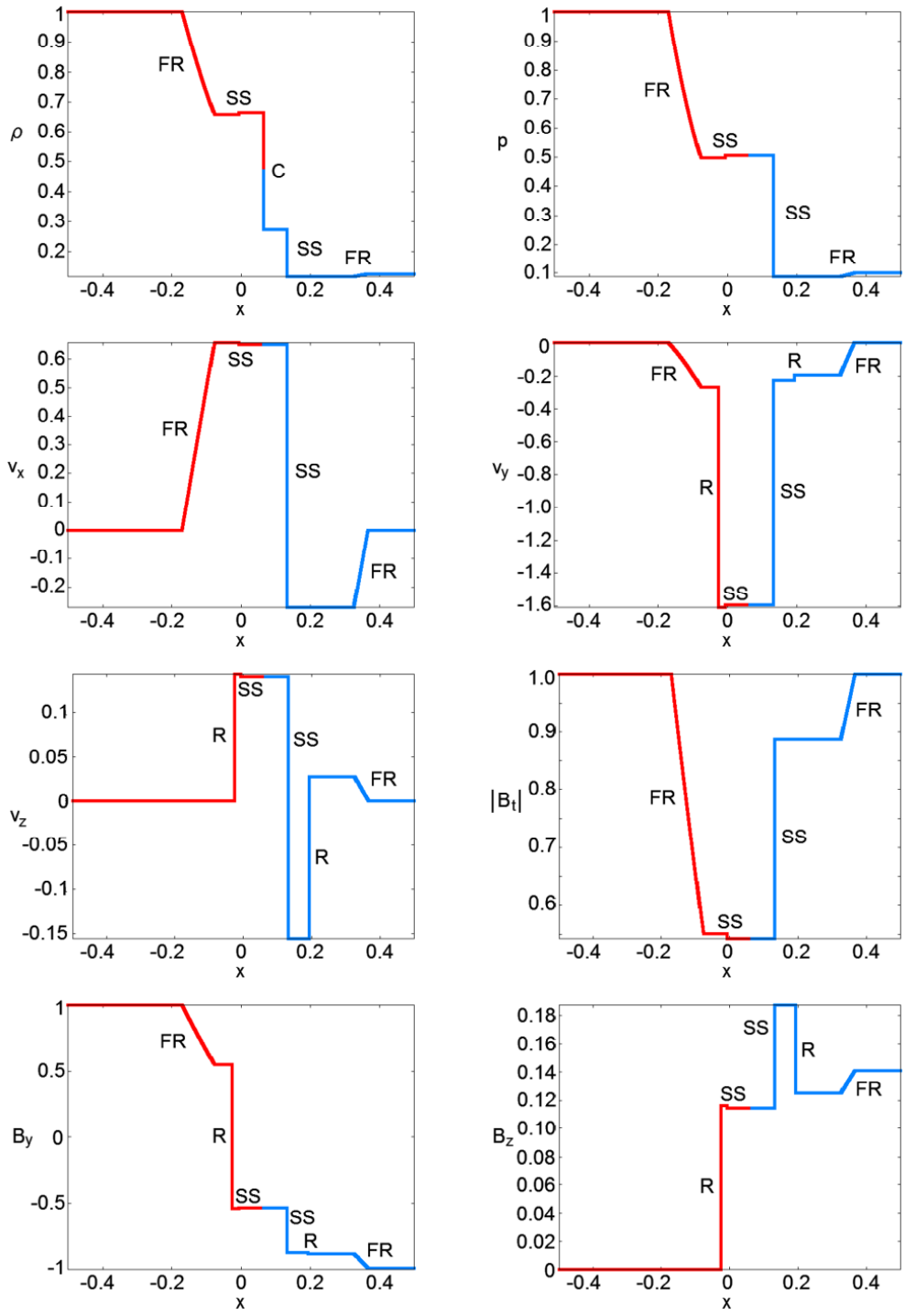

Figure 4.14: A non-coplanar neighboring solutions to the Brio & Wu problem. The initial magnitude of the transverse magnetic field of the right state is the same as the original value. The notation is the same as in Fig. 4.7.

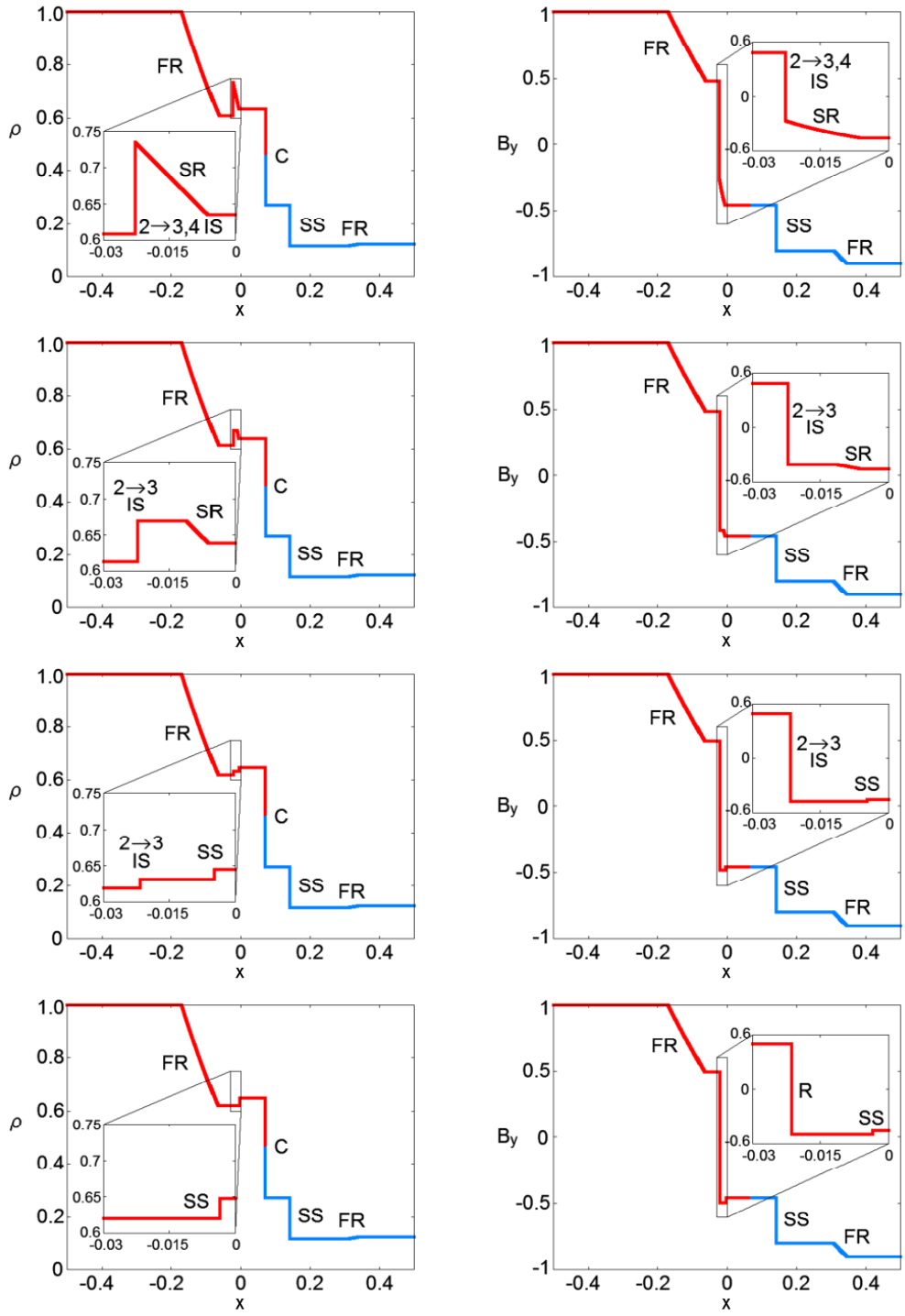

Figure 4.15: Some coplanar neighboring solutions to the Brio & Wu problem. The initial magnitude of the transverse magnetic field of the right state is reduced from the original value. The notation is the same as in Fig. 4.7. The insets are the close-ups of indicated regions.

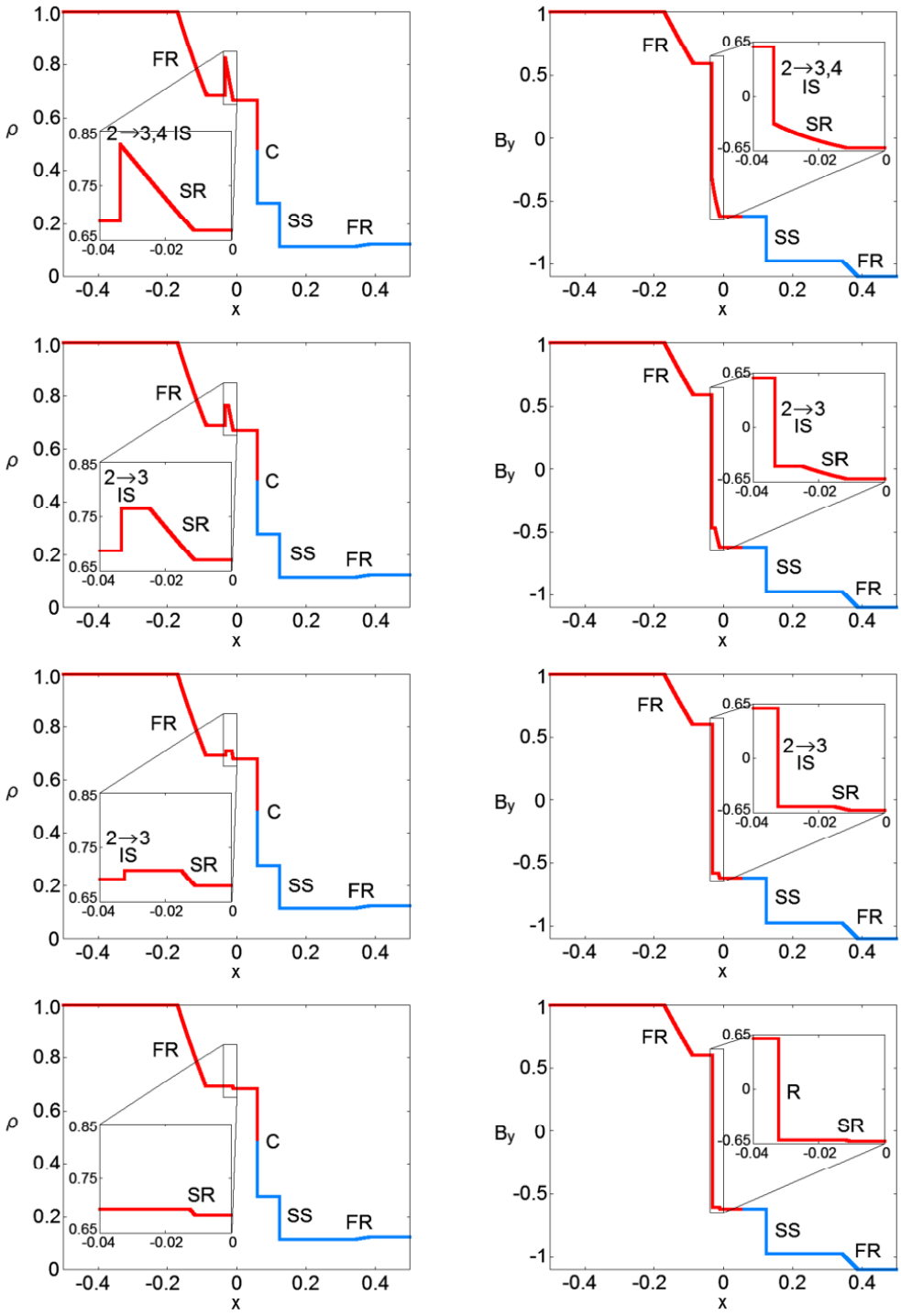

Figure 4.16: Some coplanar neighboring solutions to the Brio & Wu problem. The initial magnitude of the transverse magnetic field of the right state is increased from the original value. The notation is the same as in Fig. 4.7. The insets are the close-ups of indicated regions.

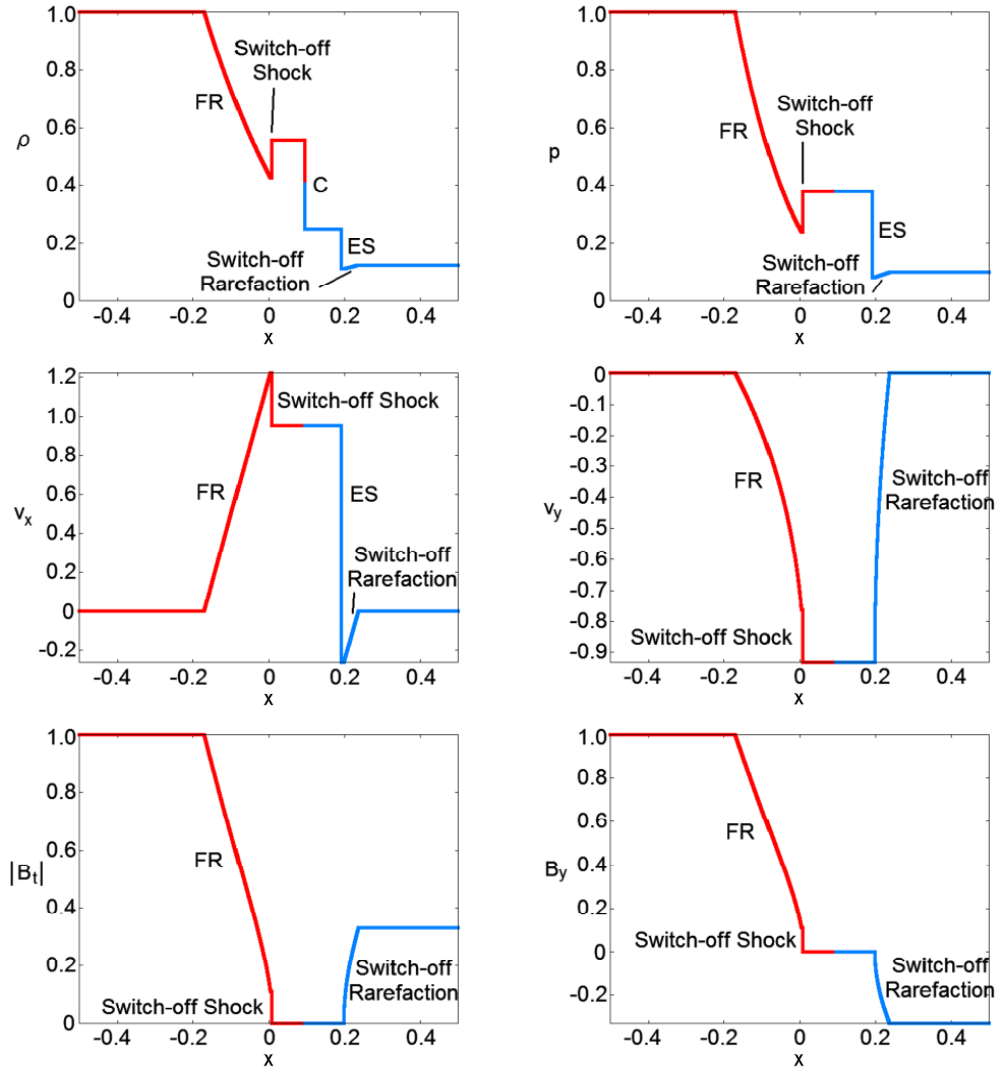

Figure 4.17: The non-regular solution with both a switch-off shock and switch-off rarefaction wave. The notation is the same as in Fig. 4.12 except for the designation ES, which stands for the Euler shock. The initial condition is the same as for the Brio & Wu problem except for the strength of the transverse magnetic field of the right state. See §4.8.2 of the main body for the precise value.

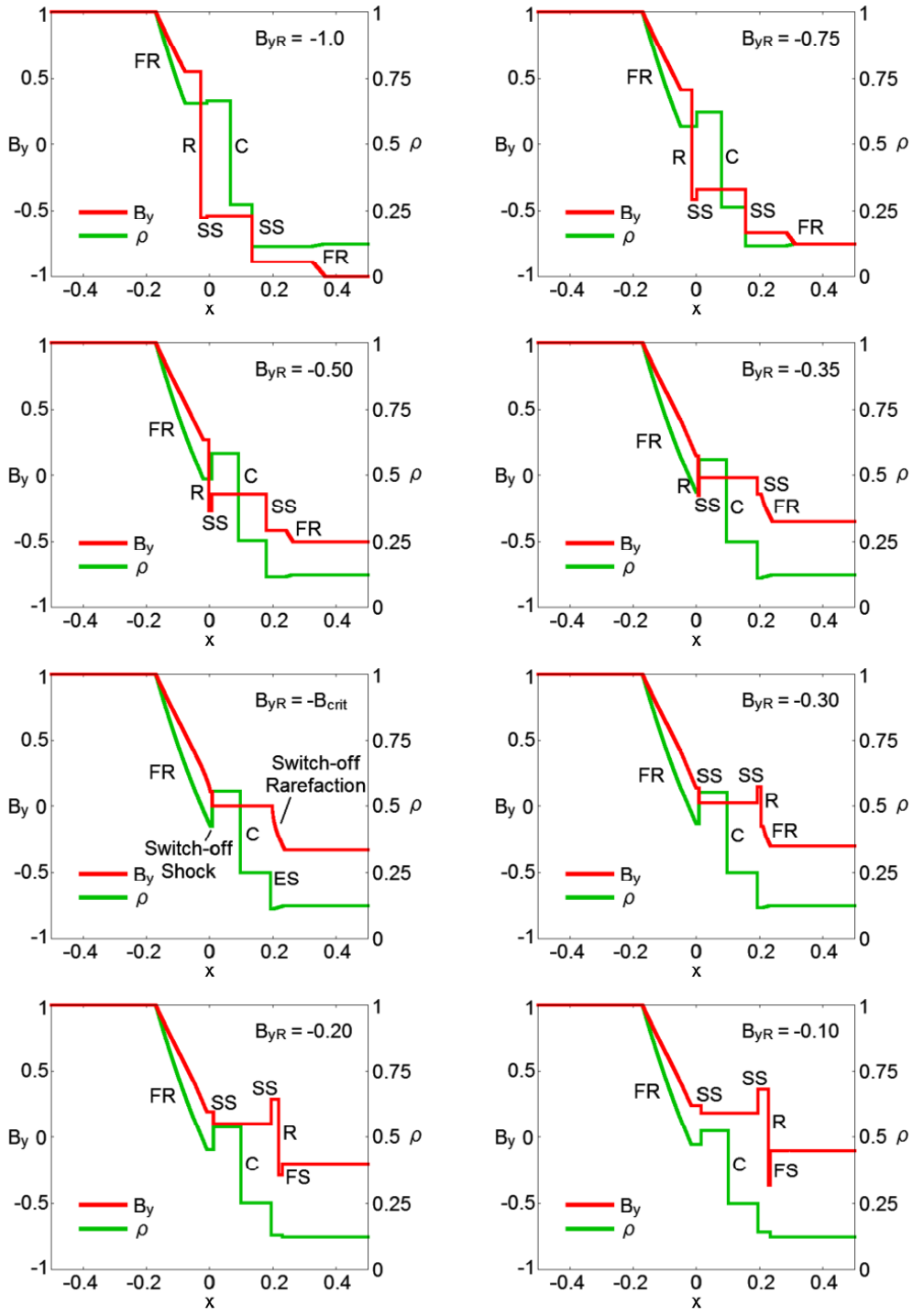

Figure 4.18: Coplanar neighboring solutions to the solution presented in Fig. 4.17. The red line represents the transverse magnetic field whereas the green line displa

varied. See §4.8.2 of the main body for details.

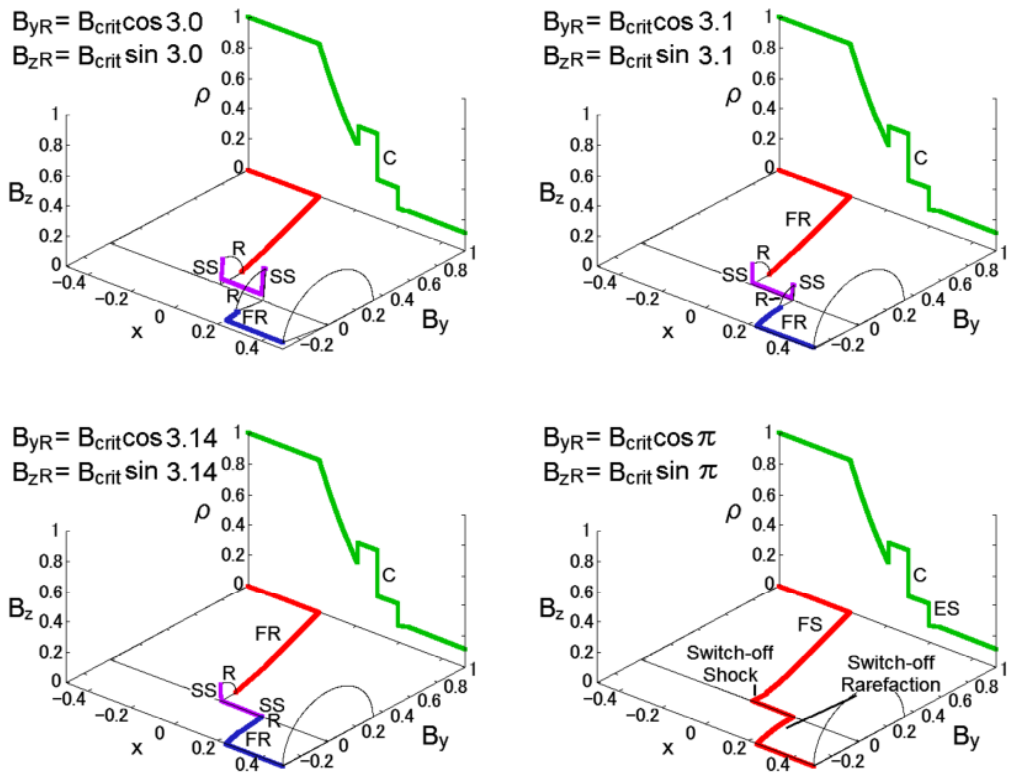

Figure 4.19: Non-coplanar neighboring solutions to the solution presented in Fig. 4.17 as well as in the bottom right panel in this figure. The green line displays the density whereas the red, purple and blue lines represent the transverse magnetic fields, each on a different plane, the angle of which is shown by an arc. Only the direction of the initial transverse magnetic field of the right state is varied in these computations. See §4.8.2 of the main body for details.

which are displayed in Fig. 4.19. As is evident, there appear left- and right-going rotational discontinuities when the transverse magnetic fields are misaligned initially. They are preceded by a fast rarefaction wave and followed by a slow shock running in each direction. As the misalignment gets smaller, or the critical point is approached, the amplitudes of the transverse magnetic fields rotated by these rotational discontinuities become smaller. And they disappear at the critical point and we recover the solution including the switch-off shock and rarefaction wave presented above. Again this clearly demonstrates that the non-regular solution at the critical point is a limit of the sequence of the regular solutions. Put another way, there are only regular solutions in the sufficiently close vicinity of the non-regular solution at the critical point. This is the main reason why we think that there is no regular solution at the critical point. Note, however, that there might be another regular solution that are not included in the neighborhood and eluded our search.

It is interesting to see how a coplanar neighboring solution is approached by non-coplanar solutions. Note that they are both regular solutions. As observed above, the left- and right-going rotational discontinuities cooperate to rotate the transverse magnetic field by the angle imposed by the initial condition. It is found that it is always the right-going rotational discontinuity that rotates the transverse magnetic field by a larger angle if $0 < B_{tR} < B_{\rm crit}$ and vice versa. As the misalignment becomes smaller and the coplanar configuration is approached, one of the rotational discontinuities that gives a smaller rotation gets weaker and disappears for the coplanar configuration. For a non-vanishing but very small misalignment, the relative amplitude of the two rotational discontinuities as a function of B_{tR} changes very rapidly near $B_{tR} = B_{\rm crit}$. In this sense the non-coplanar solutions shown in Fig. 4.19 for $B_{tR} = B_{\rm crit}$ are rather special themselves.

4.9 Summary

In this chapter, we presented an exact Riemann solver that can handle the intermediate shocks and switch-on/off waves. Our solver can treat any initial condition even when the normal or transverse magnetic field is absent. These features are realized for the first time since previous studies discarded these non-regular shocks or initial conditions with vanishing magnetic field. Referring the strategy that is proposed by Torrilhon (2002), we drastically improved it to handle all types of non-regular shocks and switch-on/off rarefactions and the details of the techniques are released for the first time. Since the types of waves generated and their order are not known *a priori* in MHD Riemann problems once such non-regular waves are considered, we developed the method that can arrange the waves in all possible patterns and search

the structure of the solution automatically. Due to the variability of the number of the generated waves, we modified the Newton-Raphson method to adjust the number of the independent variables and equations. Thanks to these techniques, all the solutions are found for a given initial condition, which has never been achieved by other authors (e.g. Andreev et al., 2008). Our method works well indeed as shown in Secs. 4.7 and 4.8, where we presented some examples of the exact solutions, which include the regular and non-regular ones. As demonstrated, our solver can investigate the structure of the solution space in detail. The code will be useful not only for the study of various solutions as demonstrated but also for numerical simulations, in which our solver will provide the exact solutions to be compared with and may be implemented to evaluate numerical fluxes. We also note that since our method is based on the Newton-Raphson method, there might be a solution that exists far away from the sequence of the solutions and hence eludes our search. Hence some strategy that finds such a particular solution may be desired.

We have applied the new code to the Brio & Wu problem, which we believe is useful for the consideration of which weak solutions are really physical, the problem with a long history of controversy. The problem is one of the best known problems for developers of MHD codes. This particular problem has been frequently utilized for the validation of newly developed numerical codes partly because it has a coplanar configuration and 2-dimensional codes can be applied. It has been also known for a long time that numerical solutions always involve the compound wave, which is a $2 \to 3, 4$ intermediate shock, to which a slow rarefaction wave is attached. This is a non-regular solutions, in which the compound wave does not satisfy the evolutionary condition and its reality has been a subject of debate. There are two competing arguments so far. Wu and his collaborators (Wu, 1987; Brio & Wu, 1988; Wu, 1988b,a, 1990; Wu & Kennel, 1992) insist that the intermediate shocks are stable and it is the evolutionary conditions to blame. On the other hand, Falle & Komissarov (Falle & Komissarov, 1997, 2001) claim that the existence of intermediate shocks in numerical solutions are due to the coplanarity, which is inherent in the intermediate shocks. Unless the symmetry is broken somehow, the solution will retain the symmetry (coplanarity or planarity) and, as a consequence, we are dealing with the reduced MHD system. Then the point is that the $2 \to 3, 4$ intermediate shock that comprises the compound wave in the numerical solution of the Brio & Wu problem becomes regular whereas the regular solution that contains rotational discontinuities, which was shown to exist by Andreev et al. (2008) and has been also confirmed in this paper, is now non-regular in the reduced MHD system.

It seems that the existence of the uncountably many other solutions that are non-regular both in the full and reduced systems supports the claim by Falle &

Komissarov (Falle & Komissarov, 1997, 2001), since they have never been realized in numerical simulations. It is intriguing to point out, however, that these solutions do not satisfy the evolutionary conditions not because the number of outgoing characteristics is wrong but because the requirement on the linear independence is not met. This implies that there exit too many neighboring solutions to these non-regular solutions and we cannot single out a physically relevant one. This under-determinacy is certainly different from the over-determinacy that we commonly find for non-evolutionary shocks and needs further investigations. It should be also mentioned that some authors (Hada, 1994; Markovskii, 1998; Inoue & Inutsuka, 2007) insist that eventually all intermediate shocks satisfy the evolutionary conditions if dissipations are taken into account. Although this may explain the realization of the compound wave in the solution of the Brio & Wu problem, it remains to be addressed why other non-regular solutions that are also evolutionary in their analyses but are not produced numerically. They may be linearly unstable. Further investigations are certainly needed.

In the second application we have picked up the initial condition, which appears to possess no regular solution. This initial condition was found by continuously modifying the original Brio & Wu problem in various ways. In fact, the initial magnetic field has a coplanar configuration and is obtained from that in the Brio & Wu problem by reducing the strength of the transverse magnetic field in the right state. We have obtained two sequences of regular solutions as we approach this initial condition from both directions, keeping the coplanarity. They are continuously connected at this point by the non-regular solution, which includes both the switch-off shock and rarefaction waves. The switch-off shock is non-regular and is located at the boundary between the regular slow shocks and intermediate shocks on the slow locus. It is true that we cannot prove the non-existence of regular solutions by these numerical calculations but the fact that all the neighboring regular solutions, coplanar or non-coplanar, are terminated at this non-regular solution suggests strongly that regular solution is unlikely to exist. We are certainly interested in if this non-regular solution is what is realized indeed for this initial condition. This will be a difficult task for numerical simulations, however, since the initial condition has to be prepared precisely.

This initial condition is singular also in the following sense. As the coplanar configurations with $|B_{yR}| > B_{\rm crit}$ approach this critical initial condition, the rotational discontinuity is always left-going whereas the right-going one emerges in the opposite case, $|B_{yR}| < B_{\rm crit}$, and at the critical condition these rotational discontinuities disappear and the switch-off shock and rarefaction wave occur; if the initial transverse magnetic fields are misaligned slightly, then the sequence of the regular solutions

exhibits a rapid and drastic change of the configuration in the vicinity of the critical initial condition: the left- and right-going rotational discontinuities exchange their roles. Such sudden changes of configuration may have a ramification for the stability of the regular solution for the non-coplanar initial configurations with $B_{tR} \approx B_{\rm crit}$.

After all, it seems that the stability of various intermediate shocks needs major reanalysis. The conventional evolutionary conditions are certainly unsatisfactory. Maybe the introduction of dissipations and its zero limits should be scrutinized. In so doing our new code will be useful to generate all possible solutions. We believe that the survey and investigation of other initial conditions and the corresponding solutions, which manifest some singularities, will provide us with new insights and eventually a clue to the understanding of which solutions are physically relevant.

Chapter 5

Summary and Conclusion

In this thesis, we treated the shock dynamics in CCSNe, which is one of the central issues in the field of supernovae. We focused on the two topics: The first topic is the non-spherical structures of progenitors of CCSNe, which have been reported by a series of paper by Arnett, and their effects on the shock dynamics; The other is the physical relevance of the so-called intermediate shocks in MHD.

In the first topic, we performed two linear analyses step by step. At first, we started from the analysis of the evolution of the perturbations that arise in the convective outer layer of a progenitor. As a result, we found that they grow sufficiently during the infall onto the stagnant shock wave. We also found the amplification factors are larger as the scale of fluctuations become smaller. Moreover, we showed that they oscillate at the shock radius with frequencies that are observed in SASI simulations. These results may suggest the possibility that the fluctuations in upstream flows can affect the SASI activity.

As the second step, we performed another linear analysis, in which we studied the effects of such amplified perturbations on the SASI activity. The problem is reduced to an eigenvalue problem and it is solved with the use of the Laplace transform as in the first analysis. Employing some different background flows and inner boundary conditions, we discuss the effect of external perturbations. The results show, however, that the fluctuated upstream flows do not affect the unstable modes of SASI in general. The sharp contrast to the results of the previous numerical simulations by Müller & Janka (2014); Couch & Ott (2013, 2014), who reported that the fluctuations facilitate shock revival, may suggest that the importance of non-linear effects of sufficiently amplified non-spherical perturbations in front of the shock. We also argued that the most unstable modes of SASI that we found seem to be driven by the purely-acoustic cycle, which is opposite to the results of the previous linear analysis.

We do not conclude, however, that the purely-acoustic cycle is the mechanism of SASI because we have not investigated the radial distributions of the modes and we might miss something important. Further investigations must be performed in order to make a robust conclusion in the future.

As the second topic, we treated the physics of MHD shock waves. Especially, we considered the physical relevance of the intermediate shocks, which are commonly observed in MHD simulations. We tackled the problem by studying the solutions of MHD Riemann problems, which are one of the fundamental problems of hyperbolic systems. For this purpose, we developed a new MHD Riemann solver that handles all types of intermediate shocks and other non-regular waves. Applying the code to Brio & Wu problems and its neighboring initial conditions, we obtained uncountably many solutions that include intermediate shocks. This result casts a new question on the relevance of the intermediate shocks: how can we single out the physical solution from uncountably many candidates. We also found an initial condition, where no regular solution exists without switch-on/off waves and the neighboring solutions suddenly change their configurations, which may have a ramification for the stability of the solutions. Anyway, the conventional arguments about evolutionary conditions are certainly unsatisfactory and some new insights seem to be necessary to understand MHD shock waves.

Both of the results are important since they are strongly coupled with the physics in CCSNe. We also note that these findings become a basis when we interpret the outcomes of numerical simulations. We believe that these studies will make much contribution to the elucidation of the mechanism of CCSNe, which is one of the main challenges in the field of physics.

Acknowledgment

First of all, I would like to greatly appreciate my supervisor, Prof. Yamada. He is willing to have a discussion whenever I asked him and he always enlightened me with his patient and earnest attitude continuously since I joined the laboratory. I also learned a lot from his sophisticated professional manner of research, which will continue to guide and help me in the future. I shall be also profoundly grateful for his encouragement when I challenged to attend an international conference in Europe. Thanks to his letter of introduction as well as his financial support to the trip, I was able to visit MPA, which must be the greatest experience in my research life. Without his continuous supports, I could have never carried out my researches.

I would like to acknowledge my collaborator, Dr. Yamamoto. He gladly gave me his set of routines that includes a sophisticated EoS, which significantly contributed to this thesis. His huge knowledge of physics and affable nature always helps me in both of research and daily life. I must also appreciate Dr. Iwakami, who kindly gave me her data of the state-of-the-art numerical simulations of SASI. Thanks to her gentle helps, I was able to proceed the researches with the credible guidelines.

I must be also grateful for Dr. Nagakura, who is a senior in Yamada laboratory. He often gave me some advice and I enjoyed daily lives with him. I would also like to appreciate the persons who have advised me in my research and daily life: Drs. Sawai, Itoh, Nakazato, Sanada, Shikita and Furusawa, who are my seniors in Yamada laboratory, and also Drs. Yamasaki, Nakamura, Yasutake, Okawa and Fujisawa, who are postdocs in Yamada laboratory, as well as junior colleagues in the laboratory. I must appreciate the members of Maeda laboratory too.

Finally, I would like to thank my parents and sister for their supports ever.

Appendix A

A.1 The integration path in the inverse Laplace transform

Here we consider the integral path in the inverse Laplace transform, that is, how to choose x in Eq. (2.18) (see also Sec. 2.2.2). The value of x should be chosen so that the entire path would lie in the region, in which $f^*(s)$ exists, i.e., the right-half ($\mathrm{Re}[s] > s_0$ for a certain real number s_0) of the complex s-plane.

We discuss the value of s_0 at first. The Laplace transformed basic equations (2.14)-(2.16) can be expressed as follows:

$$\frac{\mathrm{d}\mathbf{y}^*}{\mathrm{d}r} = [sA(r) + B(r)]\mathbf{y}^*, \tag{A.1}$$

where $\mathbf{y}^* = \mathbf{y}^*(r, s)$ is a vector whose components are the Laplace transformed variables: $\mathbf{y}^* := (\delta\rho^*/\rho,\ \delta v_r^*/v_r,\ \delta v_\perp^*/v_r)$. The matrices $A(r)$ and $B(r)$ are defined as

$$A(r) = \frac{1}{c_s(1-\mathcal{M}^2)} \begin{pmatrix} \mathcal{M} & -\mathcal{M} & 0 \\ -\dfrac{1}{\mathcal{M}} & \mathcal{M} & 0 \\ 0 & 0 & \dfrac{\mathcal{M}^2-1}{\mathcal{M}} \end{pmatrix}, \tag{A.2}$$

$$B(r) = \frac{1}{1-\mathcal{M}^2} \begin{pmatrix} \mathcal{M}^2\dfrac{\mathrm{d}}{\mathrm{d}r}\ln\dot{M} - \dfrac{\gamma-1}{\rho}\dfrac{\mathrm{d}\rho}{\mathrm{d}r} & \mathcal{M}^2\left(\dfrac{\mathrm{d}}{\mathrm{d}r}\ln\dot{M} - \dfrac{2}{v_r}\dfrac{\mathrm{d}v_r}{\mathrm{d}r}\right) & -\dfrac{\mathcal{M}^2 l(l+1)}{r} \\ -\dfrac{\mathrm{d}}{\mathrm{d}r}\ln\dot{M} + \dfrac{\gamma-1}{\rho}\dfrac{\mathrm{d}\rho}{\mathrm{d}r} & -\dfrac{\mathrm{d}}{\mathrm{d}r}\ln\dot{M} + \dfrac{2\mathcal{M}^2}{v_r}\dfrac{\mathrm{d}v_r}{\mathrm{d}r} & \dfrac{l(l+1)}{r} \\ \dfrac{\mathcal{M}^2-1}{r\mathcal{M}^2} & 0 & (\mathcal{M}^2-1)\left(\dfrac{1}{v_r}\dfrac{\mathrm{d}v_r}{\mathrm{d}r} + \dfrac{1}{r}\right) \end{pmatrix}. \tag{A.3}$$

Note that $\mathrm{d}\ln\dot{M}/\mathrm{d}r = 0$ in steady accretions. Equation (A.1) is solved formally:

$$\mathbf{y}^*(\quad) = \mathcal{P}\ \exp\ \int_R^r \mathrm{d}\ '(\quad(\ ')+\quad(\ '))\quad \mathbf{y}\ (\quad) \tag{A.4}$$

where $\mathcal{P}$ is an operator that takes a path-ordered product (Peskin & Schroeder, 1995). The norm of the solution is then estimated as follows.

$$||\mathbf{y}\ (\quad) \qquad \left|\left|\mathcal{P}\left[\exp\left[\int_R^r \mathrm{d}r'\,(sA(r')+B(r'))\right]\right]\right|| \, ||\mathbf{y}^*(R,s)||, \tag{A.5}$$

$$\leq \sum_{k=0}^{\infty}\frac{1}{k!}\int_R^r\cdots\int_R^r |\mathrm{d}r'_1|\cdots|\mathrm{d}r'_k| \times||\mathcal{P}[(sA(r'_1)+B(r'_1))\cdots(sA(r'_k)+B(r'_k))]|| \ ||\mathbf{y}^*(R,s)|| \tag{A.6}$$

Since the background flow is non-singular and we are concerned with a finite interval of r, the norm of the matrix $sA(r)+B(r)$ is bounded as

$$||sA(r)+B(r)|| \leq ||sA(r)|| + ||B(r)||, \tag{A.7}$$

$$\leq |s|C_A + C_B, \tag{A.8}$$

where C_A and C_B are some positive constants. And $|R-r|$ is also bounded by a constant, say, L. We hence obtain the following:

$$||\mathbf{y}^*(r,s)|| \leq \sum_{k=0}^{\infty}\frac{1}{k!}\int_R^r\cdots\int_R^r |\mathrm{d}r'_1|\cdots|\mathrm{d}r'_k|\ (|s|C_A+C_B)^k||\mathbf{y}^*(R,s)||, \tag{A.9}$$

$$\leq \sum_{k=0}^{\infty}\frac{L^k(|s|C_A+C_B)^k}{k!}||\mathbf{y}^*(R,s)||, \tag{A.10}$$

$$= \exp\left[L(|s|C_A+C_B)\right]||\mathbf{y}^*(R,s)||. \tag{A.11}$$

Since $\exp\left[L(|s|C_A+C_B)\right]$ is finite for any complex s, the singularity of the Laplace transformed solution, if any, should originate from the boundary function, $\mathbf{y}^*(R,s)$. From this fact, we know *a priori* where the singularities exist and hence how to choose x. For example, if a sinusoidal perturbation, $\sin(\omega t)$, is imposed at the outer boundary, the Laplace transformed solution has two poles at $s = \pm i\omega$, since $\mathcal{L}[\sin(\omega t)] = \omega/(s^2+\omega^2)$. In this case, we can choose any positive real x, i.e. $x > 0$.

We could not choose so large an x, however. Recalling the formula (2.19) and the fact that the inverse Laplace transform is independent of x, we know that

$$\int_{-\infty}^{\infty} f^*(x,y)e^{iyt}\mathrm{d}y \propto e^{-tx}, \tag{A.12}$$

since the prefactor $\exp[tx]$ in Eq. (2.19) should be canceled out. In addition to the requirement that these factors should not overflow or underflow, we need to ensure the cancellation numerically, which would be difficult for large values of x.

On the other hand, we had better not choose so small an x, either. In fact, as x becomes smaller, the integral path moves closer to the singularities and the vicinities of the singularities contribute more to the integral. Then, we need to deploy a finer grid for the integral, Δy, which would be numerically costly.

A.2 Perturbation growths in steady states

Here we derive time-independent solutions of Eqs. (2.14)-(2.16) in some limits, which would be useful in understanding the systematics of perturbation growths. They are obtained formally by taking the $t \to \infty$ limit, which in turn corresponds to the limit of $s \to 0$ in the Laplace transformed quantities. We assume that l is sufficiently large and consider only its leading terms. Unlike the previous works we do not take the limit of $r \to 0$ here. Instead the inner boundary is rather distant from the center. As a result, the Mach number is not very high and changes slowly. We further assume that $\mathbf{y}(r,t) = (\delta\rho/\rho,\ \delta v_r/v_r,\ \delta v_\perp/v_r)$ grows with l at most as $\propto l$, which is actually observed in the numerical results and will be also justified a posteriori. Then the equations that govern steady states $\mathbf{y}_\infty = \mathbf{y}(r, t=\infty)$ are

$$\frac{\mathrm{d}\mathbf{y}_\infty}{\mathrm{d}r} = B_\infty(r)\mathbf{y}_\infty, \tag{A.13}$$

in which the matrix is given as

$$B_\infty(r) = \begin{pmatrix} 0 & 0 & -\dfrac{\mathcal{M}^2 l(l+1)}{(1-\mathcal{M}^2)r} \\ 0 & 0 & \dfrac{l(l+1)}{(1-\mathcal{M}^2)r} \\ -\dfrac{1}{r\mathcal{M}^2} & 0 & -\dfrac{1}{v_r}\dfrac{\mathrm{d}v_r}{\mathrm{d}r} - \dfrac{1}{r} \end{pmatrix}. \tag{A.14}$$

From the above equations, we can write down the equation for $y_{\infty,1}(= \delta\rho/\rho|_{t=\infty})$, the first component of $\mathbf{y}_\infty$, as

$$\frac{\mathrm{d}^2 y_1}{\mathrm{d}r^2} + \frac{\mathrm{d}}{\mathrm{d}r}\ln\left[\frac{r^2 v_r(\mathcal{M}^2-1)}{\mathcal{M}^2}\right]\frac{\mathrm{d}y_1}{\mathrm{d}r} + \frac{l(l+1)}{r^2(\mathcal{M}^2-1)}y_1 = 0. \tag{A.15}$$

In this equation and hereafter we omit the subscript ∞ for notational simplicity. Suppose that v_r is described by a power law of r and $\mathcal{M}$ is constant ($= \mathcal{M}_0$). Then

the first factor of the second term is proportion to $1/r$, and the equation is rewritten with some constant, α, as follows:

$$\frac{\mathrm{d}^2 y_1}{\mathrm{d}r^2} + \frac{\alpha}{r}\frac{\mathrm{d}y_1}{\mathrm{d}r} + \frac{l(l+1)}{r^2(\mathcal{M}_0^2-1)}y_1 = 0. \tag{A.16}$$

Since $r = 0$ is a regular singularity, Eq. (A.16) can be solved by the Frobenius method as follows.

$$y_1(r) = y_1(r_0)\cos\left[\frac{l\ln(r/r_0)}{\sqrt{\mathcal{M}_0^2-1}}\right] + \frac{r_0\sqrt{\mathcal{M}_0^2-1}}{l}\left.\frac{\mathrm{d}y_1}{\mathrm{d}r}\right|_{r=r_0}\sin\left[\frac{l\ln(r/r_0)}{\sqrt{\mathcal{M}_0^2-1}}\right], \tag{A.17}$$

$$= y_1(r_0)\cos\left[\frac{l\ln(r/r_0)}{\sqrt{\mathcal{M}_0^2-1}}\right] + \frac{\mathcal{M}_0^2(l+1)}{\sqrt{\mathcal{M}_0^2-1}}y_3(r_0)\sin\left[\frac{l\ln(r/r_0)}{\sqrt{\mathcal{M}_0^2-1}}\right], \tag{A.18}$$

$$\sim \frac{\mathcal{M}_0^2 l}{\sqrt{\mathcal{M}_0^2-1}}y_3(r_0)\sin\left[\frac{l\ln(r/r_0)}{\sqrt{\mathcal{M}_0^2-1}}\right], \tag{A.19}$$

where r_0 is some reference radius and we used the approximation $l \to \infty$. From (A.19), we find that the amplitude of density perturbation is proportional to l and its radial profile is approximated by a sinusoidal function of $\ln r$. Note that the argument is also proportional to l and inversely proportional to $\mathcal{M}_0$ if $\mathcal{M}_0 \gg 1$.

Employing the same assumptions and approximations, we obtain

$$y_3(r) \sim y_3(r_0)\cos\left[\frac{l\ln(r/r_0)}{\sqrt{\mathcal{M}_0^2-1}}\right]. \tag{A.20}$$

In contrast to the density perturbation, the perturbation of transverse velocity is independent of l. Its radial distribution is again a sinusoidal function of $\ln r$ although the phase is shifted by $\pi/2$ radian with respect to that of the density perturbation, which is indeed observed in Fig. 2.5.

For the radial-velocity perturbation, the following relation is obtained by integrating Eq. (A.13),

$$y_2(r) \sim -\frac{l y_3(r_0)}{\sqrt{\mathcal{M}_0^2-1}}\sin\left[\frac{l\ln(r/r_0)}{\sqrt{\mathcal{M}_0^2-1}}\right] \sim -\frac{1}{\mathcal{M}_0^2}y_1(r). \tag{A.21}$$

Hence the radial-velocity perturbation is simply proportional to the density perturbation but the amplitude is smaller by a square of the Mach number and the phase is also shifted by π radian. These features are again discernible in Fig. 2.5.

Appendix B

B.1 How to solve the eigenvalue problem

We show here that the eigenvalue problem (3.12)-(3.14) is easily solved provided the evaluation function of the inner boundary condition (3.14), f^*, is linearly dependent on the inner boundary value of $\mathbf{y}^*$, which is natural requirement since we consider a linearized system. In fact, we obtain the eigenvalue for a given s by integrating the ordinary differential equation (3.12) twice as discussed below.

The philosophy is quite simple, which is a special case of the Newton-Raphson prescription. The next guess in the Newton-Raphson method is usually given by the approximated equation,

$$F(x+\delta x) \sim F(x) + J\delta x = 0, \tag{B.1}$$

where $F = F(x)$ is an evaluation function for a guess x and J is the Jacobi matrix. In our setup, F and x correspond to f^* and $\delta r_{sh}/r_{sh}$ respectively. If we assume that $F \propto x$, the above equation becomes an identity and hence the solution is obtained by $x_{sol} = x + \delta x = x - J^{-1}F$. In the following, we show that this linearity holds and the Jacobi matrix is easily obtained.

Recall here that the linearized equation (3.12) with the outer boundary condition (3.13) can be schematically solved with the use of the path-ordered product (see Appendix A.1). Applying the formula to the perturbed quantities at the inner boundary, it is schematically given as follows:

$$\mathbf{y}^*(r_{PNS}, s) = \mathcal{P}\left[\exp\left[-\int_{r_{sh}}^{r_{PNS}} \mathrm{d}r'(sP^{-1}M + P^{-1}Q)\right]\right]\mathbf{y}^*(r_{sh}, s), \tag{B.2}$$

$$= \mathcal{P}\left[\exp\left[-\int_{r_{sh}}^{r_{PNS}} \mathrm{d}r'(sP^{-1}M + P^{-1}Q)\right]\right]\left[s\frac{\delta r^*_{\rm sh}}{r_{\rm sh}}\mathbf{c} + R\mathbf{z}^*(r_{\rm sh}, s)\right]. \tag{B.3}$$

From the above equations, $\mathbf{y}^*$ at the inner boundary radius is proportional to $\delta r_{sh}/r_{sh}$. Since we assume that f^* is a linear function with respect to $\mathbf{y}^*(r = r_{PNS})$, $f^* \propto \delta r_{sh}/r_{sh}$ follows.

The Jacobi matrix is given by

$$J = \frac{\mathrm{d}f^*}{\mathrm{d}(\delta r_{sh}/r_{sh})} = \sum_j \frac{\partial f^*}{\partial y_j^*} \frac{\partial y_j^*}{\partial(\delta r_{sh}/r_{sh})}, \tag{B.4}$$

where the factor, $\partial f^*/\partial y_j^*$, in the last equation is known once the evaluation function is given and the derivatives, $\partial y_j^*/\partial(\delta r_{sh}/r_{sh})$, is obtained with the use of (B.3):

$$\left.\frac{\partial \mathbf{y}^*}{\partial(\delta r_{sh}/r_{sh})}\right|_{r=r_{PNS}} = s\mathcal{P}\left[\exp\left[-\int_{r_{sh}}^{r_{PNS}} \mathrm{d}r'(sP^{-1}M + P^{-1}Q)\right]\right]\mathbf{c}. \tag{B.5}$$

The right-hand side can be calculated by integrating the ordinary differential equation with an outer boundary condition that is modified as:

$$\mathbf{y}^*(r_{\mathrm{sh}}, s) \;=\; s\mathbf{c}. \tag{B.6}$$

As a result, we can obtain the eigenvalue for a given s by integrating the ordinary differential equation (3.12) twice: One is a trial integration for the outer boundary condition (3.13), which is given by an arbitrary guess, and the other is for the modified boundary (B.6).

B.2 Matrices and vectors

In this section, we give the matrices and vectors that are appeared in Chapter 3. The matrices in the basic equations are given as follows:

$$M(r) = \begin{pmatrix} 1 & 0 & 0 & 0 & 0 & 0 \\ 0 & 1 & 0 & 0 & 0 & 0 \\ 0 & 0 & 1 & 0 & 0 & 0 \\ \frac{\rho}{v_r^2}\frac{\partial \varepsilon}{\partial \rho} & 0 & 0 & \frac{T}{v_r^2}\frac{\partial \varepsilon}{\partial T} & \frac{Y_e}{v_r^2}\frac{\partial \varepsilon}{\partial Y_e} & 0 \\ 0 & 0 & 0 & 0 & 1 & 0 \\ 0 & 0 & 0 & 0 & 0 & 1 \end{pmatrix}, \tag{B.7}$$

$$P(r) = \begin{pmatrix} v_r & v_r & 0 & 0 & 0 & 0 \\ \frac{1}{v_r}\frac{\partial p}{\partial \rho} & v_r & 0 & \frac{T}{\rho v_r}\frac{\partial p}{\partial T} & \frac{Y_e}{\rho v_r}\frac{\partial p}{\partial Y_e} & 0 \\ 0 & 0 & v_r & 0 & 0 & 0 \\ \frac{\rho}{v_r}\frac{\partial \varepsilon}{\partial \rho} & \frac{p}{\rho v_r} & 0 & \frac{T}{v_r}\frac{\partial \varepsilon}{\partial T} & \frac{Y_e}{v_r}\frac{\partial \varepsilon}{\partial Y_e} & 0 \\ 0 & 0 & 0 & 0 & v_r & 0 \\ 0 & 0 & 0 & 0 & 0 & v_r \end{pmatrix}, \tag{B.8}$$

$$Q(r) = \begin{pmatrix} 0 & 0 & -v_r\frac{l(l+1)}{r} & 0 & 0 & 0 \\ \frac{1}{v_r}\frac{\mathrm{d}}{\mathrm{d}r}\frac{\partial p}{\partial \rho} & 2\frac{\mathrm{d}v_r}{\mathrm{d}r} & 0 & \frac{1}{v_r}\frac{\mathrm{d}}{\mathrm{d}r}\left(\frac{T}{\rho}\frac{\partial p}{\partial T}\right) & \frac{1}{v_r}\frac{\mathrm{d}}{\mathrm{d}r}\left(\frac{Y_e}{\rho}\frac{\partial p}{\partial Y_e}\right) & 0 \\ \frac{1}{rv_r}\frac{\partial p}{\partial \rho} & 0 & \frac{v_r}{r}+\frac{\mathrm{d}v_r}{\mathrm{d}r} & \frac{T}{r\rho v_r}\frac{\partial p}{\partial T} & \frac{Y_e}{r\rho v_r}\frac{\partial p}{\partial Y_e} & 0 \\ Q_{41} & -\frac{p}{\rho v_r}\frac{l(l+1)}{r} & 0 & Q_{44} & Q_{45} & 0 \\ -\frac{m_b}{Y_e}\frac{\partial \lambda}{\partial \rho} & 0 & 0 & -\frac{m_b T}{\rho Y_e}\frac{\partial \lambda}{\partial T} & \frac{v_r}{Y_e}\frac{\mathrm{d}Y_e}{\mathrm{d}r}-\frac{m_b}{\rho}\frac{\partial \lambda}{\partial Y_e} & 0 \\ 0 & 0 & 0 & 0 & 0 & \frac{v_r}{r}+\frac{\mathrm{d}v_r}{\mathrm{d}r} \end{pmatrix}, \tag{B.9}$$

where

$$Q_{41} = \frac{1}{v_r}\left[\frac{\mathrm{d}}{\mathrm{d}r}\left(\rho\frac{\partial\varepsilon}{\partial\rho}\right) - \frac{1}{\rho}\frac{\mathrm{d}\rho}{\mathrm{d}r}\left(\frac{\partial p}{\partial\rho} - \frac{p}{\rho}\right) - \frac{\rho}{v_r}\frac{\partial q}{\partial\rho}\right], \tag{B.10}$$

$$Q_{44} = \frac{1}{v_r}\left[\frac{\mathrm{d}}{\mathrm{d}r}\left(T\frac{\partial\varepsilon}{\partial T}\right) - \frac{T}{\rho^2}\frac{\mathrm{d}\rho}{\mathrm{d}r}\frac{\partial p}{\partial T} - \frac{T}{v_r}\frac{\partial q}{\partial T}\right], \tag{B.11}$$

$$Q_{45} = \frac{1}{v_r}\left[\frac{\mathrm{d}}{\mathrm{d}r}\left(Y_e\frac{\partial\varepsilon}{\partial Y_e}\right) - \frac{Y_e}{\rho^2}\frac{\mathrm{d}\rho}{\mathrm{d}r}\frac{\partial p}{\partial Y_e} - \frac{Y_e}{v_r}\frac{\partial q}{\partial Y_e}\right], \tag{B.12}$$

Note here that we take ρ, T and Y_e as independent thermodynamic quantities in the above expression and we did not note the fixed variables for notational simplicity when we take the derivatives of them.

The matrix R in the linearized Rankine-Hugoniot relations have the following form:

$$R = \begin{pmatrix} {U^{(\mathrm{down})}}^{-1}V^{(\mathrm{up})} & \mathbf{0} & \mathbf{0} \\ \mathbf{0}^T & \dfrac{\rho v_r^2}{\rho v_r^2 + [\![p]\!]} & 0 \\ \mathbf{0}^T & 0 & \dfrac{\rho v_r^2}{\rho v_r^2 + [\![p]\!]} \end{pmatrix}, \tag{B.13}$$

where $[\![X]\!] := X^{(\mathrm{up})} - X^{(\mathrm{down})}$ denotes a jump of a quantity X across the shock and the 4×4 matrices $U^{(\mathrm{down})}$ and $V^{(\mathrm{up})}$, whose components are composed of the background quantities below and above the shock respectively, are given by

$$U^{(\mathrm{down})} = \begin{pmatrix} 1 & 1 & 0 & 0 \\ v_r + \dfrac{1}{v_r}\dfrac{\partial p}{\partial\rho} & 2v_r & \dfrac{T}{\rho v_r}\dfrac{\partial p}{\partial T} & \dfrac{Y_e}{\rho v_r}\dfrac{\partial p}{\partial Y_e} \\ \dfrac{E}{\rho} + \rho\dfrac{\partial\varepsilon}{\partial\rho} + \dfrac{\partial p}{\partial\rho} & \dfrac{E+\rho v_r^2+p}{\rho} & T\left(\dfrac{\partial\epsilon}{\partial T} + \dfrac{1}{\rho}\dfrac{\partial p}{\partial T}\right) & Y_e\left(\dfrac{\partial\varepsilon}{\partial Y_e} + \dfrac{1}{\rho}\dfrac{\partial p}{\partial Y_e}\right) \\ 1 & 1 & 0 & 1 \end{pmatrix}, \tag{B.14}$$

$$V^{(\mathrm{up})} = \begin{pmatrix} 1 & 1 & 0 & 0 \\ v_r & 2v_r & \dfrac{p}{\rho v_r} & 0 \\ \dfrac{E}{\rho} + \rho\dfrac{\partial\varepsilon}{\partial\rho} & \dfrac{E+\rho v_r^2+p}{\rho} & p\left(\dfrac{1}{\rho} + \dfrac{\partial\varepsilon}{\partial p}\right) & Y_e\dfrac{\partial\varepsilon}{\partial Y_e} \\ 1 & 1 & 0 & 1 \end{pmatrix}, \tag{B.15}$$

where the quantities in the above equations are understood as those below and above the shock for $U^{(\mathrm{down})}$ and $V^{(\mathrm{up})}$ respectively. We also note that we take ρ, T and Y_e as

independent thermodynamic quantities for the downstream whereas we choose ρ, p and Y_e for the upstream. We did not note the fixed variables for notational simplicity when we take the derivatives in the above expressions. The vectors $\mathbf{c}$ and $\mathbf{z}^{\rm up}$ are given as

$$\mathbf{c} = \left(-U^{(\rm down)^{-1}} \zeta,\ -\frac{[\![p]\!]}{\rho v_r^2 + [\![p]\!]},\ 0 \right)^T , \tag{B.16}$$

$$\zeta = \left(\frac{r_{sh}[\![\rho]\!]}{\rho v_r^2},\ 0,\ \frac{r_{sh}[\![E]\!]}{\rho v_r^2},\ \frac{r_{sh}[\![\rho]\!]}{\rho v_r^2} \right)^T , \tag{B.17}$$

$$\mathbf{z}^{(\rm up)} = \left(\frac{\delta\rho}{\rho},\ \frac{\delta v_r}{v_r},\ \frac{\delta p}{p},\ \frac{\delta Y_e}{Y_e},\ \frac{\delta v_\perp}{v_r},\ \frac{\delta v_{rot}}{v_r} \right)^T , \tag{B.18}$$

where the quantities other than $U^{(\rm down)}$ and jumps across the shock are evaluated in front of the shock.

Bibliography

Abdikamarov, E., Ott, C. D., Radice, D., Roberts, L., Haas, R., Reisswig, C., Mösta, P., Klion, H. & Schnetter, E. 2014, arXiv:1409.7078v1

Andreev, R., Torrilhon, M. & Jorosch, T. 2008, https://web.mathcces.rwth-aachen.de/mhdsolver/. Accessed April 1, 2013

Arnett, W. D. & Meakin, C. 2011, ApJ, 733, 78

Asida, S. M. & Arnett, D. 2000, ApJ, 545, 435

Barmin, A. A., Kulikovskiy, A. G. & Pogorelov, N. V. 1996, J. Comput. Phys., 126 (0121), 77

Bazan, G. & Arnett, D. 1998, ApJ, 496, 316

Bethe, H. A. & Wilson, J. R. 1985, ApJ, 295, 14

Blinnikov, S. I., Dunina-Barkovskaya, N. V. & Nadyozhin, D. K. 1996, ApJS, 106, 171

Blondin, J. M., Mezzacappa, A. & DeMarino, C. 2003, ApJ, 584, 971

Blondin, J. M. & Mezzacappa, A. 2006, ApJ, 642, 401

Blondin, J. M. & Shaw, S. 2007, ApJ, 656, 366

Brio, M. & Wu, C. C. 1988, J. Comput. Phys., 75, 400

Bruenn, S. W., Mezaacappa, A., Hix, W. R., Lentz, E. J., Messer, O. E. B., Lingerfert, E. J., Blondin, J. M., Endeve, E., Marronetti, P. & Yakunin, K. N. 2013, ApJL, 767, L6

Burrows, A. & Hayes, J. 1995, PRL, 76, 352

Burrows, A. Livne, E., Dessart, L., Ott, C. D. & Murphy, J. 2006, ApJ, 640, 878

Burrows, A. Livne, E., Dessart, L., Ott, C. D. & Murphy, J. 2007, ApJ, 655, 416

Chao, J. K. 1995, Adv. Space Res., 15 (8/9), (8/9)521

Chatzopoulos, E., Graziani, C. & Couch, S. M. 2014, ApJ, submitted (arXiv:1405.4873v1)

Colgate, S. A. & White, R. H. 1966, ApJ, 143, 626

Couch, S. M. & O'Connor, E. P. 2014, ApJ, 785, 123

Couch, S. M. & Ott, C. D. 2013, ApJL, 778, L7

Couch, S. M. & Ott, C. D. 2014, arXiv:1408.1399v1

Dai, W. & Woodward, P. R. 1994, J. Comput. Phys., 115, 485

De Sterck, H. 1999, Numerical simulation and analysis of magnetically dominated MHD bow shock flows with applications in space physics, PhD thesis, Department of Mathematics, Katholieke Universiteit Leuven, Belgium

Delmont, P. & Keppens, R. 2011, J. Plasma Phys. 77 (2), 207

Duerbeck, H. W. 2008, Chap. 1, Classical Novae (Second Edition, Ed. by Bode, M., F. & Evans, A., Cambridge: Cambridge University Press)

Endeve, E., Cardall, C. Y., Budiardja, R. D. & Mezzacappa, A. 2010, ApJ, 713, 1219

Endeve, E., Cardall, C. Y., Budiardja, R. D., Beck, S. W., Bejnood, A., Toedte, R. J., Mezzacappa, A. & Blondin, J. M. 2012, ApJ, 751, 26

Falle, S. A. E. G. & Komissarov, S. S. 1997, ASP Conference Series, 123, 66

Falle, S. A. E. G. & Komissarov, S. S. 2001, J. Plasma Phys., 65 (1), 29

Feng, H. & Wang, J. M. 2008, Solar Phys, 247, 195

Feng, H. Q., Wang, J. M. & Chao, J. K. 2009, A&A, 503, 203

Filippenko, A. V. 1997, Annu. Rev. Astron. Astrophys., 35, 309

Foglizzo, T. 2001, A&A, 368, 311

Foglizzo, T. 2002, A&A, 392, 353

Foglizzo, T. 2009, ApJ, 694, 820

Foglizzo, T., Galletti, P., Scheck, L. & Janka, H.-Th. 2007, ApJ, 654, 1006

Foglizzo, T., Masset, F., Guilet, J. & Durand, G. 2012, PRL, 108, 051103

Gogosov, V. V. 1961, J. Appl. Math. Mech., 25 (1), 148

Gogosov, V. V. 1962, J. Appl. Math. Mech., 26 (1), 118

Green, D. A. & Stephenson, F. R. 2003, arXiv:0301603v1

Guilet, J. & Foglizzo, T. 2010, ApJ, 711, 99

Guilet, J. & Foglizzo, T. 2012, MNRAS, 421, 546

Guilet, J. & Fernández, R. 2014, MNRAS, 441, 2782

Hanke, F., Müller, B., Wongwathanarat, A., Marek, A. & Janka, H.-Th. 2013, ApJ, 770, 66

Hada, T. 1994, Geophys. Res. Lett., 21 (21), 2275

Howell, D. A. 2011, arXiv:1011.0441v1

Hurley, W. 2009, Chap. 21, Neutron Stars and Pulsars (Ed. by Becker, W., Berlin: Springer)

Inoue, T. & Inutsuka, S. 2007, Prog. Theor. Phys., 118 (1), 47

Iwakami, W., Kotake, K., Ohnishi, N., Yamada, S. & Sawada, K. 2008, ApJ, 678, 1207

Iwakami, W., Kotake, K., Ohnishi, N., Yamada, S. & Sawada, K. 2009, ApJ, 700, 232

Iwakami, W., Nagakura, H. & Yamada, S. 2014, ApJ, 786, 118

Iwakami, W., Nagakura, H. & Yamada, S. 2014, ApJ, submitted (arXiv:1404.2646v1)

Iwasaki, K. & Inutsuka, S. 2011, MNRAS, 418 (3), 1668

Janka, H.-Th. 2012, ARNPS, 62, 407

Jeffrey, A. & Taniuti, T. 1964, Non-linear Wave Propagation (New York–London: Academic Press)

Kantrowitz, A. R. & Petschek, H. E. 1966, Plasma Physics in Theory and Application (New York: McGraw-Hill Book Co.)

Kotake, K., Sawai, H., Yamada, S. & Sato, K. 2004, ApJ, 608, 391

Kotake, K., Iwakami, W., Ohnishi, N. & Yamada, S. 2009, ApJL, 697, L133

Kotake, K., Iwakami-Nakano, W. & Ohnishi, N. 2011, ApJ, 736, 124

Kotake, K., Sumiyoshi, K., Yamada, S., Takiwaki, T., Kuroda, T., Suwa, Y. & Nagakura, H. 2012, PTEP, 01A301

Kovalenko, I. G. & Eremin, M. A. 1998, MNRAS, 298, 861

Kulikovskii, A. G., Pogorelov, N. P. & Semenov, A. Yu. 2001, Mathematical aspects of numerical solution of hyperbolic systems, Monographs and Surveys in Pure and Applied Mathematics, vol. 118 (Boca Raton: CHAPMAN & HALL/CRC)

Kuroda, T., Takiwaki, T. & Kotake, K. 2014, PRD, 89, 044011

Lai, D. & Goldreich, P. 2000, ApJ, 535, 402

Landau, L. D., Lifshitz, E. M. & Pitaevskii, L. P. 1984, Electrodynamics of Continuous Media, 2nd edn., Landau and Lifshitz Course of Theoretical Physics, vol. 8. (Oxford: Elsevier Butterworth-Heinemann)

Lax, P. D. 1957, Commun. Pure Appl. Math., X, 537

Liebendörfer, M., Rampp, M., Janka, H.-Th. & Mezzacappa, A. 2005, ApJ, 620, 840

Lorimer, D. R. 2009, Chap. 1, Neutron Stars and Pulsars (Ed. by Becker, W., Berlin: Springer)

Lyne, A. & Graham-Smith, F. 2006, Pulsar Astronomy (Third Edition, Cambridge: Cambridge University Press)

Marek, A. & Janka, H.-Th. 2009, 694, 664

Markovskii, S. A. 1998, Phys. Plasmas, 5 (7), 2596

Meakin, C. A. & Arnett, D. 2006, ApJL, 637, L53

Meakin, C. A. & Arnett, D. 2007, ApJ, 667, 448

Minkowski, R. 1940, PASP, 52, 206

Minkowski, R. 1941, PASP, 53, 224

Müller, B., Janka, H.-Th. & Heger, A. 2012, ApJ, 761, 72

Müller, B., Janka, H.-Th. & Marek, A. 2013, ApJ, 766, 43

Müller, B. & Janka, H.-Th. 2014, arXiv:1409.4783v1

Müller, E., Janka, H.-Th. & Wongwathanarat, A. 2012, A&A, 537, A63

Murphy, J. W., Ott, C. D. & Burrows, A. 2009, ApJ, 707, 1173

Nagakura, H. & Yamada, S. 2008, ApJ, 689, 391

Nagakura, H. & Yamada, S. 2009, ApJ, 696, 2026

Nakamura, K., Takiwaki, T., Kuroda, T. & Kotake, K. 2014, arXiv:1406.2415v1

Nordhaus, J., Brandt, T. D., Burrows, A. & Almgren, A. 2012, MNRAS, 423, 1805

Ohnishi, N., Kotake, K. & Yamada, S. 2006, ApJ, 641, 1018

Peskin, M. E. & Schroeder, D. V. 1995, An Introduction to Quantum Field Theory (Colorado: Westview Press)

Polovin, R. V. & Demutskii, V. P. 1990, Fundamentals of Magnetohydrodynamics (New York: Consultants Bureau)

Rampp, M. & Janka, H.-Th. 2000, ApJL, 539, L33

Rantsiou, E., Burrows, A., Nordhaus, J. & Almgren, A. 2011, ApJ, 732, 57

Sano, T., Inutsuka, S. & Miyama, S. M. 1999, Numerical Astrophysics: Proceedings of the International Conference on Numerical Astrophysics 1998 (NAP98), 383

Sato, J., Foglizzo, T. & Fromang, S. 2009, ApJ, 694, 833

Sawai, H., Kotake, K. & Yamada, S. 2005, ApJ, 631, 446

Sawai, H., Yamada, S. & Suzuki, H. 2013, ApJL, 770, L19

Sawai, H. & Yamada, S. 2014, ApJL, 784, L10

Schiff, J. L. 1999, The Laplace Transform: Theory and Applications (Berlin: Springer)

Serre, D. 1999, System of Conservation Laws, (Cambridge: Cambridge University Press)

Scheck, L., Kifonidis, K., Janka, H.-Th. & Müller, E. 2006, A&A, 457, 963

Scheck, L., Janka, H.-Th., Foglizzo, T. & Kifonidis, K. 2008, A&A, 477, 931

Suwa, Y., Kotake, K., Takiwaki, T., Whitehouse, S. C., Liebendörfer, M. & Sato, K. 2010, PASJ, 62, L49

Suwa, Y., Yamada, S., Takiwaki, T. & Kotake, K. 2014, arXiv:1406.6414v1

Takiwaki, T., Kotake, K. & Suwa, Y. 2012, ApJ, 749, 98

Takiwaki, T., Kotake, K. & Suwa, Y. 2014, ApJ, 786, 83

Torrilhon, M. 2002, Exact solver and uniqueness conditions for Riemann problems of ideal magnetohydrodynamics, research report 2002-06, Zurich: Seminar for Applied Mathematics, ETH

Torrilhon, M. 2003, J. Comput. Phys., 192, 73

Torrilhon, M. 2003, J. Plasma Phys., 69 (3), 253

Wongwathanarat, A., Janka, H.-Th. & Müller, E. 2010, ApJL, 725, L106

Wongwathanarat, A., Janka, H.-Th. & Müller, E. 2013, A&A, 552, A126

Woosley, S. E. & Heger, A. 2007, PhR, 442, 269.

Woosley, S. E., & Weaver, T. A. 1995, ApJS, 101, 181

Wu, C. C. 1987, Geophys. Res. Lett. 14 (6), 668

Wu, C. C. 1988, J. Geophys. Res., 93 (A5), 3969

Wu, C. C. 1988, J. Geophys. Res. 93 (A2), 987

Wu, C. C. 1990, J. Geophys. Res., 95 (A6), 8149

Wu, C. C. & Kennel, C. F. 1992, Geophys. Res. Lett., 19 (20), 2087

Yamamoto, Y., Fujimoto, S., Nagakura, H. & Yamada, S. 2013, ApJ, 771, 27

Yamasaki, T. & Foglizzo, T. 2008, ApJ, 679, 607

Yamasaki, T. & Yamada, S. 2005, ApJ, 623, 1000

Yamasaki, T. & Yamada, S. 2006, ApJ, 650, 291

Yamasaki, T. & Yamada, S. 2007, ApJ, 656, 1019

Yoshida, S., Ohnishi, N. & Yamada, S. 2007, ApJ, 665, 1268

早稲田大学　博士（理学）　学位申請　研究業績書

氏 名　高橋　和也　　印

（2014 年 12 月　現在）

種 類 別	題名、　発表・発行掲載誌名、　発表・発行年月、　連名者（申請者含む）
○論文	題名：Linear analysis on the growth of non-spherical perturbations in supersonic accretion flows 掲載誌：The Astrophysical Journal, 794, 162 発行年月：2014 年 10 月 連名者：Kazuya Takahashi & Shoichi Yamada
○論文	題名：Exact Riemann solver for ideal magnetohydrodynamics that can handle all types of intermediate shocks and switch-on/off waves 掲載誌：Journal of Plasma Physics, volume 80, issue 02, pp. 255-287 発行年月：2014 年 4 月 連名者：Kazuya Takahashi & Shoichi Yamada
○論文	題名：Regular and non-regular solutions of the Riemann problem in ideal magnetohydrodynamics 掲載誌：Journal of Plasma Physics, volume 79, issue 03, pp. 335-356 発行年月：2013 年 6 月 連名者：Kazuya Takahashi & Shoichi Yamada
総説	題名：On the Existence and Non-uniqueness of Solutions of Riemann Problems in Ideal Magnetohydrodynamics 掲載誌：ASTRONOMICAL SOCIETY OF THE PACIFIC CONFERENCE SERIES, Vol. 488 発行年月：2014 年 9 月 連名者：Kazuya Takahashi & Shoichi Yamada
国際学会	題名：Study on the growth and time-variability of fluctuations in super-sonic flows: toward more realistic investigations on standing accretion shock instability 発表学会：Multi-Messengers from Core-Collapse Supernovae (MMCOCOS), Fukuoka, Japan 発表年月：2013 年 12 月 連名者：Kazuya Takahashi & Shoichi Yamada（ポスター）
国際学会	題名：On the existence and non-uniqueness of solutions of Riemann problems in ideal magnetohydrodynamics 発表学会：ASTRONUM 2013 (8th International Conference on Numerical Modeling of Space Plasma Flows), Biarritz, France 発表年月：2013 年 7 月 連名者：Kazuya Takahashi & Shoichi Yamada（口頭）

早稲田大学　博士（理学）　学位申請　研究業績書

種 類 別	題名、　発表・発行掲載誌名、　発表・発行年月、　連名者（申請者含む）
国内学会	題名：親星の対流層が定在降着衝撃波不安定性に与える影響の解析 発表学会：日本天文学会２０１３年秋季年会、講演予稿集 K22a、東北大学 発表年月：2013 円 9 月 連名者：高橋和也、山田章一（口頭）
国内学会	題名：理想 MHD Riemann 問題の中間衝撃波の物理的妥当性に関する新しい示唆について 発表学会：日本物理学会 第６８回年次大会、講演番号 26aEA7、広島大学 発表年月：2013 円 3 月 連名者：高橋和也、山田章一（口頭）
国内学会	題名：Regular and non-regular solutions of the Riemann problem in ideal magnetohydrodynamics 発表学会：卓越した大学院拠点形成支援事業スタートアップ・シンポジウム、早稲田大学 発表年月：2013 年 3 月 連名者：高橋和也、山田章一（ポスター）
国内学会	題名：Regular and non-regular solutions of the Riemann problem in ideal magnetohydrodynamics 発表学会：第２５回理論懇シンポジウム「計算宇宙物理学の新展開」、つくば国際会議場 発表年月：2012 年 12 月 連名者：高橋和也、山田章一（ポスター）
国内学会	題名：理想 MHD Riemann 問題の解の非一意性と安定性 発表学会：日本天文学会２０１２年春季年会、講演予稿集 J15a、龍谷大学 発表年月：2012 年 3 月 連名者：高橋和也、山田章一（口頭）

早稲田大学　博士（理学）　学位申請　研究業績書

種 類 別	題名、　発表・発行掲載誌名、　発表・発行年月、　連名者（申請者含む）
海外講演	題名：On the intermediate shocks and non-uniqueness of the solutions in ideal MHD Riemann problems 発表場所：Max-Planck Institute for Astrophysics, Garching, Germany 発表年月：2013 年 7 月 9 日 連名者：高橋和也、山田章一
国内講演	題名：On the existence and non-uniqueness of solutions of Riemann problems in ideal magnetohydrodynamics 発表場所：Ta 研コロキウム、名古屋大学 発表年月：2013 年 5 月 31 日 連名者：高橋和也、山田章一
国内講演	題名：理想 MHD 方程式の未解決問題 発表場所：高エネルギーセミナー、国立天文台 発表年月：2012 年 12 月 6 日 連名者：高橋和也、山田章一
国内講演	題名：理想 MHD Riemann 問題における intermediate shocks 発表場所：プラズマセミナー、国立天文台 発表年月：2012 年 11 月 30 日 連名者：高橋和也、山田章一
国内講演	題名：MHD Riemann 問題の解の非一意性と安定性 発表場所：茂山研究室セミナー、東京大学ビッグバン宇宙国際研究センター 発表年月：2012 年 7 月 13 日 連名者：高橋和也、山田章一